UNIVERSITÄT PADERBORN
Die Universität der Informationsgesellschaft

FAKULTÄT FÜR
ELEKTROTECHNIK,
INFORMATIK UND
MATHEMATIK

Implementation and investigation of a real-time optical 16-QAM transmission system with FPGA-based coherent receiver

Von der Fakultät für Elektrotechnik, Informatik und Mathematik
der Universität Paderborn

zur Erlangung des akademischen Grades

Doktor der Ingenieurwissenschaften (Dr.-Ing.)

genehmigte Dissertation

von

M.Sc. Ali Al-Bermani

Erster Gutachter:	Prof. Dr.-Ing. Reinhold Noé
Zweiter Gutachter:	Prof. Dr.-Ing. Ulrich Rückert

Tag der mündlichen Prüfung: 10.09.2013

Paderborn 2013

Diss. EIM-E/294

Abstract

Virtually all telecom providers need to upgrade their networks cost-efficiently to accommodate the ever-increasing data traffic. Particular effort is being undertaken to upgrade these existing optical wavelength division multiplex transmission systems with a channel spacing of 50 GHz and a channel data rate of 10 Gb/s to a channel data rate of >100 Gb/s, while at the same time achieving superior signal-to-noise performance and robustness against optical dispersions. 100 Gb/s per channel or above can be reached by coherent receivers with digital signal processing by now. In recent years QPSK was the preferred modulation format because of its robustness on long-haul links. But for transmission over less than ultimate distance, higher-order quadrature amplitude modulation (QAM) is attractive, namely 16-point QAM which doubles spectral efficiency compared to QPSK. Simulations and offline experiments have recently been published, but real-time investigations are essential for progress towards commercial applications. The core element of such a transponder is a DSPU capable to recover clock, IF carrier and data in real-time. Field programmable gate arrays (FPGA) enable evaluating digital receiver algorithms in real-time experiments before being implemented as CMOS circuits.

In this dissertation the first published real-time implementation of a 16-QAM transmission system with FPGA-based DSP is presented. 2.5 Gb/s coherent 16-QAM data has been optically transmitted over 20 and 100 km and synchronously received by heterodyning in a real-time I&Q receiver, with BER below the threshold of a state-of-the-art FEC (7% overhead). Two techniques of feed-forward carrier phase recovery (Blind Phase Search (BPS) and QPSK partitioning (QPSKP)) were tested in a real-time transmission experiment and compared with each other. The influence of the required resolution of the analog-to-digital converter (ADC) has been investigated, which is a challenge of real-time coherent transmission systems. The influence of phase noise in 16-QAM, which is mainly contributed from laser sources, optical amplifiers, and nonlinear effects in optical fibers is also shown. Moreover, different operation points of a 16-QAM modulator were tested in real-time and an optimal condition is found which minimizes the BER.

Zusammenfassung

Um den ständig wachsenden Datenverkehr zu bewältigen, müssen praktisch alle Telekommunikationsanbieter die Überragungskapazitäten ihrer Netzwerke kosteneffizient erweitern. Existierende WDM-Übertragungssysteme (wavelength divistion multiplex) mit 10 Gb/s Kanaldatenrate und 50 GHz Kanalabstand werden zur Zeit mit großem Aufwand aufgerüstet, um Kanaldatenraten von >100 Gb/s zu erreichen. Dabei soll gleichzeitig ein größtmöglicher Signal-Rausch-Abstand und Robustheit gegenüber Dispersion erreicht werden. Kanaldatenraten von über 100 Gb/s werden inzwischen auch von kohärenten Empfängern mit digitaler Signalverarbeitung erreicht. Dabei hat sich QPSK wegen seiner Robustheit in den letzten Jahren als das bevorzugte Modulationsverfahren auf Langstrecken bewährt. Für Übertragung auf weniger langen Strecken scheint auch ein noch höherwertiges Quadratur-Amplituden-Modulationsverfahren (QAM), nämlich 16-QAM, interessant zu sein. 16-QAM verdoppelt die spektrale Effizienz gegenüber QPSK. Viele Ergebnisse aus Simulationen und offline-Datenverarbeitung wurden bereits veröffentlicht, aber für den Fortschritt in Richtung kommerzieller Anwendung sind Experimente mit einem Echtzeit-Übertragungssystem unerlässlich. Das Kernelement eines geeigneten Echtzeitempfängers ist die Einheit für die digitale Signalverarbeitung (DSPU), die Takt, Daten und IF-Carrier in Echtzeit zurückgewinnt. Feldprogrammierbare Logikbausteine (FPGAs) ermöglichen die Erprobung der notwendigen Algorithmen in Echtzeitexperimenten bevor sie als feste CMOS-Schaltungen implementiert werden.

Diese Dissertation stellt die erste Echtzeitübertragung von 16-QAM mit FPGA-basierter DSPU vor. 2.5 Gb/s wurden dabei über 20 und 100 km übertragen und kohärent (heterodyn) in Echtzeit empfangen. Die Bitfehlerquote (BER) lag dabei unterhalb der Schwelle moderner Fehlervorwärtskorrekturverfahren mit 7% Overhead. Mit BPS (Blind Phase Search) und QPSK partitioning (QPSKP) wurden zwei unterschiedliche Techniken zur Phasenrückgewinnung implementiert und durch Echtzeitmessung verglichen. Der Einfluss der Auflösung der erforderlichen Analog-Digital-Umsetzer (ADC) wurde ebenfalls untersucht, welche ebenfalls eine Herausforderung für kohärente Echtzeitübertragung darstellt. Der Einfluss von Phasenrauschen wird hier auch gezeigt, welches vorwiegend von den verwendeten Lasern, optischen Verstärkern und nichtlinearen Effekten in den optischen Fasern abhängt. Darüber hinaus wurden verschiedene Arbeitspunkte des 16-QAM-Modulators in Echtzeit getestet und die optimalen Bedingungen für eine minimale Bitfehlerquote gefunden.

Acknowledgement

I would like to thank Prof. Dr.-Ing. Reinhold Noe for giving me the opportunity to pursue my PhD at Paderborn University, and for his constant support and guidance throughout my research.

I would like to thank Prof. Dr.-Ing. Ulrich Rückert and his research group especially Dipl.-Ing. Christian Wördehoff for his support during my research. I am also grateful to Dr. Timo Pfau, Dr. David Sandel and Dr. Sebastian Hoffmann for the enormous help I received from them. Special thanks go to all my colleagues and the technical staff in the Optical Communications group.

I am grateful to the German academic exchange service (DAAD) for providing me with necessary funds for my studies in Paderborn.

Finally I would like to thank my small and big family including my beloved parents, wife, children and all of my friends for their patience and support.

Paderborn, Germany *Ali Al-Bermani*
September 11, 2013

Publications

Journal Papers

O. Jan, D. Sandel, K. Puntsri, **A. Al-Bermani**, M. El-Darawy, and R. Noé, “The robustness of subcarrier-index modulation in 16-QAM CO-OFDM system with 1024-point FFT”, *Optics Express*, Vol. 20, Issue 27, pp. 28963–28968, 2012.

A. Al-Bermani, C. Wördehoff, S. Hoffmann, T. Pfau, U. Rückert, and R. Noé, " Synchronous Demodulation of Coherent 16-QAM with Feedforward Carrier Recovery ", *IEICE Transactions on Communications*, E94.B , No. 7, July 2011, Japan (invited).

A. Al-Bermani, C. Wördehoff, S. Hoffmann, D. Sandel, U. Rückert, and R. Noé, " Real-Time Phase-Noise-Tolerant 2.5-Gb/s Synchronous 16-QAM Transmission ", *IEEE Photonics Technology Letters*, VOL. 22, NO. 24, pp. 1823-1825, December 15, 2010.

S. Hoffmann, C. Wördehoff, **A. Al-Bermani**, M. El-Darawy, K. Puntsri, U. Rückert, and R. Noe, "Hardware-Efficient Phase Estimation for Digital Coherent Transmission with Star Constellation QAM", *IEEE Photonics Journal*, Vol. 2 , No. 2, pp. 174 - 180 (invited).

Conference papers

O. Jan, K. Puntsri, D. Sandel, **A. Al-Bermani**, C. Wördehoff, U. Rückert and R. Noe, " An Experiment of Subband Spectral Shaping in DFT-Spread CO-OFDM systems," *Proc. Conf. 10th Conference on Lasers and Electro-Optics Pacific Rim, and the 18th OptoElectronics and Communications Conference / Photonics in Switching 2013 (CLEO-PR&OECC/PS 2013)*, 2013, Kyoto, Japan.

K. Puntsri, O. Jan, **A. Al-Bermani**, D. Sandel, C. Wördehoff, S. Hussin, M. F. Panhwar, U. Rückert and R. Noe, " Pilot-aided CD and PN Compensation Simultaneously in CO-OFDM Systems," *Proc. Conf. 10th Conference on Lasers and Electro-Optics Pacific Rim, and the 18th OptoElectronics and Communications Conference / Photonics in Switching 2013 (CLEO-PR&OECC/PS 2013)*, 2013, Kyoto, Japan.

A. Al-Bermani, C. Wördehoff, O. Jan, K. Puntsri, M. F. Panhwar, U. Rückert, and R. Noé, "The Influence of Laser Phase noise on Carrier Phase Estimation of a Real-Time 16-QAM Transmission with FPGA Based Coherent Receiver", *14. ITG-Fachtagung "Photonische Netze"*, 6.-7. May 2013 Leipzig, Germany.

O. Jan, K. Puntsri, **A. Al-Bermani**, C. Wördehoff, U. Rückert, and R. Noé, " An Experiment of Coherent Optical DFT spread OFDM with Laser Phase Noise", *14. ITG-Fachtagung "Photonische Netze"*, 6.-7. May 2013 Leipzig, Germany.

K. Puntsri, O. Jan, **A. Al-Bermani**, C. Wördehoff, D. Sandel, M. F. Panhwar, S. Hussin, U. Rückert, and R. Noé, "ISI Tolerance of Cyclic Prefix Free Coherent Optical OFDM Communication System", *14. ITG-Fachtagung "Photonische Netze"*, 6.-7. May 2013 Leipzig, Germany.

M. F. Panhwar, C. Wördehoff, K. Puntsri, **A. Al-Bermani**, U. Rückert and R. Noé, "Adaptive Search Based Efficient Non-Data Aided FD CD Estimation for FDE", *14. ITG-Fachtagung "Photonische Netze"*, 6.-7. May 2013 Leipzig, Germany.

K. Puntsri, O. Jan, **A. Al-Bermani**, C. Wördehoff, D. Sandel, S. Hussin, M. F. Panhwar, R. Noé, and U. Rückert, " An Ultralow Complexity Algorithm for Frame Synchronization and IQ Alignment in CO-OFDM Systems", *Proc. OFC/NFOEC 2013*, March 17.-21., 2013, JTh2A.43, Anaheim, CA, USA.

A. Al-Bermani, C. Wördehoff, S. Hoffmann, U. Rückert, and R. Noé, "Real-time Comparison of Blind Phase Search with Different Angle Resolutions for 16-QAM ", *Proc. IEEE Photonics 2012 Conference (IPC12)*, formerly (LEOS), 23 - 27 September 2012, Burlingame, California, USA.

K. Puntsri, D. Sandel, S. Hussin, O. Jan, **A. Al-Bermani**, M. F. Panhwar, and R. Noé, "A Low Complexity and High Accuracy Frame Synchronization for Optical OFDM and PolMux-Optical OFDM", *Proc. IEEE Photonics 2012 Conference (IPC12)*, formerly (LEOS), 23 - 27 September 2012 , Burlingame, California, USA.

O. Jan, D. Sandel, M. El-Darawy, K. Puntsri, **A. Al-Bermani,** and R. Noé, "Phase Noise Robustness of SIM-OFDM in CO-OFDM Transmission", *Proc. European Conference on Optical Communication (ECOC2012)*, Amsterdam, 16.-20. Sept. 2012.

K. Puntsri, D. Sandel, S. Hussin, O. Jan, **A. Al-Bermani**, M. F. Panhwar, and R. Noé, "A Novel Method for IQ Imbalance Compensation in CO-OFDM Systems", *Proc. Conf. 17th Opto-Electronics and Communications Conference (OECC 2012)*, 2-6 July 2012, Busan, South Korea.

O. Jan, D. Sandel, M. El-Darawy, K. Puntsri, **A. Al-Bermani**, and R. Noé, "Fiber Nonlinearity Tolerance of SIM-OFDM in CO-OFDM", *Proc. Conf. 17th Opto-Electronics and Communications Conference (OECC 2012)*, 2-6 July 2012, Busan, South Korea.

A. Al-Bermani, C. Wördehoff, K. Puntsri, O. Jan, U. Rückert, and R. Noé, "Phase Estimation Filter Length Tolerance for Real-Time 16-QAM Transmission System Using QPSK Partitioning", *Workshop der ITG-Fachgruppe 5.3.1*, 5-6. July 2012, Gewerkschaftshaus Nürnberg, Germany.

K. Puntsri, V. Mirvoda, S. Hussin, O. Jan, **A. Al-Bermani**, M. F. Panhwar, and R. Noé, " A Low Complexity and High Accuracy Frame Synchronization for PolMux-Optical OFDM", *Workshop der ITG-Fachgruppe 5.3.1*, 5-6 July 2012, Gewerkschaftshaus Nürnberg, Germany.

A. Al-Bermani, C. Wördehoff, K. Puntsri, O. Jan, U. Rückert and R. Noé, " Real-time Synchronous 16-QAM Optical Transmission System Using Blind Phase Search and QPSK Partitioning Carrier Recovery Techniques ", *13. ITG-Fachtagung "Photonische Netze"*, 7.-8. May 2012 Leipzig, Germany.

O. Jan, M. El-Darawy, **A. Al-Bermani**, K. Puntsri, and R. Noé, " The Mitigation of Fiber Nonlinearities using RFP technique in CO-OFDM System ", *13. ITG-Fachtagung "Photonische Netze"*, 7.-8. May 2012 Leipzig, Germany.

O. Jan, M. El-Darawy, K. Puntsri, **A. Al-Bermani**, and R. Noé, " RF-pilot-based nonlinearity compensation in frequency domain for CO-OFDM transmission", *Proc. SPIE 8434-18*, Session 4, 16-18 April 2012, Brussels, Belgium.

A. Al-Bermani, C. Wördehoff, S. Hoffmann, U. Rückert, and R. Noé, "Nonlinear Effect of IQ Modulator in a Realtime Synchronous 16-QAM Transmission System", *Proc. IEEE Photonics 2011 Conference (IPC11)*, formerly (LEOS), 9 - 13 October 2011, Arlington, Virginia, USA.

K. Puntsri, S. Hoffmann, S. Hussin, **A. Al-Bermani**, and R. Noe, "A Low Complexity and High Accuracy Frame Synchronization for Optical OFDM Systems," *Proc. Conf. 16th Opto-Electronics and Communications Conference (OECC 2011)*, 4-8 July 2011, Kaohsiung, Taiwan.

A. Al-Bermani, C. Wördehoff, S. Hoffmann, U. Rückert, and R. Noé, " Synchronous 16-QAM Transmission in a FPGA-Based Coherent Receiver with Different Phase Estimation Filter Lengths ", *12. ITG-Fachtagung "Photonische Netze"*, 2.-3. May 2011 Leipzig, ITG-Fachbericht 228, ISBN 978-3-4007-3346-0, Germany.

A. Al-Bermani, C. Wördehoff, S. Hoffmann, K. Puntsri, U. Rückert, and R. Noé, " Realtime Implementation of Square 16-QAM Transmission System ", *Proc. SPIE 8065*, 806519 (2011), 28 March 2011, Strasbourg, France.

S. Hoffmann, **A. Al-Bermani**, C. Wördehoff, U. Rückert, and R. Noe, "Kohärente optische 16-QAM-Übertragung mit ressourceneffizienter Vorwärts-Phasenschätzung", *Workshop der ITG-Fachgruppe 5.3.1*, 14. Februar 2011, Technische Universität Dortmund, Germany.

R. Noé, S. Hoffmann, C. Wördehoff, **A. Al-Bermani**, and M. El-Darawy, "Advances in Coherent Optical Modems and 16-QAM Transmission with Feedforward Carrier Recovery", *Proc. SPIE 7960*, 79600L (2011), 25 January 2011, San Francisco, California, USA.

A. Al-Bermani, C. Wördehoff, S. Hoffmann, K. Puntsri, T. Pfau, U. Rückert, R. Noé, " Realtime 16-QAM Transmission with Coherent Digital Receiver ", *Proc. Conf. 15th Opto-Electronics and Communications Conference (OECC 2010)*, 5.-9. Juli 2010, Sapporo, Japan (7B4-2). *

A. Al-Bermani, R. Noé, S. Hoffmann, C. Wördehoff, U. Rückert, and T. Pfau, " Implementation of Coherent 16-QAM Digital Receiver with Feedforward Carrier Recovery ", *Proc. Signal Processing in Photonic Communications (SPPCom)*, Optical Society of America, SPWB5, 21-24 June 2010, Karlsruhe, Germany.

S. Hoffmann, C. Wördehoff, **A. Al-Bermani**, M. El-Darawy, K. Puntsri, U. Rückert, and R. Noé, "Hardware-effiziente Phasenschätzung für kohärenten QAM-Empfang mit regulären Stern-Konstellationen", *11. ITG-Fachtagung "Photonische Netze"*, ITG-Fachbericht 222, pp. 221-224, 3.-4. May 2010 Leipzig, Germany.

A. Al-Bermani, C. Wördehoff, T. Pfau, S.Hoffmann, U. Rückert, R. Noé, "First Realtime Synchronous 16-QAM Transmission with Coherent Digital Receiver", *11. ITG-Fachtagung "Photonische Netze"*, ITG-Fachbericht 222, pp. 153-156, 3.-4. May 2010 Leipzig, Germany.

R. Noé, U. Rückert, S. Hoffmann, R. Peveling, T. Pfau, M. El-Darawy, and **A. Al-Bermani**, "Real-time Implementation of Digital Coherent Detection", *Proc. European Conference on Optical Communication (ECOC2009)*, Tu5.4.3, 20.-24. Sept. 2009, Vienna, Austria.

* This paper received the IEEE Photonics Society Japan Chapter Young Scientist Award.

Table of contents

Glossary

Mathematical symbols

Variable	Description
Δf	Sum laser linewidth
η	Quantum efficiency of the photo diode
Φ_k	Phase error samples
φ_0	Initial phase offset after coherent detection
φ_{lo}	LO initial phase
φ_{nlo}	LO phase noise
φ_{ns}	Signal laser phase noise
φ_s	Signal laser initial phase
B	Number of test carrier phase angles
e	Electron charge
E_b	Energy power per bit
E_{in}	Unmodulated input electric field
E_{out}	Optical output signal of the IQ-modulator
f_c	Carrier frequency
G	Optical amplifier gain
h	Planck constant
i_n	Unity scale of the in-phase coordinate of a symbol
k_B	Boltzmann constant
M	Number of parallel modules
N	Filter half-width
n_{sp}	Spontaneous emission parameter
$P_{s,x}$	Power of the optical signal in the x-polarization
$P_{s,y}$	Power of the optical signal in the y-polarization
q_n	Unity scale of the quadrature coordinate of a symbol
R	Responsivity of the photodiode
r_{in}	Input load resistance
R_s	Symbol rate
t	Time
T_{abs}	Absolute temperature
T_s	Duration of one symbol
V_π	Voltage for π phase shift (MZM power transfer function)
ω	Angular frequency
ω_{lo}	LO angular frequency
ω_s	Signal laser angular frequency

Abbreviations

Abbreviation	Description
ADC	Analog to Digital Converter
ASE	Amplified Spontaneous Emission
ASK	Amplitude Shift Keying
AWGN	Additive White Gaussian Noise
BD	Balanced Detector
BER	Bit Error Ratio
BPS	Blind Phase Search
BPSK	Binary Phase Shift Keying
CD	Chromatic Dispersion
CPE	Carrier Phase Estimation
CW	Continuous Wave
dB	Decibel
DA	Data-Assisted
DAC	Digital to Analog Converter
DB	Duobinary
DD	Decision-Directed
DDMZM	Dual-Drive Mach-Zehnder Modulator
DFB	Distributed Feedback
DPMZM	Dual-Parallel Mach-Zehnder Modulator
DPSK	Differential Phase-Shift Keying
DSP	Digital Signal Processor
DSPU	Digital Signal Processing Unit
EAM	Electro-Absorption modulator
ECL	External Cavity Laser
EDFA	Erbium Doped Fiber Amplifier
ENoB	Effective Number of Bits
FEC	Forward Error Correction
FF	Feed-Forward
FPGA	Field Programmable Gate Arrays
FWM	Four Wave Mixing
I	In-phase
I/O	Input/Output
LINC	Linear amplification using Nonlinear Components
LO	Local Oscillator
M-QAM	M-ary Quadrature Amplitude Modulation
MZM	Mach-Zehnder Modulator
NRZ	Non-Return to Zero

OOK	On-Off Keying
PBC	Polarization Beam Combiner
PCB	Printed Circuit Board
PBS	Polarization Beam Splitter
PDM	Polarization Division Multiplexing
PE	Phase Estimation
PLL	Phase Locked Loop
PM	Phase Modulator
PMD	Polarization Mode Dispersion
PRBS	Pseudo Random Binary Sequence
PSK	Phase Shift Keying
Q	Quadrature
QAM	Quadrature Amplitude Modulation
QPSK	Quadrature Phase Shift Keying
QPSKP	QPSK Partitioning
RIN	Relative Intensity Noise
RX	Receiver
RZ	Return to Zero
SE	Spectral Efficiency
SMF	Single Mode Fiber
SNR	Signal to Noise Ratio
SOP	State of Polarization
SPM	Self-Phase Modulation
TX	Transmitter
VVPE	Viterbi and Viterbi Phase Estimation
VOA	Variable Optical Attenuator
WDM	Wavelength Division Multiplexing
XPM	Cross Phase Modulation

Chapter 1:

Introduction

1.1 Traffic evolution in data network

Optical components, systems and networks have evolved enormously since the beginning of the eighties to satisfy the traffic evolution in the data networks. With the creation of next generation optical communications systems exhibit single channels data rates of 40 and 100 Gb/s for long haul [1]. Therefore, before talking about technology lets talk about the motivation, why we are looking into all of this. The reason started from our human fundamental desire to interact. The information is of little use if we keep it to ourselves, and it is by very nature needed to be transmitted or communicated in order to be useful in order to make sense and that is the fundamental thing, or in other words no information means there is no modern life. It is expected that data traffic will increase exponentially due to the rapidly increasing use of high speed online services and broadband applications, such as cellular telephone, YouTube, Facebook, grid computing, data storage, teleconferencing, upcoming high definition video communication, and others [2, 3]. One of the best examples today is Panasonic life wall which is essentially a giant TV screen that filled the entire wall of a living room with the motivation to immerse yourself into the living room of another family; if we want this technology or not that is a secondary question because people will make us believe what we wanted. Today, we cannot live without smartphones anymore; so the same will happen when these advanced real-time applications that consume a huge amount of bandwidth, also we can expect that down the road 10 to 15 years we all have something like that in our homes. But going back to the evolution of data traffic so far, if we look into some statistics, what can be found from services is that we all know and love like Internet, YouTube, Facebook and so on; that is what fuels the historic capacity growth in network. Therefore it is no exaggeration to say that we cannot live without information, where we cannot live without optical fiber communication.

Figure 1.1 shows the growth of traffic capacity in the US network and it shows that network traffic is growing very fast [4]. The whole thing is true for the whole geographic

region, while the slopes might be slightly different maybe between 30 to 60% per year and all of these rates depend on the nature and penetration of services offered by network operators in different geographic regions [5, 6]; but in general we have very fast growth of traffic capacity. This yearly growth rate is close to 60% or 10log(1.6) which is 2dB, as shown in Figure 1.1 in the US network. So we have 2dB/year traffic growth fueled by human desires into interact.

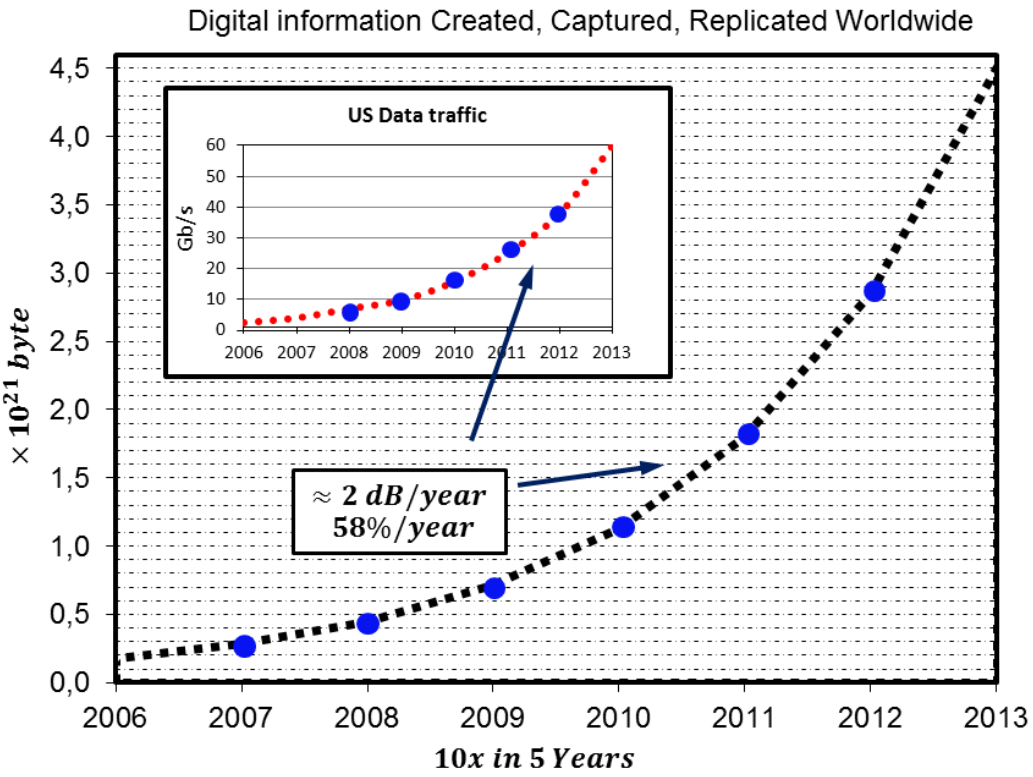

Figure 1.1: Network traffic growth [5, 6].

Now interestingly not just humans want to talk but computers also want to talk, and there is a very fundamental rule which is called ‘‘Amdahl’s rule of thumb’’ in computer engineering [7]. It shows that one floating operation that is processor can handle (flop) triggers ~ 1 Byte/s of transport; this factor of proportionality might differ between applications (what the computer are used for and what programs are running). But the important point is the linear proportionality [7, 8]. So this floating point operation triggered bandwidth is usually going over the printed circuit board (PCB) linking the ram chip with another chip with the processor, linking all I/O devices, and all storage devices on the PCB. I introduce this because we are now entering cloud computing and cloud services. The cloud services are giant distributed computer, where we have I/O processes, memory and storage going on everywhere in the network, and the role of these printed circuit board

traces is now probably being taken over by the transport network. So whatever we see from the scaling of the bandwidth in the PCB we should expect to take place in cloud services in the network as well. So as we move more and more into cloud services, this driver ‘‘Amdahl’s rule of thumb’’ will drive network traffic and if we look to the evolution of floating point operations per second of top 500 supercomputers, we will see a very nice exponential scaling which is about 86%/year or 2.7dB/year, as shown in Figure 1.2 [9].

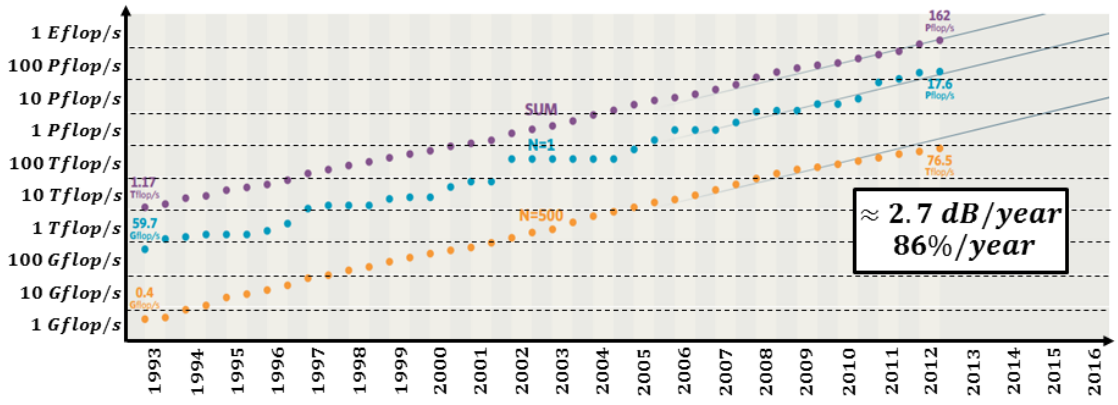

Figure 1.2: Fastest 500 supercomputers [9].

An important question come to our mind is that (do we know that this is driving data traffic in networks at that rate?), and the answer is No. This is because cloud services are only starting to catch on now, but with very high confidence one should expect growth of data network of about 2.7dB/year. Furthermore, most companies that run data services like Google, and others are expect growing rates somewhere around that (like 2.7dB/year) and not 2dB/year but something stronger [10]. So now the workhorse to make all that happen, to satisfy the demand for the exponentially growing bandwidth, has to be the optical network, and this fact is true since the nineties or even earlier.

Figure 1.3 shows a generic picture of how optical networks look like. Packet routers are used because everything is IP, where the data gets dumped into the network then the router is usually hooked up into the WDM system through a client interface which is a short-reach very cheap interface and runs today at 100 Gb/s or (4×25 Gb/s). We have heard about 100Gbit Ethernet standard but in fact there is no 100Gb/s flow anywhere in the network, it is 4×25 Gb/s on the client interface on four different wavelengths or 10×10 Gb/s on multimode fiber. The WDM system will convert that data into a very high speed quality. The WDM interface can go for very long distances. One can pack a lot of those signals onto one optical fiber, and this known as the line interface [10]. The line

interface currently also runs at about 100 Gb/s. Then the data is dropped into fiber through add/drop multiplexers. Maybe there are 100 wavelengths going over one single optical fiber, so that one can get 10 Tb/s, and this goes into the network through various optical add/drop modes to route the wavelengths to different points in the network. On the other side the exact same happen in reverse order.

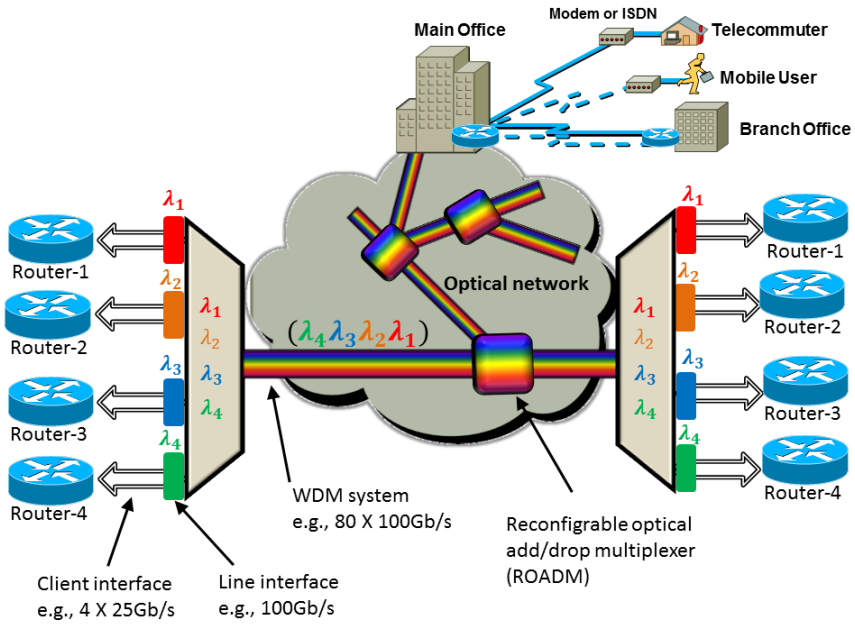

Figure 1.3: Optical networks: workhorse of the internet.

It is important to know how to increase the capacity of the line interface and the WDM system to meet the exponentially growing bandwidth demands of future data application. The next chapter shows how to scale the bandwidth of those line interfaces and how to make them faster, as routers want to process and put more data.

1.2 Outline of the thesis

In this chapter, a description of the current situation of traffic growth and a short presentation of the optical network is given; Later the social demand is described and how to meet the exponential bandwidth growth for future applications.

Chapter 2 shows the evolution of digital optical modulation, from on-off Keying (OOK) with direct detection receivers to multi-level modulation formats using coherent transmission. Also, the recent results of capacity limitations of single-mode fibers are shown and how to increase the spectral efficiency by comparing different modulation formats and how to provide a cost-effective transport infrastructure.

Chapter 3 explains the general principle of the 16-point quadrature amplitude modulation (16-QAM) transmitter. It provides all information which is relevant of the modulator function and includes the selection of optimal operation points in optical and electrical transmitter parts. Moreover, the electrical field of the optical transmitter signals has been derived analytically, and differences of signal characteristics have been emphasized.

Subsequently, chapter 4 illustrates different receiver concepts which can be employed to detect optical higher-order modulation signals, starting with optical frontends and ending with electrical data recovery. Furthermore, various feed-forward phase recovery algorithms for 16-QAM systems have been presented as the QPSK partitioning (QPSKP) and the blind phase search (BPS). Finally, the algorithmic and technological requirements for real-time 16-QAM transmission have been presented.

Chapter 5 presents the hardware implementation and the measurement results of a 16-QAM transmission system with feed-forward real-time synchronous demodulation and data recovery based on a field-programmable gate array (FPGA) for digital signal processing. Furthermore, the two techniques of carrier phase estimation (CPE) have been implemented and investigated in a real-time transmission, where the performance of them is presented.

Finally, the achieved results are discussed by a summary.

Chapter 2:

The evolution of optical transmission technologies

2.1 High-speed interface using coherent detection

The age of direct detection was the age until the middle of the 2000s where everything was OOK. The first 100 Gb/s interface was made in 2005 where still OOK was used so they switched a laser on and off by very fast electronics using very fast modulators [11–13]. Then coherent detection came and stayed. So it really is driving everything in optical communications at least on line interface side but not on the client interface. A lot of groups, very often in industry, have jumped onto this train and the University of Paderborn was the first to achieve real-time quadrature phase shift keying (QPSK) transmission with digital feed-forward carrier recovery [14, 15]. But the first report for that which demonstrated 100 Gb/s very impressively is by C. Fludger [16] and that marks the transitions for 100 Gb/s to move to coherent detection and to higher spectral efficiency (SE). Therefore, the real motivation to go to coherent detection was to put 100 Gb/s channels on a 50 GHz WDM grid without too much problems and allowing for a long haul reach; so QPSK and polarization multiplex using both polarization of light traveling through the fiber, that has made coherent so attractive. Furthermore, coherent has a couple of other very nice benefits, and people who operate optical networks might say this is the most important, but the fundamentally most important thing is the SE. Furthermore, for planning, operation and management, linear impairments can now be very easily compensated, because the coherent receiver translates the entire of optical field (electrical field of optical signal) into the electronic domain and then can do all kinds of polarization mode dispersion and chromatic dispersion compensation. An interesting thing is that coherent receiver which are introduced can be a little worse concerning speed because this first 100 Gb/s interface that is shown in Figure 2.1 is on two polarizations, and for one polarization, there is just a 50 Gb/s interface, and in the electrical domain, real and imaginary part of the optical field or I and Q component are needed and they are both on 25 Gb/s (or 28 Gb/s with overhead). Now, electrically this is a 4×25 Gb/s interface and it is the same as client interface. The symbol rate of QPSK signal has been moved up

to 56 Gbaud and later to 80 Gbaud, and it was the highest one with all electronic processing. Figure 2.1 shows that technology is almost back to where it was in 2005, where switches and electronics moved at 100 Gbaud, but the best change happen is now the transmission has been done in multilevel and coherent.

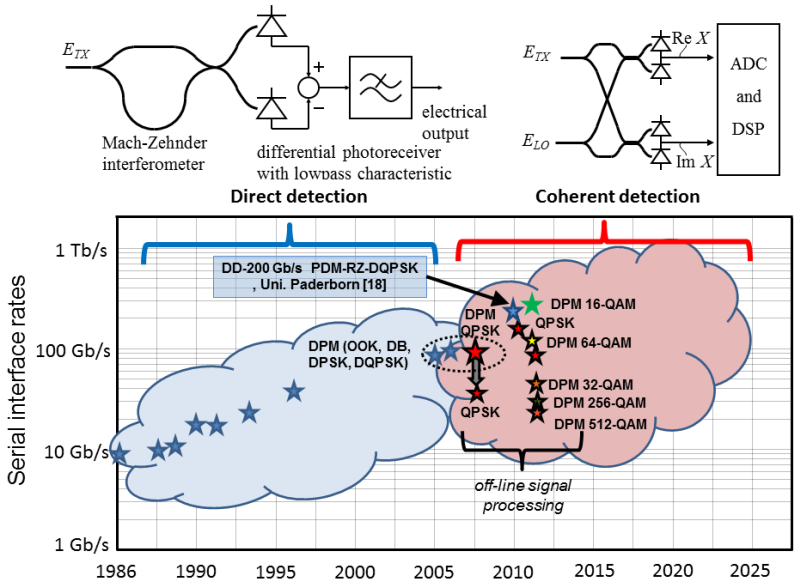

Figure 2.1: Optical transmitters, direct detection vs. coherent detection [17, 18].

The highest bit rate with a single wavelength interface that has been shown is 640 Gb/s for dual polarization or 320 Gb/s per polarization, as shown in Figure 2.2 [19–25]. Therefore, coherent detection with quadrature amplitude modulation is now on track to scale the interface rates to higher levels.

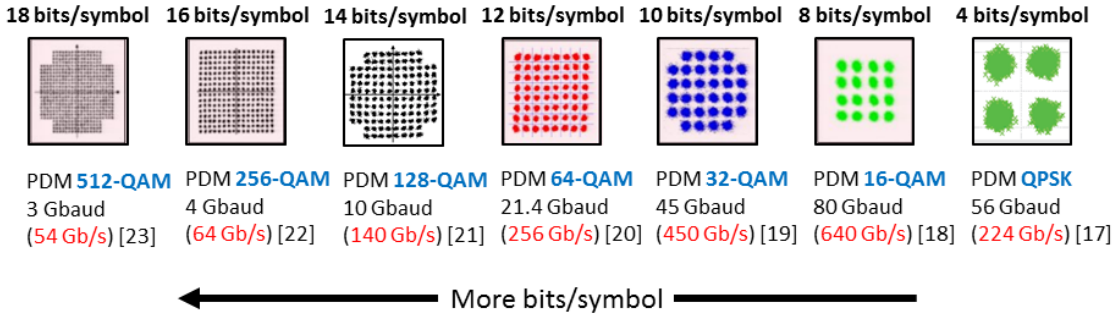

Figure 2.2: Higher interface rates via higher-order modulation using off-line signal processing.

Today, the age of 100 Gb/s has officially arrived because this coherent system now offered by many manufacturers. In 2008 and later in 2010, there are commercially available 11.5 GBaud and 28 GBaud QPSK line interface products based on custom designed CMOS ASICs to handle the massive required DSP functions for adaptive polarization

tracking, chromatic dispersion compensation, and forward-error correction (FEC) [10]. This PDM-QPSK 100 Gb/s interface with a very powerful ASIC has more than 70M gates. In 2012, Ciena announced new generation coherent optical chipset (WaveLogic 3) [26] the industry's first software-programmable coherent technology that scales to 400 Gb/s. This coherent optical processor can support multiple coherent modulation formats BPSK, QPSK and 16-QAM (i.e. DP 16-QAM for 200 Gb/s at metro and regional distances (2 × 100 Gb/s waves in a single 50 GHz space) also dual-channel DP 16-QAM for 400 Gb/s at metro and regional distances).

Again, electrically what they did is not a 100 Gb/s but a 4 × 25 Gb/s, and this parallelism, what is seen here, started actually in the microprocessor industry. The clock speed could not cranked up for very different reasons, but the microprocessor went to parallel architectures (i.e. multi-core processor architectures) and that is the parallelism which is exact the same thing what happened in Figure 1.3, because one cannot do a 100 Gb/s in a viable fashion but easily can go to 4 × 25 Gb/s by exploiting I&Q (real and imaginary part of the field) and exploiting the two polarizations that propagate in a single mode fiber. Therefore, that theme of parallelism will stick, so there can be scaled but more and more parallelism is needed.

2.2 The evolution of coherent optical multilevel formats

There are several options to increase interface rates: (i) one can just go to highest speeds (just try to switch faster and faster) which can be seen in the baud rate or symbol rate (the rate at which the symbols are sent one after the other) could go higher and higher, (ii) another solution is to go to multiple carriers to create an effective super channel, or (iii) one can pack more bits into one symbol and go to higher density of QAM, as shown in Figure 2.3.

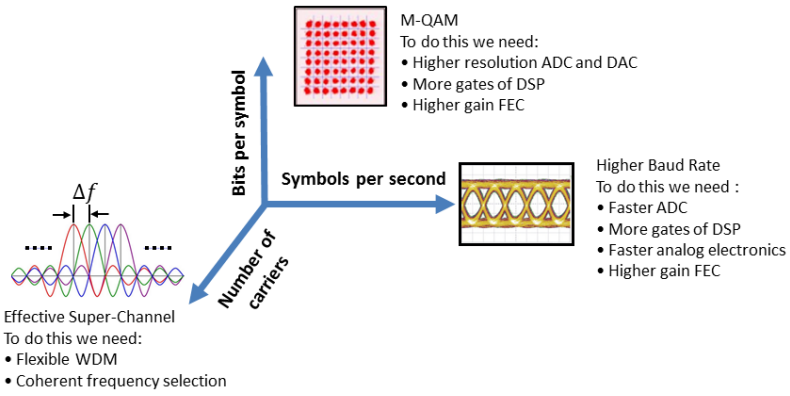

Figure 2.3: Three levers to increase data rates.

Looking into the constellation maps in Figure 2.2, there can be seen that the dots in the complex plane of the optical field represent many bits, for QPSK, there are 2 bits per point and per polarization that can be sent. For 64-QAM there will be 6 bits per point per polarization. Therefore, the more points one have the more bits are packed into one symbol. In addition, an interesting thing that can be seen from all of these off-line experimental demonstrations shown in Figure 2.2 is that the highest speed has been achieved by sticking to relative moderate constellation size at high symbol rates. For the very high order modulation at low symbol rates, the aggregate interface rate is not that high, and there is a very fundamental reason for that which is the scaling. Increasing the speed to twice the symbol rate leads to twice the bit rate, so it's a linear scaling; Increasing the constellation size into double number of points, just one bit per symbol more is got, so there is a logarithmic scaling. So a very different scaling that rules here and it turns out that 16-QAM is a pretty good choice.

2.3 Technology scaling of ADC

There are certain factors that also favor the choice of a relatively low order modulation format. The higher-order modulation requires a higher effective number of bits (ENoB) in digital-to-analog and analog-to-digital conversion (DAC, ADC) [27]. In [28], the increase in ADC requirements for M-ary quadrature amplitude modulation (M-QAM) is shown. Furthermore, in [29, 30], Walden has made many observations about technology for scaling of analog-to-digital converters, and all these higher-order modulation formats have a lot to do with analog-to-digital conversion, because symbols have to be generated which afford several levels at the transmitter and the receiver. So, Walden shows in [29, 30] that for every bit of higher analog-to-digital resolution (for every bit reduced from the ADC), the ADC bandwidth is halved. The number of amplitude levels and quantization levels in M-QAM increases by a factor of $(sqrt(sqrt(2)))$. The difficulty of building a high-speed analog-to-digital converter rises linearly with the number of quantization levels. Usually, one is much better to go to a higher speed combined with lower resolution than going to lower speed with higher resolution aiming to interface rates and not to SE.

2.4 SE of multilevel modulation format and Shannon Limit

In M-QAM the number of points in the grid is usually a power of 2 $(2, 4, 8, ...)$, which is called $2^m - $ QAM. Figure 2.4 shows the constellation diagrams for a variety of modulation formats: conventional OOK, differential phase-shift keying (DPSK), duobinary (DB),

$2^4 -$ QAM and $2^8 -$ QAM. Figure 2.4 shows the advantage of using $2^m -$ QAM which is able to carry *m* bits per symbol, so it can do *m* times the SE compared to binary intensity modulation. Table 2.1 shows that the transmission rate will increase if higher *m* values are selected.

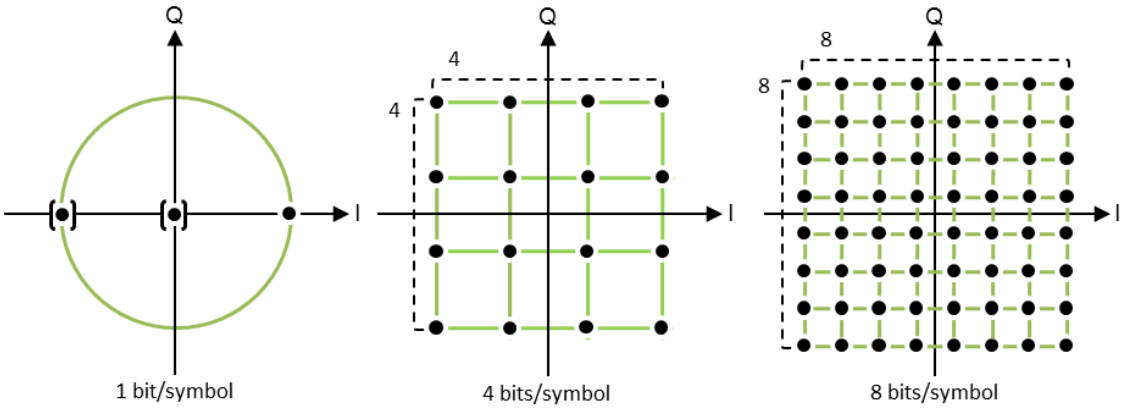

(a) OOK, DPSK, DB (b) 16-QAM $(4 \times 4 = 2^4)$ (c) 64-QAM $(8 \times 8 = 2^8)$

Figure 2.4: Constellation maps for OOK, DPSK, DB (a), $2^4 -$ QAM (b), and $2^8 -$ QAM (c).

Table 2.1: Bit rates of different forms of QAM and conventional OOK.

Modulation	No. of bits/symbol	Symbol rate
OOK	1	$1 \times bit\ rate$
4-QAM	2	$1/2 \times bit\ rate$
8-QAM	3	$1/3 \times bit\ rate$
16-QAM	4	$1/4 \times bit\ rate$
32-QAM	5	$1/5 \times bit\ rate$
64-QAM	6	$1/6 \times bit\ rate$
128-QAM	7	$1/7 \times bit\ rate$
256-QAM	8	$1/8 \times bit\ rate$
512-QAM	9	$1/9 \times bit\ rate$
1024-QAM	10	$1/10 \times bit\ rate$

The bit error rate (BER) formula for coherent synchronous detection systems and square M-QAM signals is shown in equation (2.1), more details can be found in [31–33].

$$BER_{M-QAM} \approx \frac{2\left(1-\frac{1}{\sqrt{M}}\right)}{\log_2(M)} \cdot erfc\left(\sqrt{\frac{3\,SNR}{2(M-1)}}\right) \tag{2.1}$$

Figure 2.5 shows the BER of square M-QAM as a function of energy to noise power per bit E_b/N_0 which is signal-to-noise ratio (SNR) per bit. Figure 2.5 also shows that higher order modulation requires larger SNR per bit to achieve the same BER.

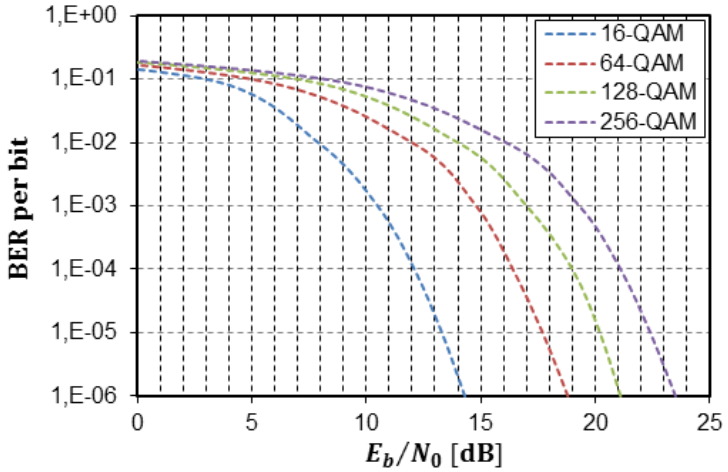

Figure 2.5: BER of M-QAM as a function of SNR per bit.

Another important thing is the SNR, so equation (2.2) computes the ultimate SE and the required E_b/N_0, this equation known as Shannon-Hartley theorem [34]:

$$\frac{C}{W} = \log_2\left(1 + \frac{E_b}{N_0}\frac{C}{W}\right) \tag{2.2}$$

The plot in Figure 2.6 shows the very fundamental Shannon limit and it shows a trade-off between SE and the required SNR per bit. The E_b/N_0 is plotted for a BER $= 10^{-4}$ by assuming synchronous detection. The SE comes at a fundamental cost for M-QAM, where high SNR is required as the value of M is increases, and it becomes closer to Shannon limits than other formats.

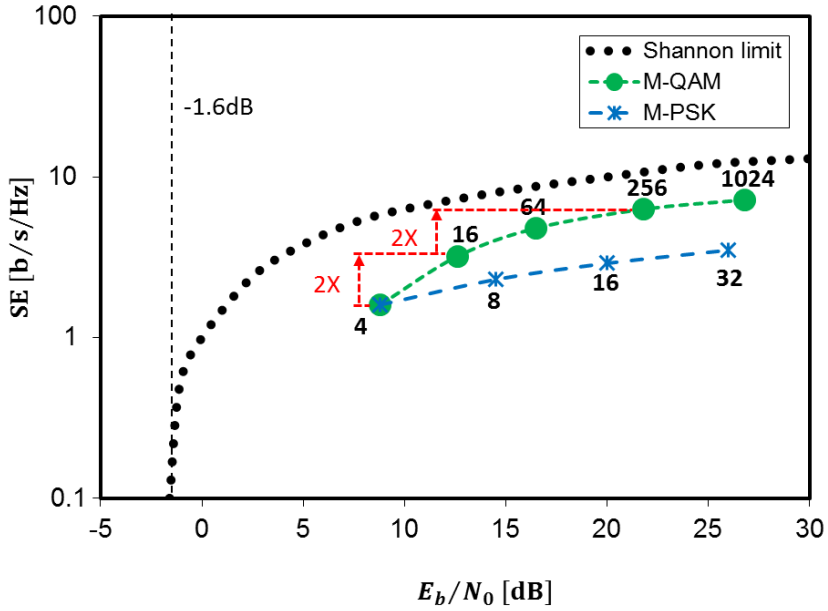

Figure 2.6: Spectral efficiency versus sensitivity of M-QAM.

From Figure 2.6 the QPSK (4-QAM) signal with four constellation points has a certain SNR to operate and SE about 2 b/s/Hz. To double the capacity in the optical network, one should go to 16-QAM, and that comes by the cost of more SNR. In reality, approximately 7 dB more SNR required for doubling the capacity. To achieve these more SNR, better amplifiers are needed, lower fiber loss, more launch power and a fiber with less nonlinearity. So there are several options to vary to get these more SNR out of the system, and that means optical line design (i.e. optical line design is very important here). To double the system capacity again we should go to 256-QAM and to do this we need more SNR, there one will reach the point of diminishing returns, also we cannot get these more SNR easily. That is far beyond just tweaking the line; in this case the region distance has to be shortened. Furthermore, to increase symbol rate and/or number of bits within one symbol, this may affect the signal launch power to the fiber without generating excessive nonlinear signal distortions [35, 27]. So from this sense 16-QAM is a pretty good compromise between the required SNR and the SE.

Chapter 3:

16-QAM transmitter design

The Square 16-QAM constellation was introduced for the first time by Campopiano and Glazer in 1962 [36]. Today, it has become a well-known modulation format and widely used in electrical systems, while for optical transmission systems, this format was still very distant from a commercially practical implementation until 2012 when Ciena showed a real-time coherent technology that scales to 400 Gb/s over metro and regional distances [26]. In the later sections, the fundamental key components of optical transmitter for 16-QAM modulation are shown.

3.1 Concepts of optical modulation

The first part in the optical system is the transmitter, which is used to convert the electrical signal into the optical form and launch it into the optical channel. The technology of optical transmitter can be divided into two categories: (i) direct modulation and (ii) external modulation, as shown in Figure 3.1.

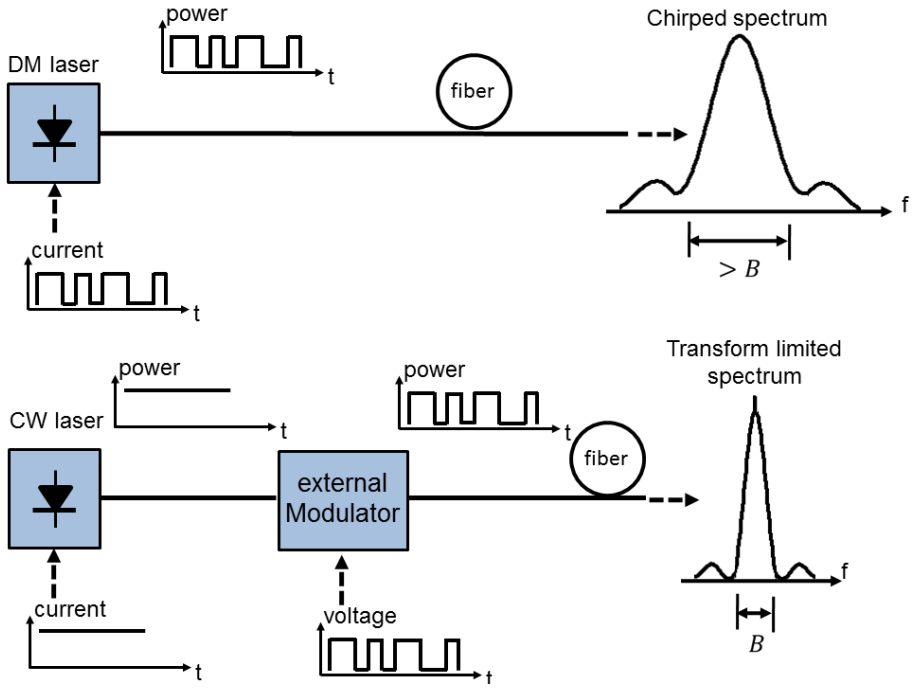

Figure 3.1: Optical transmitters, direct modulation (top) vs. external modulation (bottom).

In the direct modulation scheme, the data signal is modulated on the laser drive current. This type of modulation is simple and low cost but has a limited application in modern communication due to the narrow modulation bandwidth of lasers and the generation of frequency fluctuations by time, called laser chirp. To avoid this effect, an external modulation can be employed to produce higher-quality optical pulses where a combination of a laser which acts as continuous wave (CW) light source followed by an external modulator which switches the optical power on or off according to the data stream. Furthermore, in external modulation all data can be transferred from optical domain into electrical domain, where optical equalization of chromatic dispersion (CD) and polarization mode dispersion (PMD) in the electrical domain become possible.

Two kinds of external modulators are commonly used, Mach-Zehnder modulators (MZM) and electro-absorption modulators (EAM) [37]. MZMs have better transfer characteristics where the electrical drive voltage is used to control the frequency chirp. On the other hand EAMs can be easily integrated together with the laser source on the same chip which requires careful characterization, but they have an intrinsic chirp. In addition, the characteristics of EAMs have nonlinear transmission-voltage and voltage-dependent chirp [38]. An important parameter for the transmitter is the launch power, since more launch power means more spacing between the preamplifiers. Furthermore, various nonlinear effects limits will appear when the input power is increased. Figure 3.2 shows different optical modulator structures and the complex amplitude diagrams [3].

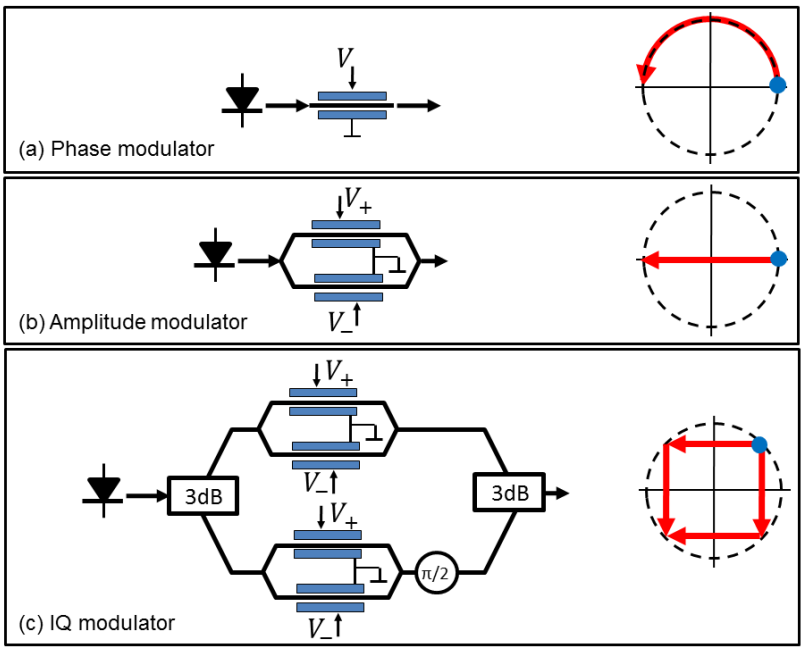

Figure 3.2: Types of optical modulators.

3.2 System performance parameters on signal degradation

There are several limitations of the system performance which forces us to migrate to higher-order modulation formats. Tendencies regarding relevant electrical and optical components, also system parameters such as laser phase and amplitude noise, laser linewidth requirements, transmitter chirp and fiber propagation effects have to be taken into account. For high-speed data transmission large signal bandwidths have to be handled which will increase the requirements on electrical drivers and electrical to optical interconnects. The electrical components will generate signals with noise, time jitter, and imbalance between rise and fall time. The electrical to optical components are limited by their maximum driving speed where any difference between electrical and optical velocities leads to some distortions of the signal [39].

In practical systems, laser noise has to be taken into account. Due to spontaneous emission taking place inside semiconductor optical light sources, photons with intensity fluctuations and random phase fluctuations are added to the coherent output field. The relative intensity noise (RIN) can lead to significant degradation in optical system performance, especially for coherent detection with local oscillators (LO) and absence of balanced detection [40, 41]. The amount of RIN is independent of attenuation along optical channel as both signal and noise powers are attenuated equally. Furthermore, transmission capacity and carrier to noise ratio are limited by RIN. In the simple system level modeling approach, the intensity fluctuations can be modeled with Gaussian statistics and a white noise spectrum [42, 43]. The spectral linewidth of a laser is defined as the full-width at half-maximum bandwidth of the CW spectrum. However, phase fluctuations will increase with the increase of the spectral linewidth of a laser. Furthermore, laser phase noise is critical for higher-order modulation with a high number of bits per symbol especially when the symbol rate is reduced.

During fiber transmission, there will be interactions between transmitter chirp and fiber degradation effects (linear and nonlinear effects) which can have a strong impact on transmission system performance. Most of the degradation of a fiber link results from (i) fiber attenuation, (ii) Kerr nonlinearities, (iii) chromatic dispersion, (iv) polarization mode dispersion, (v) nonlinear scattering effects and (vi) nonlinear phase noise. However, the combination of frequency chirp with CD has a critical effect on channel transmission performance. Optical amplifiers are used to compensate for the attenuation of transmission system; this means for long distance one need several cascaded sections (fiber link with

optical amplifier) which add noise of the amplifiers. All impairments induced by nonlinear effects depend on the type of the transmitted signal. The Kerr effect of an optical fiber implies all the nonlinear response creating from the intensity dependence of the refractive index. Kerr nonlinearities have three propagation effects depending on the transmission scenario. Firstly, self-phase modulation (SPM) which means phase variation depending on the power variation over time. Secondly, cross phase modulation (XPM) where the phases of the propagating channels are shifted because of power fluctuations of the neighboring channels and this has double of effect than SPM. The third one is four wave mixing (FWM) where spurious frequencies are generated by the interaction of two or more propagating wavelengths with high power. Two other nonlinear scattering effects of the fiber channel are Raman and Brillouin scattering where both phenomena mean an intensity-dependent attenuation of the signal wave [44].

3.3 Transmitter configurations for square 16-QAM

The constellation diagram of square 16-QAM shows that 4 bits are mapped to one symbol, and the symbols have 12 phase and 3 amplitude states. There are several possible transmitter configurations for square 16-QAM (see Appendix). These methods can be categorized according to electrical driving signals to the optical modulator: i) electrical multilevel drive signals, and ii) electrical binary drive signals. Figure 3.3 shows possible implementations for an optical square 16-QAM transmitter.

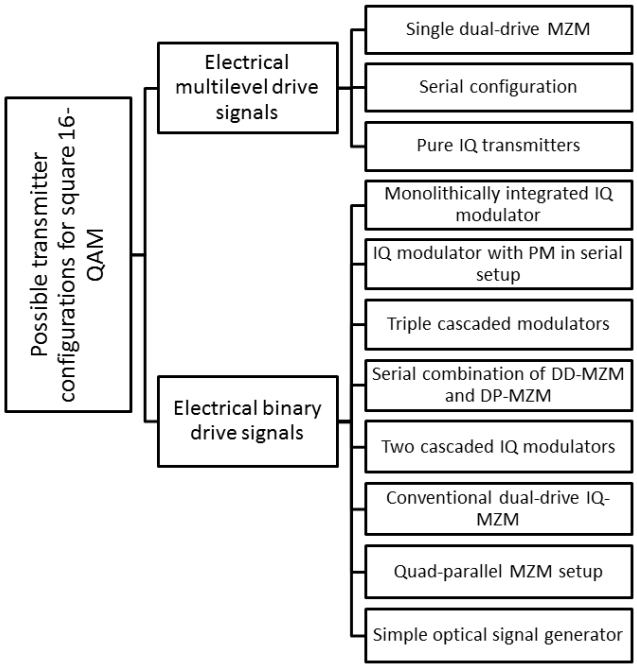

Figure 3.3: Optical square 16-QAM transmitters, more details are shown in the Appendix.

The common structures from these several possible implementations are presented in Figure 3.4. The optical part is composed of one or more fundamental external optical modulator structures.

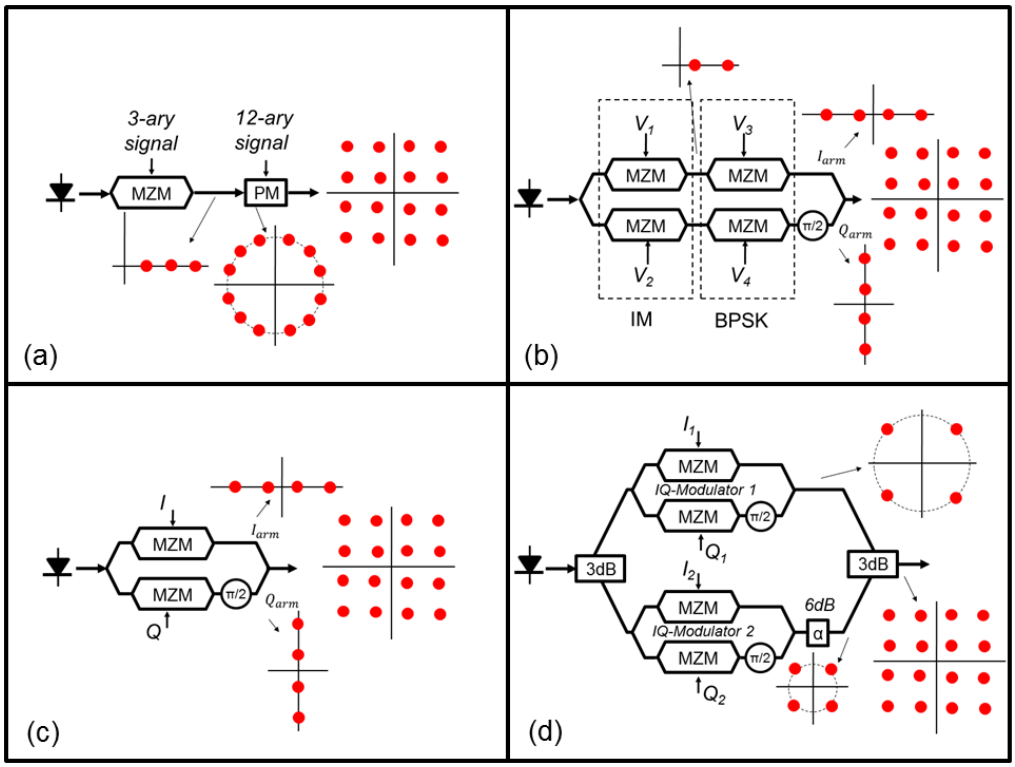

Figure 3.4: Optical square 16-QAM transmitters; serial MZM with PM (a), monolithically integrated IQ modulator (b), conventional IQ setup (c), and quad-parallel MZM setup (d).

The serial square 16-QAM transmitter contains a MZM and a phase modulator (PM) in series shown in Figure 3.4(a). This structure features a simple optical part, but phase modulation requires a 12-ary electrical driving signal. High-speed DAC with high-resolution are required to perform electro-optical (E/O) interfacing. Using separate serial structures for I and Q modulation displayed in Figure 3.4(b) leads to a higher optical complexity and necessitating integration, but allows binary input levels. Phase modulators in the 16-QAM transmitter structure temporarily yield to high optical power, where phasors with amplitudes greater than one are possible during the symbol transitions [45]. In contrast pure IQ transmitters shown in Figure 3.4(c) are composed of two arms, leading also to a bigger optical complexity, but the electrical driving signals manage with four levels. Combining two IQ transmitters to a quad-parallel MZM proposed in [46] and presented in Figure 3.4(d) allows again binary driving signals at the costs of the highest optical complexity of all four structures but provides the best performance for high baud rates with respect to E/O interfacing. In pure IQ transmitters there will be symbol

transitions through zero in the constellation diagrams. Conventional IQ setup will be used in all experiments of this dissertation because it has lower electrical and optical complexity.

3.4 Optimal transmitter condition

3.4.1 Quadrature modulator

In digital optical communication with square 16-QAM modulation, the constellation points are usually arranged in a square grid with equal vertical and horizontal spacing. Section 3.3 shows that the most commonly structure used for optical QAM modulation is the IQ-modulator. This modulator is composed of a Mach-Zehnder interferometer which contains two MZMs which operate in the push-pull mode at the minimum transmission point [47] [48], one MZM in each arm, and a PM that introduces a phase difference between the two arms. The incoming light is equally split into two arms, the in-phase (I) and the quadrature (Q) one.

Figure 3.5 shows two different MZM operation principles. Firstly, to achieve a modulation in intensity the MZM should operate at the quadrature point, since the DC bias is set to $-V_\pi/2$ and get V_π peak-to-peak modulation. Secondly, the MZM will operate at the minimum transmission point when the DC bias is set to $-V_\pi$ and we will get $2V_\pi$ peak-to-peak modulation, a phase skip of π occurs when crossing the minimum transmission point. This becomes more clearly from the field transfer function shown in Figure 3.5. By this way, the MZM can be implemented for binary phase modulation and for modulation of the field amplitude in each branch of an optical IQ-modulator [43].

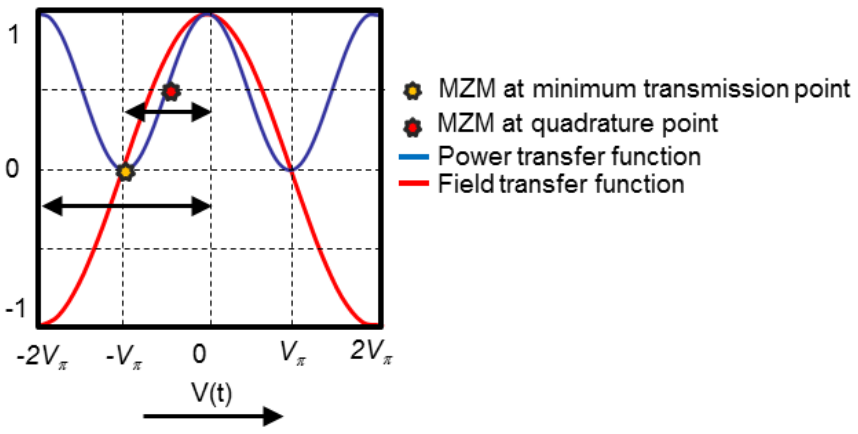

Figure 3.5: MZM operation points.

Figure 3.6 shows optical square 16-QAM transmitter structure. The incoming light is equally split into two arms (I and Q). It is assumed that the input into the IQ-modulator is an unmodulated optical wave which can be expressed in complex notation as

$$E_{in}(t) = \sqrt{2P_s}e^{j(w_s t+\theta_s)} \cdot e_s \tag{3.1}$$

where P_s is the average optical power, $w_s/2\pi$ the frequency, θ_s is the initial phase and e_s the polarization of transmitted laser. In equation (3.1) the effect of intensity and phase noise of the laser has been neglected. The optical output signal of the IQ-modulator $E_{out}(t)$ can be written as a function of the unmodulated input electric field $E_{in}(t)$:

$$E_{out}(t) = \frac{j}{2}e^{-j\frac{\pi V_{PM}}{2V_{\pi PM}}}\left\{\sin\left(\frac{V_i(t)}{2V_{\pi i}}\pi\right) - e^{-j\frac{V_{PM}(t)\pi}{V_{\pi PM}\ 2}}\sin\left(\frac{V_q(t)}{2V_{\pi q}}\pi\right)\right\}E_{in}(t) \tag{3.2}$$

where $V_i(t), V_q(t), V_{PM}$ are driving voltage and $V_{\pi i}, V_{\pi q}, V_{\pi PM}$ are the half wave voltages of the two MZMs and the phase shifter, respectively. All MZMs operate in push-pull mode and the voltage of the phase shifter is set at $V_{PM} = V_{\pi PM}/2$, in order to introduce the phase difference of $\pi/2$ between the two arms.

The ideal multilevel in-phase and quadrature driving voltages can be describe by

$$V_i(t) = \frac{2V_\pi}{\pi} \cdot \sin^{-1}\left(\sum_n \left(i_n \cdot p(t - nT_s)\right)\right) \tag{3.3}$$

$$V_q(t) = \frac{2V_\pi}{\pi} \cdot \sin^{-1}\left(\sum_n \left(q_n \cdot p(t - nT_s)\right)\right) \tag{3.4}$$

where V_π is the needed radio frequency voltage for phase shift π, $p(t)$ is the amplitude pulse shape, and i_n and q_n are the unity scale of the in-phase and the quadrature coordinate of a symbol, respectively [45]. One of the 16th symbols will map into symbol interval (denoted by the integer n) of one symbol length T_s.

3.4.2 Optimum driving voltage for IQ-modulator

For the generation of 16-QAM a field programmable gate arrays (FPGA) was used with modulator drivers, attenuators and resistive summers as illustrated in Figure 3.6 [49]. Firstly, four pseudo-random binary sequence (PRBS) signals are generated by an FPGA with output voltage levels of $\pm v$. One in each pair experiences a loss of $(-20\log(\alpha)(\text{dB}))$ to have voltage amplitudes αv and $-\alpha v$ $(0 < \alpha < 1)$ and is combined with the other

unattenuated signal using resistive summers. As a result, two four-level signals with the amplitudes of $\pm(1+\alpha)v$ and $\pm(1-\alpha)v$ are generated. The four-level signals are applied to both MZMs in the IQ-modulator.

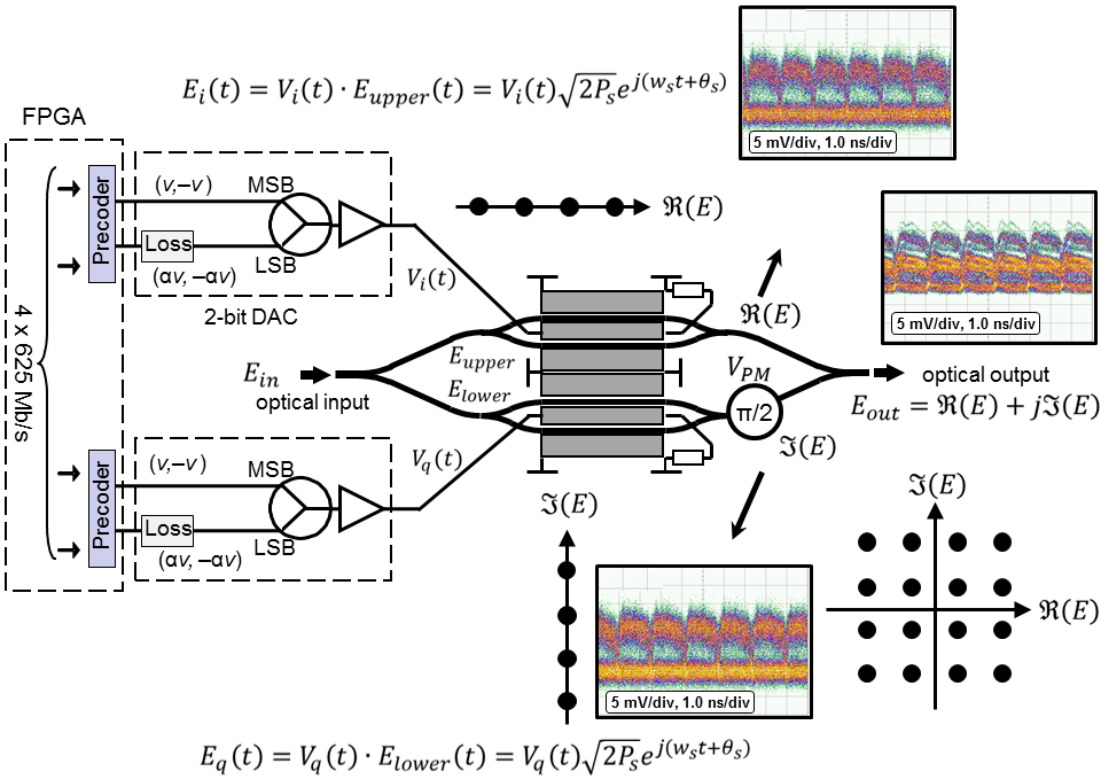

Figure 3.6: 16-QAM signal generation scheme with an IQ-modulator.

Figure 3.7 shows the characteristic response of the MZM when a driving voltage is applied and the DC bias voltage (V_{bias}) is set to null position. The transfer characteristic equation as a function of the applied voltage is

$$\frac{|E_{out}|^2}{|E_{in}|^2} = \sin^2\left(\frac{V_d(t)}{2V_\pi}\pi\right) \tag{3.5}$$

where $V_d(t)$ is the electrical driving voltage waveform, V_π is the voltage to turn the modulator from minimum to maximum transmission. The voltage amplitude can be defined as $(1+\alpha)v = \Delta V_\pi$ $(0 < \Delta \leq 1)$, the output intensity of the MZM shown in Figure 3.7 can be described by

$$P_1 = \sin^2\left(\frac{\pi}{2}\cdot\Delta\right) \tag{3.6}$$

$$P_2 = \sin^2\left(\frac{\pi}{2}\cdot\frac{(1-\alpha)}{(1+\alpha)}\Delta\right) \tag{3.7}$$

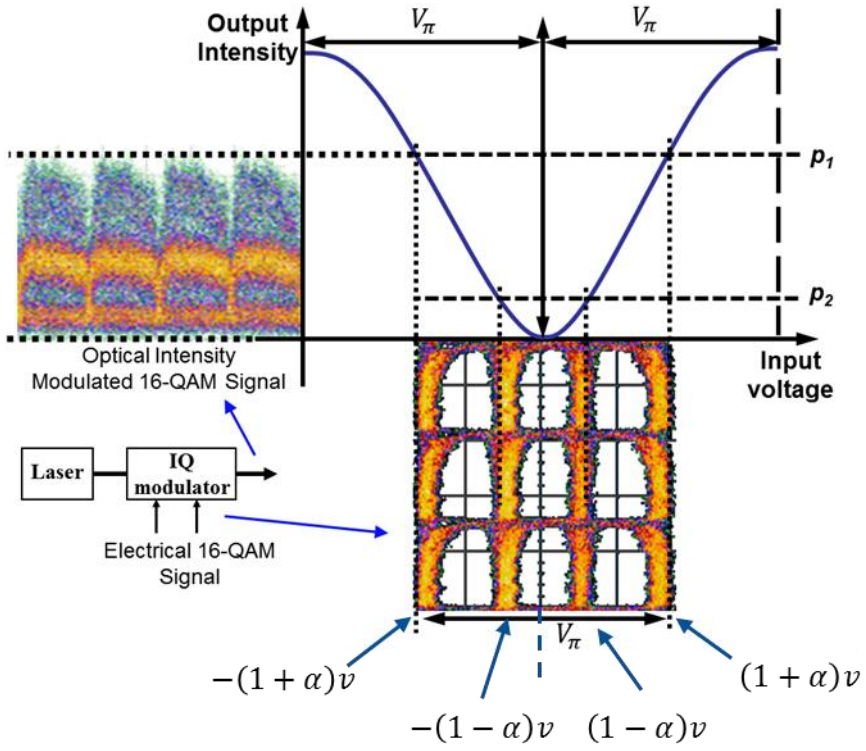

Figure 3.7: MZM transmittance for 16-QAM.

3.4.3 Extinction ratio of IQ-modulator

In optical transmitters, no matter of modulation type, some power is emitted when a zero is transmitted. This unwanted effect is defined as extinction ratio (ER):

$$ER = \frac{P(1)}{P(0)} \tag{3.8}$$

where $P(1)$ and $P(0)$ are the power levels corresponding to the ‘‘one’’ and ‘‘zero’’, respectively. For ideal transmitters the ER is infinite. Normally in modulator datasheet the ER is expressed in dBs where ($ER_{dB} = 10\log(ER)$ (dB)). The ER should be high enough to achieve a large separation between the power of the ‘‘one’’ and ‘‘zero’’, and ensure that very low power appears in the signal when a ‘‘zero’’ is transmitted [50]. Choosing a lower ER value leads to a swing decrease in the optical signal, even if the average power $P_{avg} = (P(1) + P(0))/2$ stays constant as shown in Figure 3.8(a&b). To overcome this problem (i.e. to recover the original signal swing), the average transmitted power can be increased as shown in Figure 3.8(c). If we assume that the receiver is limited to thermal noise, then power penalty can be derived as [44]

$$\delta_{ER}(dB) = 10\log\left(\frac{ER+1}{ER-1}\right) \tag{3.9}$$

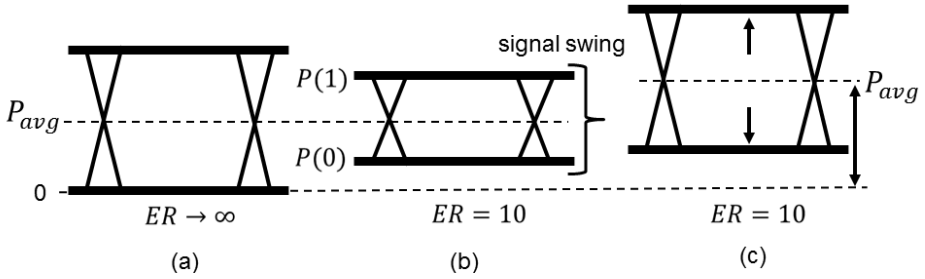

Figure 3.8: Eye diagram after optical transmitters for $ER \cong \infty$ (a), $ER = 10$ (b), and $ER = 10$ and increased average power.

In practical transmission systems, reducing the ER of the modulator will increase the received noise, because $P(0)$ is not zero so it will add more noise on the zeros, and also a lot of noise will be added onto the zeros and the ones due to optical amplifiers to restore the transmitted signal swing, necessitating to put more power to compensate for this noise. Therefore, power penalty of the ER becomes larger than given in equation (3.9). For the case that receiver noise is dominated by photo detector or preamplifier noise like electric noise power proportional to the received signal current [51], the power penalty can be written as

$$\delta_{ER}(dB) = 10\log\left(\frac{\sqrt{ER}+1}{\sqrt{ER}-1}\cdot\frac{ER+1}{ER-1}\right). \tag{3.10}$$

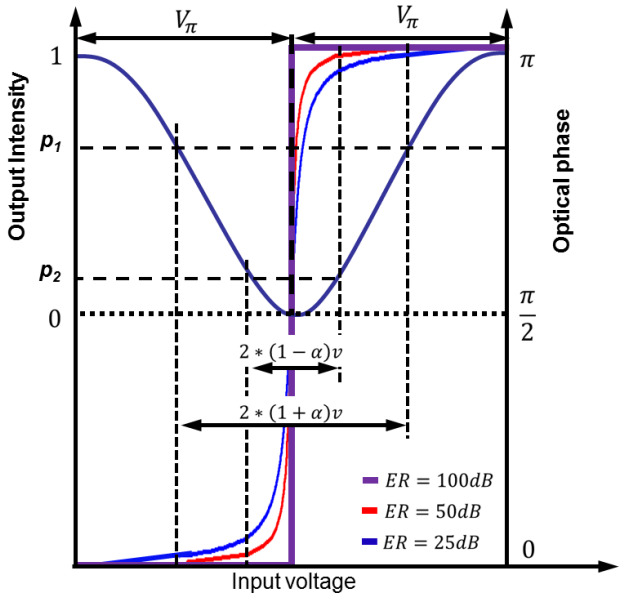

Figure 3.9: Characteristic response and the output optical phase of MZM when driving voltage is applied for different ER [52].

For example, two different IQ-modulators have been tested in an amplified lightwave system with 50 dB and 25 dB ER, and these cause a power penalty of up to 0.0275 dB and

0.5164 dB, respectively. Figure 3.9 shows phase transfer function of MZM for different ER values [52]. Kawanishi investigate in [53] the impact of parasitic phase modulation at MZMs on advanced modulation formats and he showed that phase error in the optical output increases with the ER of the modulator also he proved that $ER > 30$ dB is required for advanced modulation formats, such as 256-QAM. Due to unequal amplitude distribution of the two Mach-Zehnder arms the phase error becomes significant when the ER is small or the modulation signal amplitude is small [53]. Today, lithium niobate ($LiNbO_3$) MZM technology has an ER in the range of 20 ~ 50 dB. For a limited ER value (ie. $ER < 100$ dB) the optical phase of the MZM deviates from the ideal optical phase of ($0\ or\ \pi$) [52], as shown in Figure 3.9. The 12 phases and the 3 amplitudes of the square 16-QAM signal are affected by the characteristics of MZM.

3.4.4 Effect of MZM to 16-QAM

The influence of linear and nonlinear effects related to the IQ-modulator of a 16-QAM coherent transmission system has been investigated in a real-time transmission, as shown in Figure 3.10 [49]. The amplitudes of the MZM in the IQ-modulator need to be carefully adjusted to obtain a good pattern and to avoid phase distortions. Two different IQ-modulators with 50 dB and 25 dB ER have been tested. The 2.5 Gb/s signal was transmitted through 1.6 km of standard single-mode fiber (SMF). The characteristic response of the MZM is a nonlinear sinusoidal due to the applied driving voltage. Furthermore, a finite value of ER causes unwanted phase distortion in the optical output [53, 54]. All the MZMs are identical and the amplitudes of the electrical signals applied to the MZMs are the same. All receiver components will explain later in the next chapters.

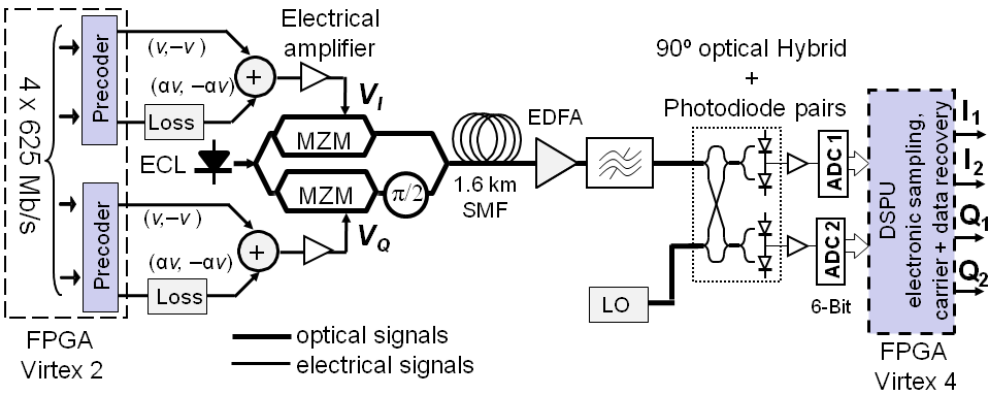

Figure 3.10: Self-homodyne 2.5 Gb/s 16-QAM transmission setup.

Figure 3.11 shows typical constellation maps and the eye diagrams of the 16-QAM patterns in the transmitter (electrically before the modulator) for different attenuators

values. The amplitude of the constellation map is affected severely when α is changed [49]. In Figure 3.12 the optical signal before transmission is plotted for different α and Δ values.

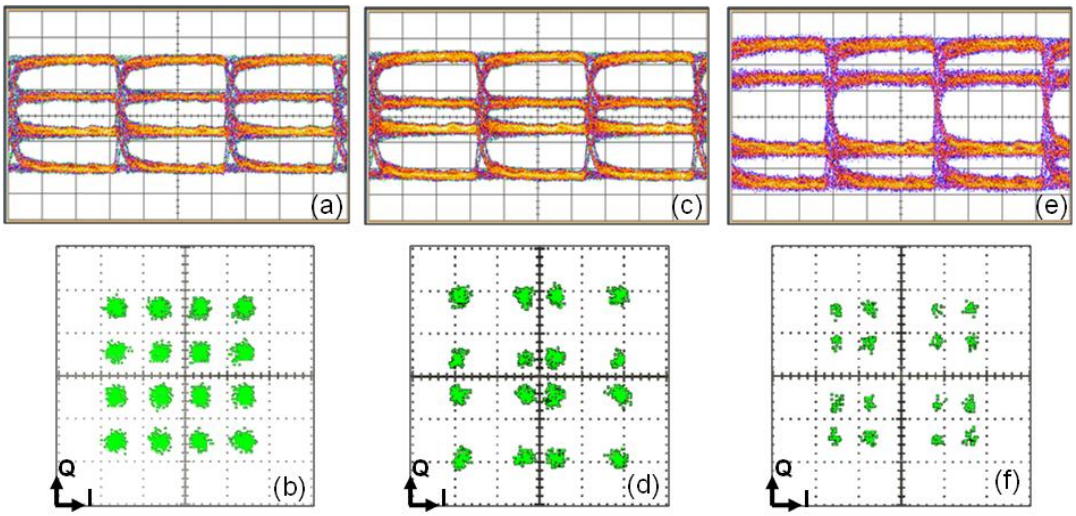

Figure 3.11: Electrical eye diagrams and constellation maps of 625 Mbaud 16-QAM. (a&b) $\alpha = 0.5$; (c&d) $\alpha = 0.7$ and (e&f) $\alpha = 0.35$.

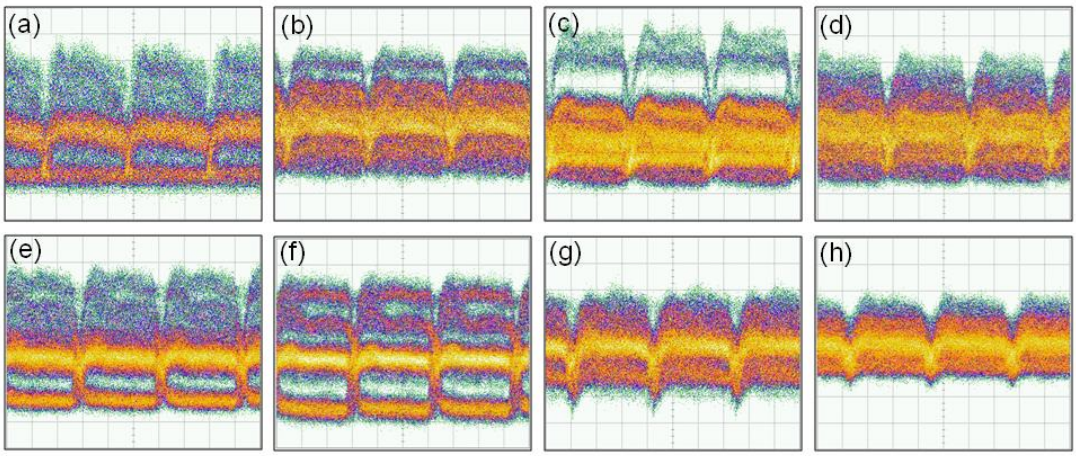

Figure 3.12: Intensity patterns of 625 Mbaud 16-QAM behind DPMZM. (a) $\alpha = 0.5, \Delta = 0.5$; (b) $\alpha = 0.5, \Delta = 1$; (c) $\alpha = 0.5, \Delta = 0.35$; (d) $\alpha = 0.5, \Delta = 0.7$; (e) $\alpha = 0.7, \Delta = 0.5$; (f) $\alpha = 0.7, \Delta = 1$; (g) $\alpha = 0.35, \Delta = 1$ and (h) $\alpha = 0.35, \Delta = 0.5$.

Figure 3.13 shows the received constellation maps after optical transmission over 1.6 km of SMF for -20 dBm preamplifier input power for different α and Δ values [49]. Using the parameters $\alpha = 0.5$ and $\Delta = 0.5$, the constellation is aligned properly as shown in Figure 3.13(a), and this gives the best BER. As Δ is increased to 1, the constellation shows severe phase distortions as shown Figure 3.13(b). In Figure 3.13(c-h), the amplitude and the phase deviate from the values needed for ideal constellation.

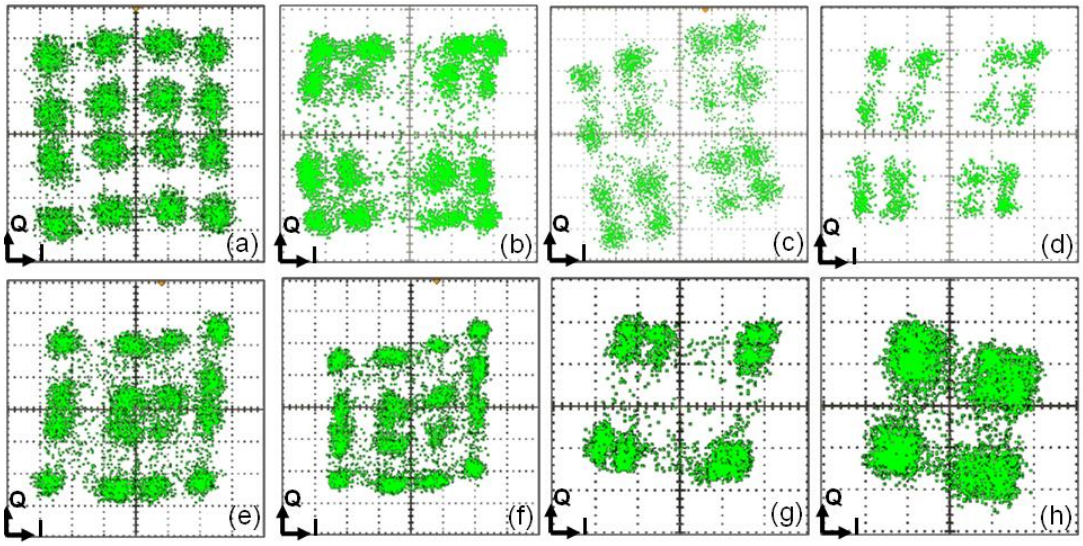

Figure 3.13: 16-QAM constellation after optical transmission for –20 dBm. (a) $\alpha = 0.5, \Delta = 0.5$; (b) $\alpha = 0.5, \Delta = 1$; (c) $\alpha = 0.5, \Delta = 0.35$; (d) $\alpha = 0.5, \Delta = 0.7$; (e) $\alpha = 0.7$; $\Delta = 0.5$; (f) $\alpha = 0.7, \Delta = 1$; (g) $\alpha = 0.35, \Delta = 1$ and (h) $\alpha = 0.35, \Delta = 0.5$.

Figure 3.14 shows the Q-factor dependence from the parameter α for different launched and received fiber preamplifier input power. For MZMs with ER of 25 dB and 50 dB, the transmission performance of Q-factor at each α is plotted while the parameter Δ varied in each curve. Equation (3.11) shows how we can obtain the Q-factor from the BER, where the Q factor increases as BER improves.

$$\text{BER} = \frac{1}{2} erfc\left(\frac{Q}{\sqrt{2}}\right). \tag{3.11}$$

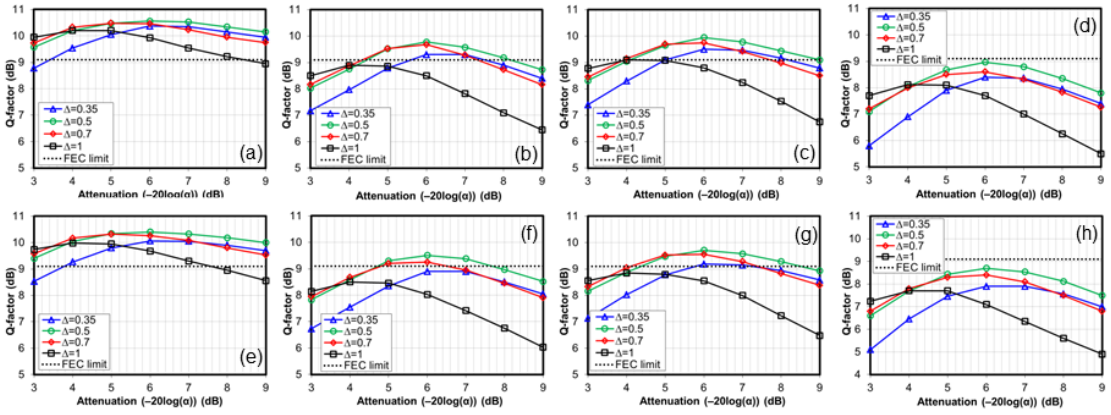

Figure 3.14: Q-factor dependence with the variation of the parameter α for: (a) ER = 50dB, TX– 5dBm, RX– 20dBm; (b) ER = 50dB, TX – 5dBm, RX– 30dBm; (c) ER = 50dB, TX – 9dBm, RX– 20dBm; (d) ER = 50dB, TX – 9dBm, RX– 30dBm; (e) ER = 25dB, TX – 5dBm, RX– 20dBm; (f) ER = 25dB, TX – 5dBm, RX– 30dBm; (g) ER = 25dB, TX – 9dBm, RX– 20dBm; (h) ER = 25dB, TX – 9dBm, RX– 30dBm.

Chapter 4:

16-QAM receiver design

4.1 Coherent receiver

Figure 4.1 shows the subsystems of a synchronous digital coherent receiver. The functionality of the first three subsystems is to produce the synchronized channel, and the next sections will focus on it.

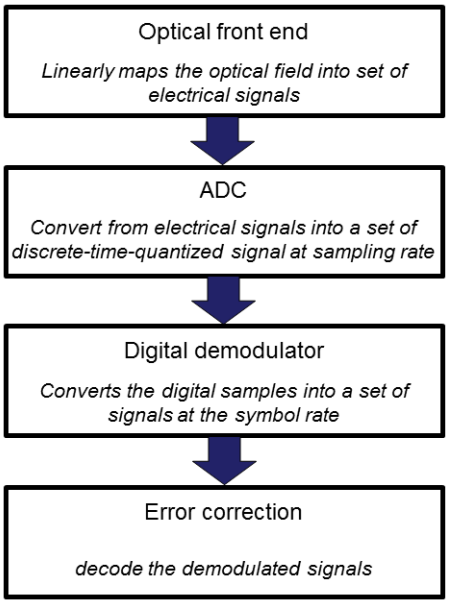

Figure 4.1: Key subsystems of digital coherent receiver.

4.1.1 Distinguishing of coherent detection

Two fundamental kinds of receivers with coherent (heterodyne and homodyne) detection can be distinguished. These two schemes were intensively studied in the 1980s [55–57] and prior to the advent of the erbium-doped fiber amplifier in the early 1990s because of their excellence to direct detection, especially in terms of sensitivity and frequency selectivity. As illustrated in Figure 4.2, the carrier frequencies of signal laser and LO laser can be identical or different. If they are identical, then there will be coherent homodyne detection where the optical spectrum will be directly converted to the electrical baseband. In the second case, coherent heterodyne detection, the field information of the optical

signal wave is transferred onto an electrical carrier at an intermediate frequency (IF) given by $w_{IF} = |w_s - w_{lo}|$. If the carrier frequencies of the optical signals are different by a fraction of the symbol rate (R_s), the intermediate frequency will be placed somewhere within the signal band, this case is named by coherent intradyne detection [3].

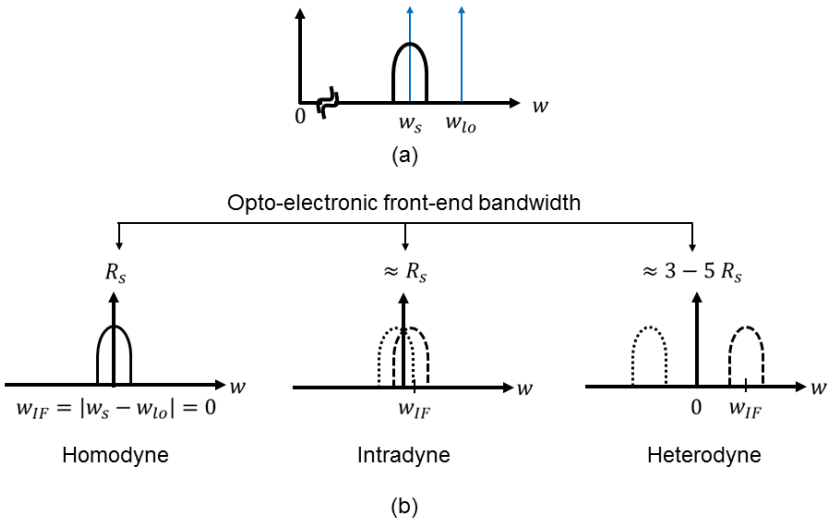

Figure 4.2: Optical signal spectra (a) and coherent detection options (b).

4.1.2 Receiver effort

The suitability and feasibility of a practical receiver scheme must be chosen according to the received modulation format. IQ receivers for direct detection which are identical for all higher-order phase modulation formats, have simple optical complexity because carrier synchronization is not necessary. The general coherent detection shows higher optical frontend complexity because a LO is required. Furthermore, to implement a coherent receiver one needs to control frequency and polarization of the signal. In case of differential detection, carrier phase synchronization is not important because differential demodulation is needed to implement on the electrical side, so laser phase noise is not so important. When performing synchronous detection for high-order modulation format, carrier phase synchronization becomes necessary and a challenge for practical implementation. Furthermore, progress in digital signal processing technology allows to implement carrier synchronization digitally. Direct detection shows less complexity in electrical data recovery comparing to coherent detection. Despite of their higher complexity, coherent receivers have the advantage to translate the electrical field of optical signal into electrical domain, this makes coherent receiver more sensitive to carrier phase and state of polarization (SOP) of the incoming signal. In addition, all transmission

impairments can be mitigated in electronic domain. All these things above make coherent synchronous detection more suitable for arbitrary modulation formats.

4.2 Coherent optical to electrical converter

Phase-diversity receivers are based on optical hybrids, which combine the fields of the received modulated signal and the LO, introducing various phase shifts between the two, followed by multiple identical p-i-n photodiodes to detect the combined optical signal [39]. As the receiver uses two photodiodes in each branch, it is called a balanced receiver. The phase-diversity receiver with a 90º hybrid is shown in Figure 4.3(left). In high-order modulation, 2×4 90º optical hybrids are used to separately recover the in-phase and quadrature components of an optical signal. The viability and different possibilities to implement the 2×4 90º hybrid are discussed in [58]. One option to implement the 2×4 90º hybrid is by using four 3 dB couplers and a $\pi/2$ phase shift in one branch.

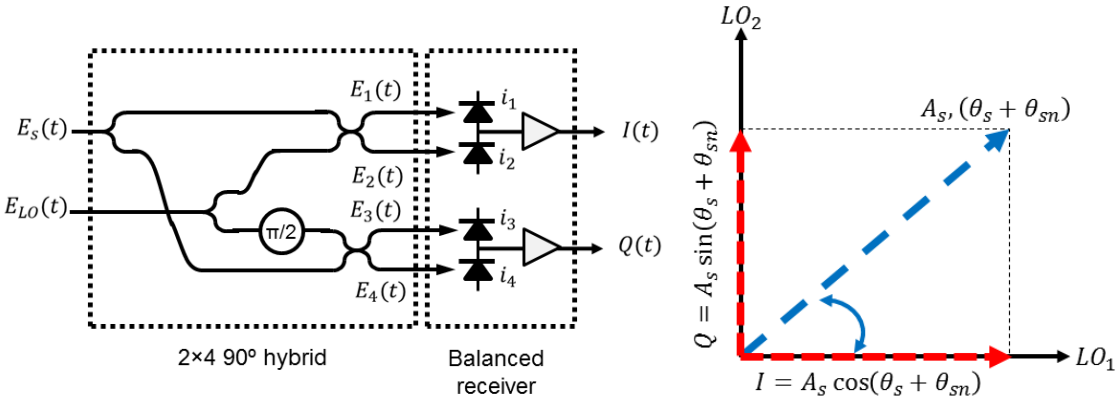

Figure 4.3: Configuration of optical down converter with optical to electrical convertor (left) and phasor diagram of the signal and LO for phase-diversity homodyne detection (right).

An integrated form is fabricated in $LiNbO_3$ to achieve IQ balance [59]. The device became available commercially with six adjustable electrodes [60]. Four independent electrodes (IC1, IC2, OC1, OC2) to control power difference of the 3 dB couplers and two electrodes to set the phase difference between upper and lower branches (PS1, PS2) [61], as shown in Figure 4.4.

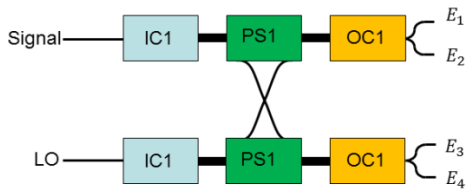

Figure 4.4: 90º hybrid with six adjustable electrodes.

Assuming that the normalized electrical field of the optical signal at the received side of the 90º hybrid is

$$E_s = \sqrt{P_s} \cdot e^{j(w_s t+\varphi_s)} \cdot a(t) \cdot e^{j\varphi(t)} \cdot e^{j\varphi_{ns}(t)} \cdot e_s \tag{4.1}$$

and the continuous wave light of the LO is

$$E_{lo} = \sqrt{P_{lo}} \cdot e^{j(w_{lo} t+\varphi_{lo})} \cdot e^{j\varphi_{nlo}(t)} \cdot e_{lo} \tag{4.2}$$

where P_s and P_{lo} are the continuous wave powers, w_s and w_{lo} are signal laser and LO angular frequencies, respectively. φ_s and φ_{lo} are the initial phases, $\varphi_{ns}(t)$ and $\varphi_{nlo}(t)$ represent the laser phase noise, $a(t)$ is the normalized modulation amplitude, $\varphi(t)$ is the modulation phase, and e_s and e_{lo} are the polarization unit vectors of signal and LO light [43]. The polarizations of the received signal and LO laser are assumed to be the same ($e_s = e_{lo}$). The received analytical electrical field from the two inputs E_s and E_{lo} is E_l, where l is the number of each output

$$\begin{aligned} E_1 &= \tfrac{1}{2}(E_s + E_{lo}), \\ E_2 &= \tfrac{1}{2}(E_s - E_{lo}), \\ E_3 &= \tfrac{1}{2}(E_s + jE_{lo}), \\ E_4 &= \tfrac{1}{2}(E_s - jE_{lo}). \end{aligned} \tag{4.3}$$

These four output fields illuminate two pairs of two identical p-i-n photodiodes, and the photocurrents are

$$i_l = R_l \cdot E_l \cdot E_l^{\,*} + n_{sh} \tag{4.4}$$

where R_l represents the responsivity of the photodiodes [44], and asterisk denotes the adjoint matrix. n_{sh} represent the shot-noise photocurrents of the photodiodes.

$$R = \eta \frac{2\pi e}{h w_s} \tag{4.5}$$

where $e = 1.6 \cdot 10^{-19} C$ is the charge per electron, $hw_s/2\pi$ is the energy per photon with Planck's constant $h = 6.63 \cdot 10^{-34} Js$, η is the quantum efficiency of the photo diode. In case of $R_1 = R_2 = R_3 = R_4$, the outputs of the photodiodes within the balanced detectors are then subtracted, resulting in a combined in-phase and a quadrature photocurrent:

$$I(t) = i_2 - i_1 = R\sqrt{P_s P_{lo}}\, a(t)\, e_s e_{lo} \cos[\Delta w t + \varphi_n(t) + \varphi_0 + \varphi(t)] + n_I \quad (4.6)$$

and

$$Q(t) = i_3 - i_4 = R\sqrt{P_s P_{lo}}\, a(t)\, e_s e_{lo} \sin[\Delta w t + \varphi_n(t) + \varphi_0 + \varphi(t)] + n_Q \quad (4.7)$$

where Δw is the angular frequency offset between signal laser with w_s and LO with w_{lo}. A fixed phase offset φ_0 will appear because of the difference between the initial phases of signal and LO ($\varphi_0 = \varphi_s - \varphi_{lo}$). The overall laser phase noise which is defined as ($\varphi_n(t) = \varphi_{ns}(t) - \varphi_{nlo}(t)$) and will lead to a random walk of the phase which causes a rotation of the received constellation diagram. n_I and n_Q represent some additive noise in each branch. If the receiver is shot-noise limited then n_I and n_Q will represent the overall shot-noise photocurrents of the two balanced photodetectors, and can be substituted by n_{shI} and n_{shQ}, respectively. If the optical amplifier in the system is limited to LO-ASE noise, then the two parameters will be explained as n_{I_ASE} and n_{Q_ASE}. This noise is Gaussian for the case of neglecting the LO laser phase noise. In coherent detection the LO-ASE noise is dominant to other noise components like signal-ASE noise and ASE-ASE noise [43]; as for direct detection systems the signal-ASE noise is dominant because it depends on the power of the detected symbols. The influence of thermal noise of the receiver can be neglected if the LO power is somehow high and the system becomes a shot-noise limited receiver [43]. For long-haul optical transmission the influence of shot-noise can be neglected because the receiver is limited by amplifier noise. Moreover, the polarizations of signal laser and LO should be aligned exactly to obtain maximum interference. Using two polarizations provide an auxiliary degree of freedom for optical transmission systems and double the spectral efficiency of the modulated signal. One can determine the complex amplitude ($X(t)$) using in-phase and quadrature photocurrents which is the same as the complex amplitude of the optical information signal except for the phase noise. Also it shows that the signal is down-converted into the baseband. $A(t)$ in equation (4.8) represent the normalized complex modulation envelope ($A(t) = a(t) \cdot e^{j\varphi(t)}$), and $n_{IQ}$is the complex shot-noise ($n_{IQ} = n_I + jn_Q$).

$$\mathrm{X}(t) = I(t) + jQ(t) = R\sqrt{P_s P_{lo}}\, A(t)\, e_s e_{lo} e^{j(\Delta w t + \varphi_n(t) + \varphi_0 + \varphi(t))} + n_{IQ} \quad (4.8)$$

4.3 Receiver with polarization and phase diversity

It has been assumed up to here that the SOPs of the incoming signal and LO were identical. However, in real systems, the SOP of the incoming signal is unlikely to remain aligned to

the SOP of LO because of fluctuations of transmission fiber birefringence. The output signals from balanced photodetectors depend on the SOP of the incoming signal and LO light. Polarization diversity should be used to avoid outages; it contains two polarization beam splitters (PBS) and two phase diversity receivers as shown in Figure 4.5. The optical information signal has an arbitrary SOP and is separated into a couple of liner polarization with PBS. Two 90º hybrids are used to generate eight electric fields for balanced photodiodes. Receivers employing polarization diversity have been extensively investigated in [62, 63].

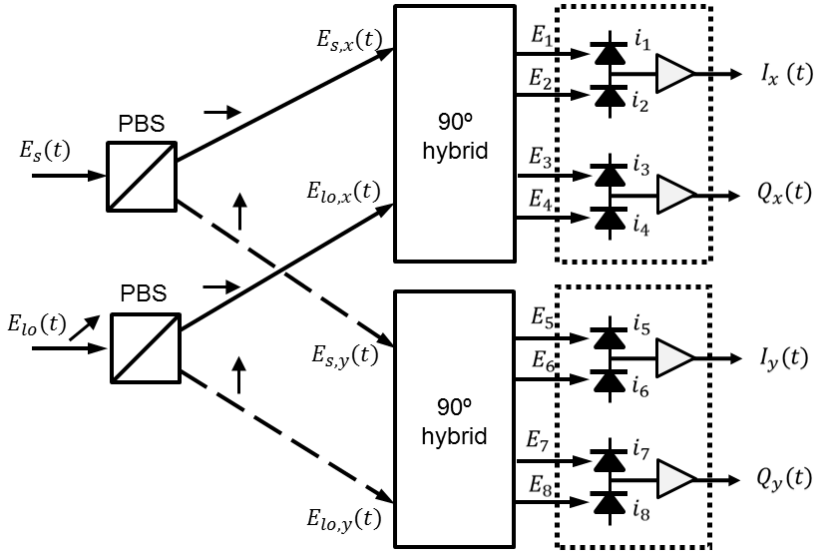

Figure 4.5: Configuration of a polarization diversity receiver.

The final expression of the photocurrents in the upper and lower branch, in the absence of noise, are given by

$$I_x(t) = R\sqrt{P_{s,x}P_{lo}/2}\, a(t)\cos[\Delta wt + \varphi_n(t) + \varphi_0 + \varphi(t) + \varphi_x] \tag{4.9}$$

$$Q_x(t) = R\sqrt{P_{s,x}P_{lo}/2}\, a(t)\sin[\Delta wt + \varphi_n(t) + \varphi_0 + \varphi(t) + \varphi_x] \tag{4.10}$$

$$I_y(t) = R\sqrt{P_{s,y}P_{lo}/2}\, a(t)\cos\left[\Delta wt + \varphi_n(t) + \varphi_0 + \varphi(t) + \varphi_y\right] \tag{4.11}$$

$$Q_y(t) = R\sqrt{P_{s,y}P_{lo}/2}\, a(t)\sin\left[\Delta wt + \varphi_n(t) + \varphi_0 + \varphi(t) + \varphi_y\right] \tag{4.12}$$

where $P_{s,x}$ and $P_{s,y}$ are the power of the optical signal in the *x*- and *y*-polarization, respectively. φ_x and φ_y are the phase noise emerging from the polarization mismatch between the signal and local oscillator in the upper and lower branch, respectively.

4.4 Signal-to-noise ratio of a modulated signal

The performance of telecommunication systems depend on the SNR associated with the demodulated signal and the so called carrier-to-noise ratio (CNR). The CNR is defined as the RMS power of the received modulated carrier signal to the RMS received noise power after the receive filters.

$$CNR = \frac{average\ signal\ power}{noise\ power} \tag{4.13}$$

The complex phasor describes the received amplitude and phase in IQ-plane given by equation (4.8). The total noise output from each double balanced photodiodes mainly consist of three sources: (i) LO shot noise n_{sh}, (ii) amplified spontaneous emission (ASE) LO beta noise n_{ASE}, and (iii) circuit noise n_c [64]:

$$\overline{n_I{}^2} = \overline{n_Q{}^2} = \overline{n_{sh}{}^2} + \overline{n_{ASE}{}^2} + \overline{n_c{}^2} \tag{4.14}$$

where the LO shot noise variance is given by

$$\overline{n_{sh}{}^2} = 2eR\frac{P_{lo}}{2}\frac{\Delta f}{2}. \tag{4.15}$$

In this equation, $\Delta f/2$ represents the noise bandwidth and Δf is the receiver bandwidth, where the LO power is divided by two by the phase diversity process. The ASE-LO beat noise variance is given by

$$\overline{n_{ASE}{}^2} = 4eR\frac{\eta(G-1)n_{sp}}{2}\frac{P_{lo}}{2}\frac{\Delta f}{2}, \tag{4.16}$$

where G is optical amplifier gain and n_{sp} denotes the amplifier spontaneous emission factor. The circuit noise variance is given by

$$\overline{n_c{}^2} = 4\frac{k_B T_{abs}}{r_{in}}\frac{\Delta f}{2}, \tag{4.17}$$

where k_B is the *Boltzmann constant*, T_{abs} is the absolute temperature, and r_{in} is the input load resistor.

The total noise appearing in n_{IQ} is

$$\overline{n_{IQ}{}^2} = \overline{n_I{}^2} + \overline{n_Q{}^2} = 2\left(\overline{n_{sh}{}^2} + \overline{n_{ASE}{}^2} + \overline{n_c{}^2}\right) \quad (4.18)$$

When the LO shot noise dominates the circuit noise with sufficient LO power, there is no need to rely on the optical preamplifier (i.e. Letting preamplifier gain $G = 1$ and $P_{lo} \to \infty$). The mean square of the signal photocurrent for heterodyne receivers is $\overline{|\mathrm{X}(t)|^2} = 4R^2P_sP_{lo}$ and for homodyne receivers is $\overline{|\mathrm{X}(t)|^2} = R^2P_sP_{lo}$. The receiver bandwidth at the baseband is $\frac{\Delta f}{2} = \frac{1}{2T}$ for homodyne signal and at the intermediate frequency $\Delta f = \frac{1}{2T}$ for heterodyne signal (i.e. minimum bandwidth); T is symbol duration [3].

The shot-noise limited CNR of the heterodyne signal becomes

$$CNR_{heterodyne} = \frac{\overline{|\mathrm{X}(t)|^2}/2}{2eRP_{lo}\Delta f} = \frac{\eta P_s}{h\Delta f}. \quad (4.19)$$

In case of homodyne when reconstructing the complex amplitude, shot noise due to LO power of $P_{lo}/2$ has to be added because of homodyne receivers from both ports. The CNR of the homodyne signal is given as

$$CNR_{homodyne} = \frac{\overline{|\mathrm{X}(t)|^2}}{eRP_{lo}\Delta f} = \frac{\eta P_s}{h\Delta f}, \quad (4.20)$$

which is the same as heterodyne receiver, even when two polarizations are introduced [3].

4.5 Digital processing in coherent detection

The recent advances in high-speed digital signal processing to optical coherent detection makes more phase estimation options available, compared to earlier generation where Phase-locked loops (PLLs) were always deployed [65]. After O/E conversion, the analog signals are converted to digital signals using ADCs [14] [66] [67]. The outputs from ADCs are processed by a digital signal processing unit (DSPU), resulting in the complex amplitude of the signal in a stable manner in spite of a permanently changing carrier phase and signal polarization. The digital signal processing structure is typically composed of a sequence of operations to recover the information of the received signal as shown in Figure 4.6. The subsystems give some indication to the design of digital coherent receiver. Furthermore, recent progress in high performance, speed, and reliability of integrated circuits make digital signal processing technology attractive to recover the complex amplitude from the received baseband signal.

ADCs and DSPU will be integrated within a single chip to ease the interface, reduce footprint size and energy consumption. FPGAs can be employed to verify and evaluate

DSP algorithms in real-time experiments, but they are insufficient for commercial implementation in terms of available performance and energy efficiency.

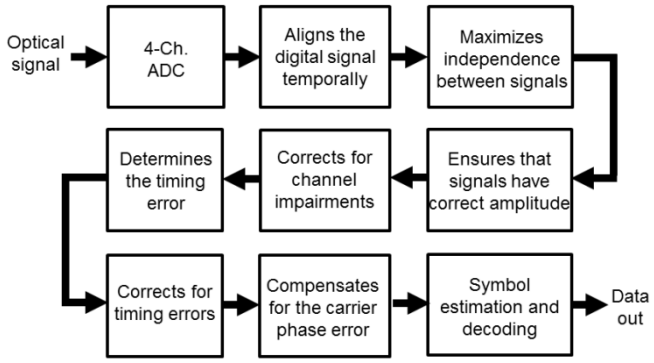

Figure 4.6: Typical functional sequence of digital coherent receiver.

4.5.1 Digital coherent receiver

Figure 4.7 shows a simplified block diagram of an optical transmission system with coherent detection and polarization multiplex. The intradyne receiver signal is generated by an unmodulated LO laser and two 90° hybrids for the optical demodulation and separation. The DSPU contains several subsystems to overcome static and dynamic channel impairments as well as laser phase noise and inadequate receiver setups in the digital domain [68]. Digital coherent receiver techniques can compensate for linear distortions such as CD and PMD [69], as well as nonlinear distortions such as SPM [70]. The concept of linear optical communication systems become very clear in Figure 4.7, where a vector in the complex plane drives the quadrature modulator with two electric fields.

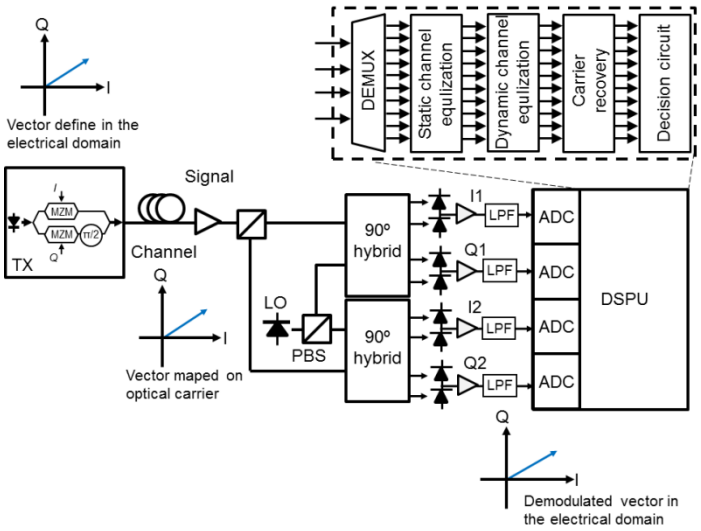

Figure 4.7: Simplified block diagram of an optical transmission system with coherent detection and digital signal processing

The complex envelope of the modulated electric field at the output of the quadrature modulator is mapped on the phasor of the optical carrier. This vector is perfectly restored by the digital coherent receiver. This combination of optical transmitter and optical receiver is a linear optical transmission system, where complex envelope is protected even with E/O and O/E conversion process.

At the receiver end, the signal is passed through a linear homodyne synchronous detection polarization diversity receiver. After phase and polarization diversity optical circuit, the entire of optical field (i.e. amplitude, frequency, phase and polarization) can be obtained. After photodetection, in-phase and quadrature parts of the electric fields are low-pass filtered and fed into the ADCs. The ADCs asynchronously sample the in-phase and quadrature signals with a frequency equal or greater than twice the symbol rate. The amplitude of the output signal will pass through a quantizer which will take $2^{\text{ADC resolution bits}}$ discrete values to restore the complex amplitudes [31]. Such complex amplitudes are equalized in the time or frequency domain by equalizers which compensate for the main part of CD having been accumulated along the fiber channel [43]. Carrier recovery is used to compensate for the distortion by laser phase noise, frequency offset and initial phase offset; it will also rotate the constellation diagram to a suitable position by correcting the received phase. After CD equalization and clock recovery, PMD can be compensated within separating both polarizations. Frequency and phase estimations are performed on both channels before the received symbols are finally decoded. High baud rates of optical transmission links require *M*-fold parallelization of the digital signal processing to meet technology parameters. This results in several constraints for algorithm structure and computational complexity [71].

The following paragraphs skip timing recovery and equalization, but in detail describe carrier synchronization by digital phase estimation for the single polarization receiver depicted in Figure 4.7. Here, a single polarization is used with an ideal clock recovery. The in-phase and quadrature signals at the output of optical quadrature photodetection, defined by equations (4.6) and (4.7), are sampled by an ADC once per symbol at the sampling instant t_k which is located in the middle of the symbols [43].

Electrical filters have been neglected, the in-phase and quadrature samples (I_k & Q_k) at the *k*-th symbol interval are

$$I_k = R\sqrt{P_s P_{lo}}\, a_k \cos[\Delta w t_k + \varphi_{nk} + \varphi_0 + \varphi_k] + n_{I_k} \tag{4.21}$$

and

$$Q_k = R\sqrt{P_s P_{lo}}\, a_k \, \sin[\Delta w t_k + \varphi_{nk} + \varphi_0 + \varphi_k] + n_{Q_k} \tag{4.22}$$

where a_k, φ_k and φ_{nk} represent the samples of the modulation amplitude, the modulation phase, and the overall laser phase noise respectively. The vector on the complex plane after sampling is given by

$$X_k = I_k + jQ_k = R\sqrt{P_s P_{lo}} \cdot A_k \cdot e^{j\Phi_k} + n_{IQ_k} \tag{4.23}$$

where the samples of the normalized complex envelop A_k, the phase error Φ_k, and the complex noise n_{IQ_k} are defined as

$$A_k = a_k \cdot e^{\varphi_k}, \quad \Phi_k = \Delta w t_k + \varphi_{nk} + \varphi_0, \quad n_{IQ_k} = n_{I_k} + n_{Q_k}. \tag{4.24}$$

4.5.2 Carrier recovery classes and categories

Carrier phase estimation is a key challenge in coherent transmission systems in order to optimize the laser linewidth tolerance. A large number of frequency and phase recovery algorithms have been proposed in the previous years [72, 28, 73, 74] to estimate the phase error Φ_k from the received signal. The goal of these algorithms is to compensate for the complex noise impairment. Carrier recovery can be classified into three main classes: (i) data-assisted (DA), (ii) decision-directed (DD) and (iii) non-decision-aided (NDA). DA carrier recovery methods require training sequences, so the effective link capacity will be reduced. In order to avoid lowering the capacity blind carrier recovery methods must be employed. Although Ip analyzed in [75] that DD carrier recovery methods are optimal for high SNR compared to NDA methods, [65] proved that they are not feasible in a practical systems with parallel signal processing because of the internal delay in the feed-back loop. Alternatively, a NDA algorithm can be designed as a pure feed-forward approach, and it has just a marginal worse performance than the maximum a posteriori phase estimator which was found out to be the optimal solution in coherent optical communication system [65]. Nowadays NDA phase error estimators are state-of-the art in coherent optical systems.

In addition to the aforementioned classes one can further broadly categorize the phase and frequency synchronization techniques according to the receiver concepts into: (i) Closed-loop (or decision feedback) and (ii) Open-loop (or feed-forward) schemes, such as Viterbi-&- Viterbi or M^4 techniques. Decision feedback technique involves a feedback path within the system to make corrections for errors. The basic design of such a system is illustrated

by using PLL. In contrast to decision feedback, feed-forward schemes do not contain a feedback path. Closed-loop synchronization has a very diverse history at the eighties and the beginning of nineties [43]. Today's, open-loop estimation has a rich literature as well, also has only more recently been applied to the task of carrier recovery. Digital coherent receivers also allow new techniques for phase and frequency synchronization. PLLs are no longer required for optical receivers as frequency mismatch between the transmitter and the LO laser only results in a constant rotation of the received constellation. Recent investigations have shown that feed-forward carrier synchronization techniques are more tolerant to laser phase noise than PLL based receivers.

4.5.3 Feed-forward square 16-QAM carrier phase estimation schemes

Even the unmodulated IF signal contains a phase noise corresponding to the sum linewidth of TX and LO lasers. If there is no automatic LO frequency control then the IF generally will differ from zero. A non-zero IF leads to a deterministic phase slope on adjacent samples which can be employed for frequency estimation [76]. The random phase noise has to be tracked by a phase estimation stage that also removes residual frequency offsets due to imperfect frequency estimation or LO frequency control. The effort for phase estimation (calculation of a time series of angles, real numbers within a limited range) depends on the modulation format.

For star constellations (BPSK, QPSK, 8-PSK and certain QAM formats) it is obviously advantageous to convert the received symbols to polar coordinates and demodulate them by a simple subtraction of signal and carrier phase angles [77]. In contrast, higher-order square QAM formats require a rotation in the complex plane for demodulation to adjust them to non-radial decision boundaries. While for M-PSK modulation CPE can efficiently be performed by using, e.g., the Viterbi and Viterbi phase estimation (VVPE) method [78] or the multiplier-free estimator proposed in [79]. Square QAM modulated systems require an increased DSP complexity because only a small set of the symbols have equidistant phases ($\theta 1 \neq \theta 2$), cf. Figure 4.10. To recover the carrier phase with a sufficient tolerance against phase noise, information of all received symbols should be used for CPE. The feed-forward phase noise estimation technique uses N successive samples of X_k to produce an estimate of the average phase noise during the N symbol interval.

$$X_k = Z_k \cdot e^{j\Phi_k} + n_{c_k} \tag{4.25}$$

$$Z_k = R\sqrt{P_s P_{lo}} \cdot A_k \tag{4.26}$$

where Z_k is the amplitude value at the *k*th symbol, and n_{c_k} is the additive white Gaussian noise (AWGN) with zero mean and variance $\delta^2/2$ per dimension.

Phase noise is a Wiener process [80] as follows:

$$\Phi_k = \sum_{i=0}^{k} v_i \tag{4.27}$$

where the $v_i(s)$ are independent and identically distributed (i.i.d.) random Gaussian variables with zero mean and a variance of

$$\sigma_v^2 = 2\pi(\Delta f \cdot T_s) \tag{4.28}$$

where $(\Delta f \cdot T_s)$ is the laser-sum-linewidth-times-symbol-interval-product. Carrier recovery techniques first estimate the value of Φ_k and then remove it from equation (4.25).

In this work two efficient NDA carrier phase estimation methods [73, 28] have been tested in a real-time transmission experiment and compared with each other. Feed-forward phase estimators (PE) using the QPSKP scheme [81, 73], require less computational effort in comparison to minimum distance PE concepts [82, 83], but they are more sensitive against noise effects, especially for higher order QAM constellations due to the laser linewidth tolerance and limited computational resources. The algorithms are described in the following subsections.

4.5.3.1 Blind phase search (BPS) technique

This subchapter showed Pfaus's results for carrier recovery. Recently, T. Pfau et al., introduced the BPS technique (or minimum distance method) which was firstly proposed for more general synchronous communication systems in [84] and [85] to optical coherent systems [28]. The developed BPS estimator features good tolerance to laser linewidth, blind feed-forward manner, and universally to arbitrary M-QAM format. For 16-QAM, the estimator simultaneously tries a fixed set of different carrier phase angles and determines the most likely one of them [28]. Figure 4.8 shows a block diagram of the employed carrier recovery module. The input signal Z_k of the coherent receiver is sampled at the symbol rate. For the theoretical description, perfect clock recovery and equalization are assumed [28]. The phase estimator rotates the received symbols Z_k into the first quadrant. Then they

are rotated within the quadrant in parallel by B test carrier phase angles φ_b which are equally spaced:

$$\varphi_b = \frac{\mathrm{b}}{B} \cdot \frac{\pi}{2},\ b \in \{0,1,\dots,B-1\} \tag{4.29}$$

Afterwards, all rotated symbols are fed into a decision circuit and the squared distance $\left|d_{k,b}\right|^2$ to the closest constellation point is calculated in the complex plane:

$$\begin{aligned} \left|d_{k,b}\right|^2 &= \left|Z_k e^{j\varphi_b} - \left\lfloor Z_k e^{j\varphi_b} \right\rfloor_D\right|^2 \\ &= \left|Z_k e^{j\varphi_b} - \hat{X}_{k,b}\right|^2 \end{aligned} \tag{4.30}$$

In order to reduce the influence of channel noise distortions, the distances of $2N+1$ consecutive symbols rotated by the same carrier phase angle φ_b are summed up to a mean square error quantity $S_{k,b}$:

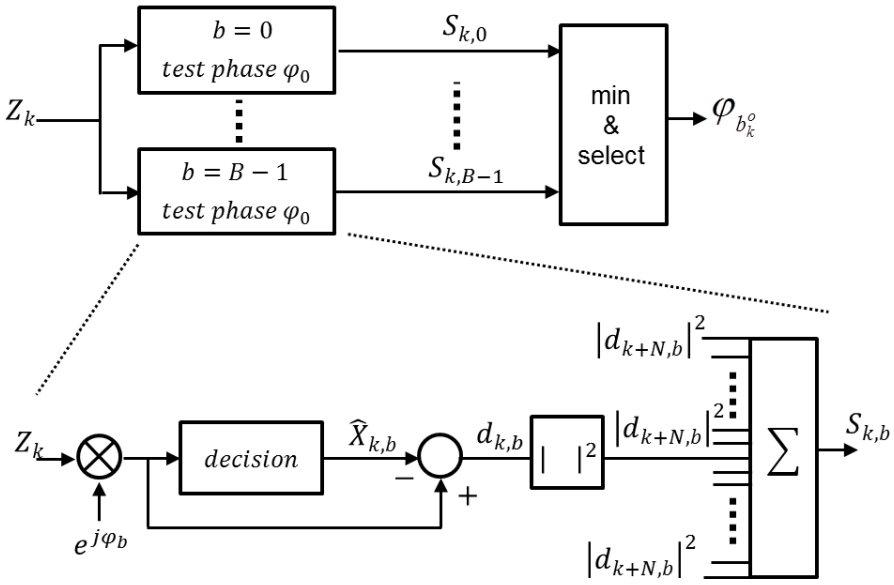

Figure 4.8: BPS Feed-forward carrier recovery [28].

$$S_{k,b} = \sum_{n=-N}^{N} \left|d_{k-n,b}\right|^2 \tag{4.31}$$

The optimum value of the filter half width N depends on the product of the laser linewidth multiplied by the symbol rate. A value of $N = 6,\dots,10$ turned out to be a fairly good choice in simulation [28]. After filtering, the optimum phase angle is determined by searching the minimum sum of distance values. As the decoding was already executed in

equation (4.30), the decoded output symbol $\hat{X}_k$ can be selected from the $\hat{X}_{k,b}$ by a switch controlled by the index $m_{k,min}$ of the minimum distance sum.

Due to the 4-fold ambiguity of the recovered phase in the square M-QAM constellation the first two bits which determine the quadrant of the complex plane should be differentially Gray-encoded. The differential encoding and decoding process is the same as for QPSK and is presented in detail in [86]. It can be described by the following formula

$$n_{o,k} = (n_{r,k} - n_{r,k-1} + n_{j,k}) mod 4$$
$$n_{o,k}, n_{r,k}, n_{j,k} \in \{0,1,2,3\} \quad (4.32)$$

where $n_{o,k}$ is the differentially decoded quadrant number, $n_{r,k}$ is the received quadrant number and $n_{j,k}$ is the jump number. The only required modification of the decoding process compared to [86] is that quadrant jumps are detected according to the following formula:

$$n_{j,k} = \begin{cases} 1 & if\ m_{k,min} - m_{k-1,min} > M/2 \\ 3 & if\ m_{k,min} - m_{k-1,min} > -M/2 \\ 0 & otherwise \end{cases} \quad (4.33)$$

For all other bits that determine the symbol within the quadrant of the complex plane, normal Gray-coding is sufficient and no differential encoding/decoding is required. Figure 4.9 illustrates the bit to symbol assignment including differential encoding/decoding for square 16-QAM. The resulting constellation diagram is not any longer Gray-encoded. This multiplies the BER by a factor of 2 for 4-QAM (QPSK), 1.67 for 16-QAM, and less (approaching 1) for high order QAM constellations [87].

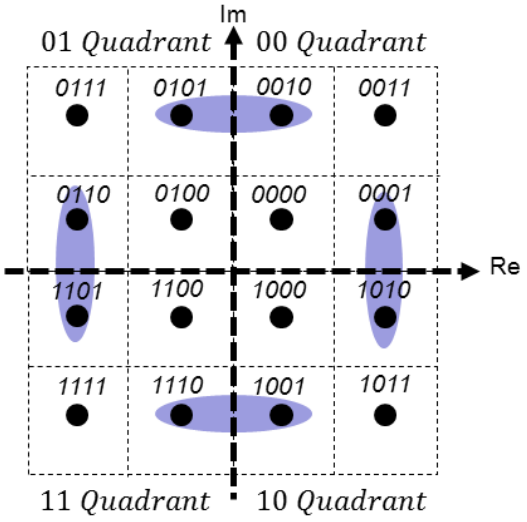

Figure 4.9: Partial differential encoding for a square 16-QAM constellation [28].

4.5.3.1.1 Hardware efficient carrier recovery implementation

The rotation of a symbol in the complex plane normally requires a complex multiplication, consisting of four real-valued multiplications with subsequent summations. This leads to a large number of multiplications to be executed. The hardware effort would therefore become prohibitive, especially for higher order constellations. Applying the CORDIC (coordinate rotation digital computer) algorithm [88] can dramatically reduce the necessary hardware effort to calculate the B rotated test symbols. This algorithm can compute vector rotations simply by summation and shift operations. As for the calculation of the B rotated copies of the input vector intermediate results can be reused for different rotation angles, the number of shift and add operations required to generate the B test symbols is given by

$$n_{op} = \sum_{b=1}^{\log_2 B} 2^{b+1} \tag{4.34}$$

For $= 16$, the CORDIC algorithm requires only 60 shift and add operations whereas complex multiplication of Z_k with 16 test phasors would require 64 real multipliers and 32 adders. To determine the closest constellation point $\hat{X}_{k,b}$ the rotated symbols are fed into a decision circuit. The square distance (4.30) can be written as

$$\begin{aligned} \left|d_{k,b}\right|^2 &= \left(\Re\left[d_{k,b}\right]\right)^2 + \left(\Im\left[d_{k,b}\right]\right)^2 \\ &= \left(\Re\left[Z_k e^{j\varphi_b}\right]\right)^2 - \left(\Re\left[\hat{X}_{k,b}\right]\right)^2 + \\ &\quad \left(\Im\left[Z_k e^{j\varphi_b}\right]\right)^2 - \left(\Im\left[\hat{X}_{k,b}\right]\right)^2 \end{aligned} \tag{4.35}$$

where $\Re[\cdot]$ and $\Im[\cdot]$ denote the real and the imaginary parts, respectively. Implementing this formula literally into hardware would lead to two multipliers and three adders, but a closer examination of (4.30) and (4.35) reveals that the results of the subtractions are relatively small because the distance to the closest constellation point is calculated. Therefore, the most significant bits (MSBs) of the subtraction result will always be zero and can be discarded to reduce the hardware effort. Due to the moderate resolution required for d^2, the squared distance (4.31) can be determined by a look-up table or basic logic functions more efficiently than by multipliers.

Parallel systems allow a very efficient implementation of the summation of $2N + 1$ consecutive values. The adders can be arranged in a binary tree structure where intermediate results from different modules are reused in neighboring modules leading to a moderate hardware effort.

In the experimental setup with the FPGA implementation used in [89, 90] and presented in Section 5.2.5, hardware effort is reduced by a suboptimal number of test carrier angles within the test interval, which reduces the precision of carrier recovery and thus receiver sensitivity. Using a two-stage carrier recovery is another possibility to reduce the hardware effort of the test interval. This is done by preprocessing the data in a first carrier recovery stage that provides a rough estimate of the carrier phase. The first estimator stage can be a standard fourth-power estimator or a simple decision directed estimator with feedback from the second stage [82]. Both first stage topologies allow reducing the size of the angular interval, and hence, the number of required test carrier phase angles B for the QAM feed-forward carrier recovery in the second stage. Feed-forward QAM phase estimation with multiple stages is also proposed by Zhou [83].

4.5.3.2 QPSKP technique

The constellation diagram for Square-16-QAM is shown in Figure 4.10. The symbols can be classified into three rings Class I, Class II and Class III according to their amplitudes. Class I and Class III symbols have equidistant phases, so the modulation can be removed by using a $(\cdot)^4$ operation. In contrast Class II symbols contain a modulation-dependent phase offset θ_1 that will not be removed by the 4th-power operation.

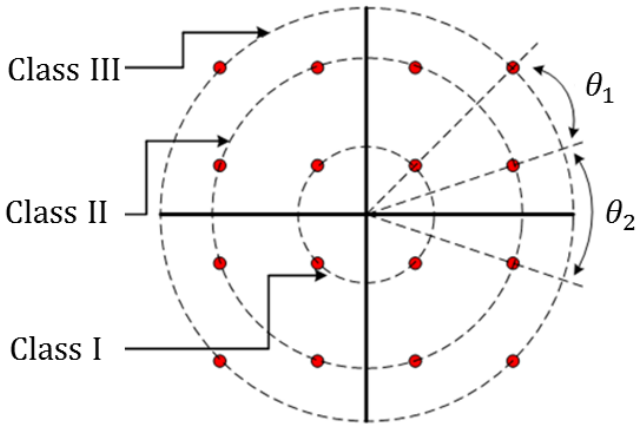

Figure 4.10: Square-16-QAM constellation.

To compensate for this offset a two stage CPE method has been proposed [91, 92, 73], shown in Figure 4.11. In the first stage the received symbols Z_k are classified by their amplitudes. Class II symbols are rotated by $\pm\theta_1$ to get rid of the modulation. In parallel a mean estimation of the residual symbols is done after the $(\cdot)^4$ operation. At the end of stage one the rotated Class II sample close to the mean estimate in the $(\cdot)^4$-domain is

selected. The aligned symbols $|\tilde{Z}_k|^4$ are passed to the second stage where a VVPE scheme is used to calculate the precise carrier phase angle $\hat{\varphi}_k$. Compared to pure VVPE designed for QPSK modulation the computational complexity is increased by the second filter stage, two complex multiplications for θ_1-compensation and one comparator to determine the right θ_1 rotation. The required classification of the received Class II symbols leads to an increased sensitivity against ASE noise and results to a larger filter half-width N.

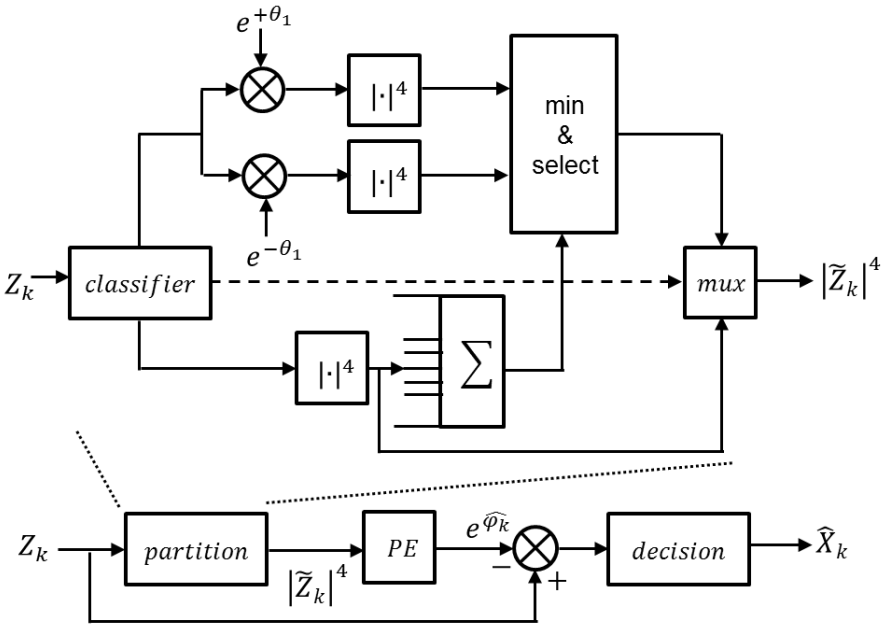

Figure 4.11: QPSKP Feed-forward carrier recovery.

4.6 Receiver implementation constrains

Real-time operation imposes constraints on coherent optical receivers [93]: (i) Elaborate digital signal processors cannot be clocked at the same multi-Gb/s rate as analog-to-digital converters. Time division demultiplexing is required and permits data processing, including synchronous carrier and data recovery, in M parallel modules at a lower clock frequency. (ii) Digital signal processing must be implemented efficiently in hardware because complicated algorithms boost chip area, power consumption and cost. The design should therefore not only be optimized by performance, but also by hardware aspects. (iii) Feedback delay can hardly be tolerated. Carrier recovery by decision-feedback is impossible at multi-Gbaud symbol rate. Feedback loops must therefore be avoided in the carrier recovery process, especially for 16- and higher-order QAM constellations where phase noise is very critical. Feed-forward design is the method of choice.

Chapter 5:

Real-time transmission system

This chapter presents the implemented 16-QAM transmission system with real-time synchronous demodulation and data recovery. Two efficient feed-forward carrier phase estimation methods [73, 28] have been tested in a real-time transmission experiments and compared with each other to present the performance against phase noise, sensitivity of the receiver phase angle resolution and the required receiver filter length. Also the influence of the required resolution of the ADCs, which is a challenge of real-time coherent transmission systems, is presented. The influence of linear and nonlinear effects related to the IQ-modulator of a 16-QAM coherent transmission system has been investigated in a real-time transmission. The VHDL code for the FPGA was developed in cooperation between Bielefeld University/CITEC and Paderborn University/ONT. CITEC developed the core program describing the carrier & data recovery according to the specifications provided by ONT.

5.1 Synchronous 16-QAM optical transmission setup

In July 2010 the worldwide first real-time synchronous optical 16-QAM transmission experimental results [94, 89] were presented for 1.25 Gb/s and 2.5 Gb/s 16-QAM modulated optical signal using standard external cavity laser (ECL), as shown in Figure 5.1.

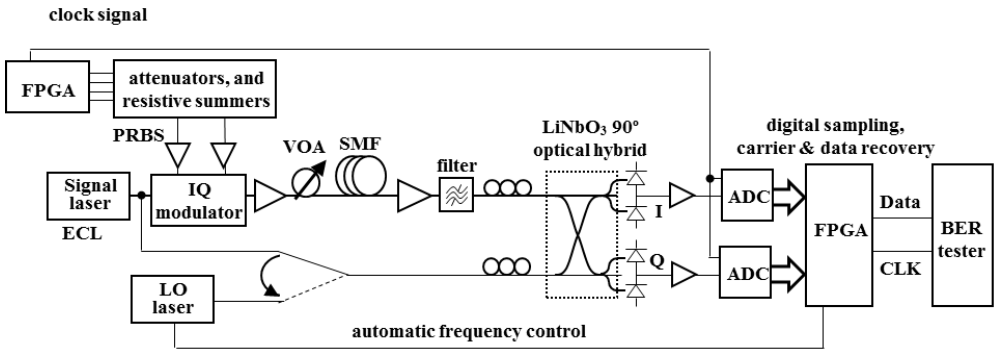

Figure 5.1: Worldwide first real-time synchronous 16-QAM transmission setup.

The results from these experiments showed that the implementation of a real-time digital coherent 16-QAM receiver was feasible and the error achieved was below the threshold of

a state-of-the-art FEC (7% overhead). All TX and RX signals were digitally processed in real-time by an FPGA and commercially available ADCs, as this approach does not require an expensive and time consuming IC design. In the following subsections different components were described in more detail.

5.1.1 16-QAM signal generation

The transmitter comprises a commercial ECL having a linewidth of approximately 150 kHz and an IQ-modulator driven by two 625 Mbaud quaternery data streams which are generated by an FPGA. The 16-QAM data is generated with a Xilinx Virtex-II Pro™X Platform FPGA characterization board (MK325) using XC2VP70X. This FPGA offers 20 RocketIO X Multi Gigabit Transceivers ranging from 2.488 Gb/s to 6.5 Gb/s per channel, and provides a seamless migration path for higher performance serial applications. To reduce the symbol rate of the transmission system, parallel processing of the data has to be applied inside the FPGA (i.e. I/O Multi Gigabit Transceivers). The number of parallel modules depends on the target symbol rate, for 2.5 Gb/s an amount of 16 parallel modules will be sufficient. The serial transceivers were reduced from 2.5 Gb/s to 625 Mb/s by selecting each four bits into one, and this will help to reduce the symbol rate and to synchronize the output data. The multi-gigabit transceivers are used for parallel to serial conversion. The transmission clock is generated from one of the multi-gigabit transceiver by transmitting an alternating "1010 ..." sequence at twice the symbol rate of the system.

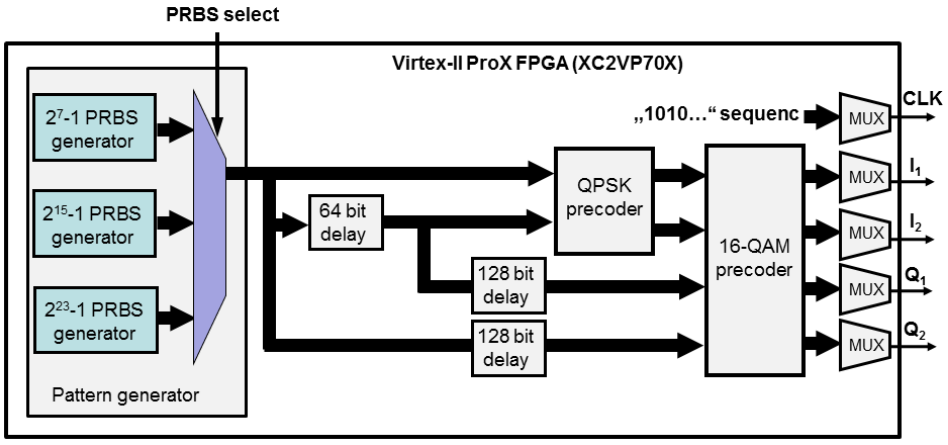

Figure 5.2: Block diagram for the implemented 16-QAM signal in an FPGA

The block diagram of 16-QAM signal generator inside a Virtex-II FPGA is shown in Figure 5.2. Four pseudo-random bit sequences of different lengths ($2^7 - 1$, $2^{15} - 1$, $2^{23} - 1$) were generated at a data rate of 625 Mb/s. The data were first mapped to the

constellation points before the quadrant number was differentially precoded to cope with quadrant phase slips during receiver-side carrier synchronization. To resolve the fourfold ambiguity of the estimated optical phase within the receiver, the quadrant numbers of the in-phase and quadrature data streams are modulo 4 differentially encoded. All four subchannels (I_1, Q_1, I_2 and Q_2) are amplified with four modulator drivers (TriQuint). The generated waveforms are passively combined to form two 4-level 625 Mbaud electrical waveforms for in-phase and quadrature modulation. The levels of the most and least significant bit (MSB, LSB) are coarsely set using fixed 6 dB attenuators in one path. The IQ-modulator is a double-nested MZM based on $LiNbO_3$. An external dip switch in the FPGA is used to control the system for synchronization and data mode, selecting the length of the PRBS sequence, and to select data type between QPSK and 16-QAM mode for driving a dual-parallel MZM (DPMZM) setup. ECLs are employed in a self-homodyne or a heterodyne arrangement. For self-homodyne detection the signal passes an EDFA and is then split optically by a 3 dB coupler. One signal portion is fed into an IQ-modulator for transmission (TX) while the other portion replaces the local oscillator (LO) laser for coherent reception. Figure 5.3 shows a photograph of the implemented transmitter.

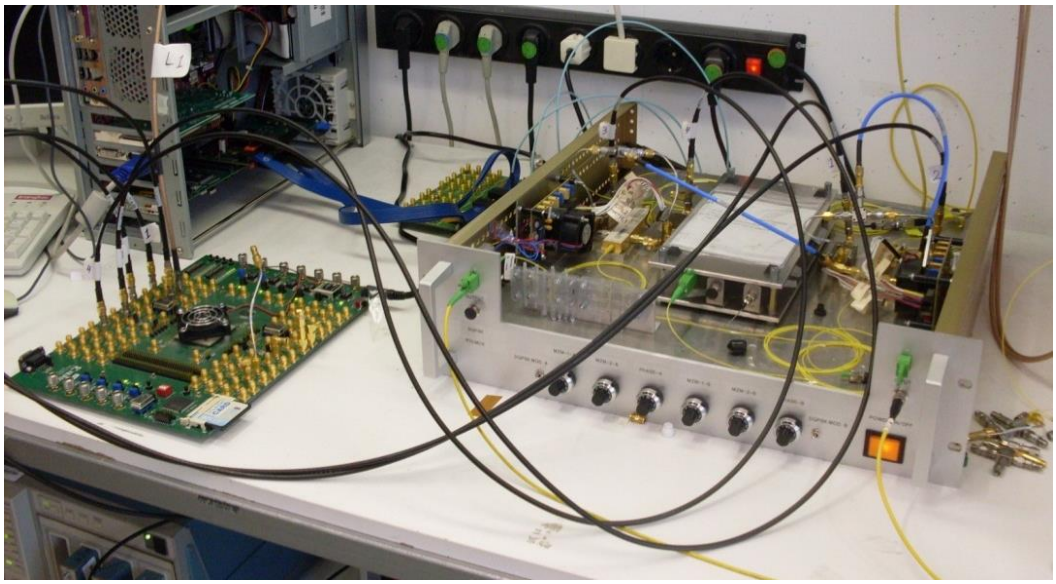

Figure 5.3: 16-QAM transmitter with conventional IQ setup.

5.1.2 Coherent optical receiver frontend

Figure 5.1 shows the experimental setup. After transmission through 20 or 100 km of standard SMF, the signal is fed to a variable optical attenuator (VOA), followed by an EDFA and a ∼20 GHz wide bandpass filter for noise filtering. Then the received signal

was fed into a $LiNbO_3$ optical 90° hybrid, where it was superimposed with the LO signal provided from optical switch which can change the setup between self-homodyning with the signal laser and heterodyning with an additional ECL. The polarizations of the LO and received signals were matched manually by using quarter-wave plate arrays. The outputs of the optical 90° hybrid were detected by two differential photodiode pairs. Their output currents were converted to voltage signals by resistive loads and amplified by two 10 GHz bandwidth amplifiers. Figure 5.4 and Figure 5.5 show the implemented component in the coherent receiver testbed.

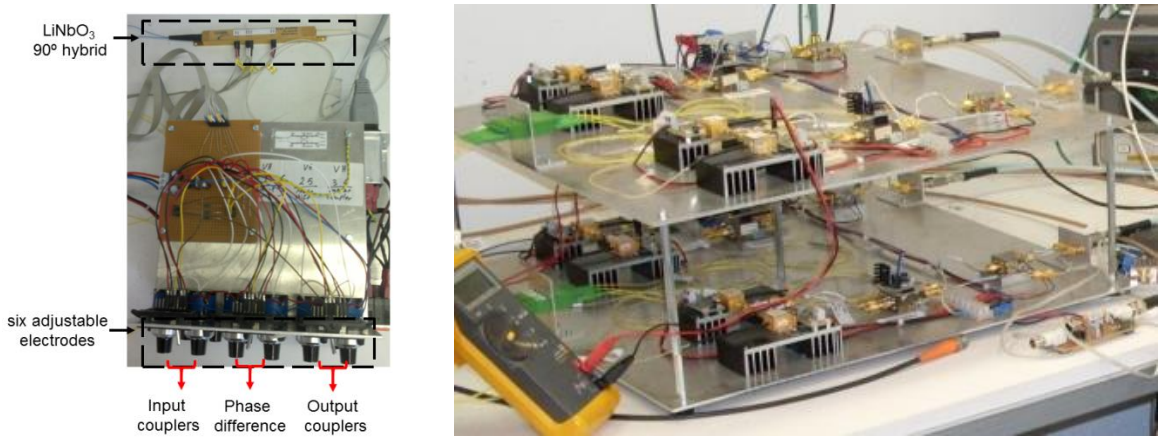

Figure 5.4: $LiNbO_3$ optical 90° hybrid and associated control unit (left), and differential photodiode pairs and amplifiers (right).

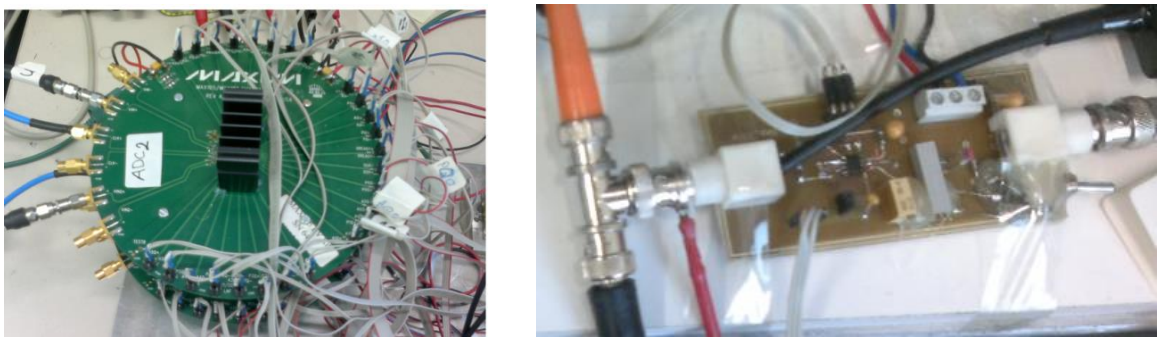

Figure 5.5: Commercially available ADCs (left), and PI controller (right).

5.1.3 Digital signal processing unit

After photodetection and linear amplification the signals are converted into the digital domain. In the receiver a MAX105 evaluation kit was used for analog-to-digital conversion with dual channel, 6 bit (800Ms/s), and it can process differential or single-ended analog inputs, as shown in Figure 5.5(left). Therefore for 2.5 Gb/s 16-QAM signal, the electrical I&Q signal components are amplified before being sampled in two ADCs at

the symbol rate of 625 MHz. Interconnections between the dual ADC board and the FPGA are implemented in low-voltage differential signalling (LVDS) that provide digital outputs with an internal $6{:}\,12$ demultiplexer to reduce the received data rate to one half the sample clock rates. This allows easier interfacing with the subsequent DSPU, as shown in Figure 5.6. Data are output from ADCs in two's complement format. Two types of FPGAs with Xilinx Virtex 4 FPGA (XC4VSX35) and Xilinx Virtex 6 FPGA (XC6VML605) were employed to verify and evaluate DSP algorithms in real-time experiments, where two different electronic carrier and data recovery methods are implemented. In both cases signals are processed in $M = 8$ demultiplexed parallel streams, thereby reducing the internal clock frequency to 78.125 MHz. Due to pure feed-forward approaches in both carrier recoveries the DSP can hence be adapted to any transmission rate by increasing M. An external PI controllers are needed for clock recovery (not shown in Figure 5.1) and for heterodyne experiments, as shown in Figure 5.5(right) [95, 66].

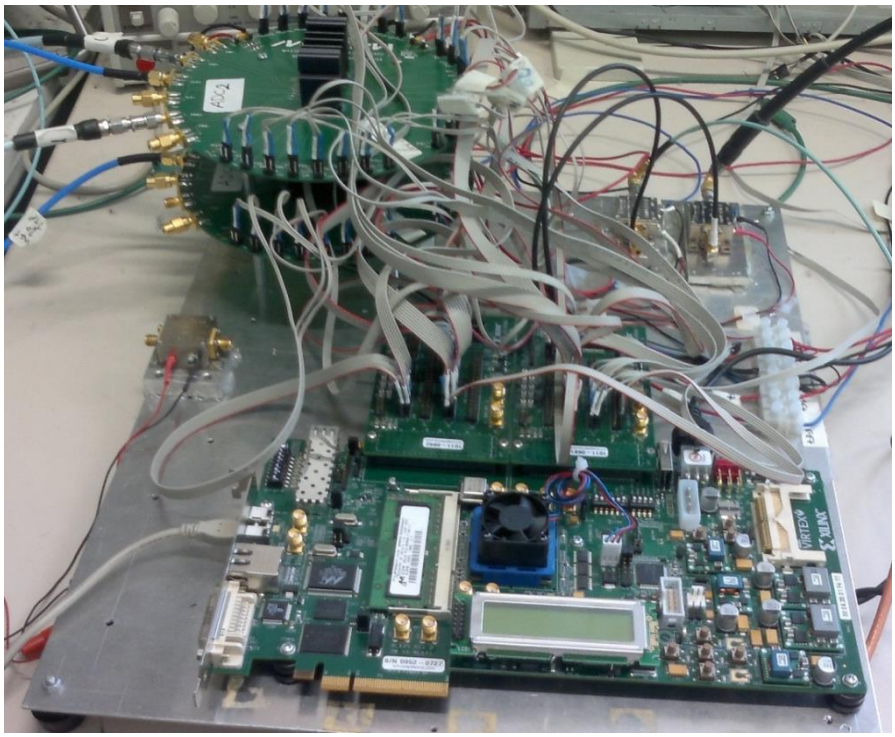

Figure 5.6: FPGA based coherent receiver.

5.2 Real-time transmission

The following subsections discuss the performance of a real-time 16-QAM transmission system. 2.5 Gb/s 16-QAM data was transmitted over 20 and 100 km of standard single-mode fiber. The individual strengths and drawbacks of most dominant feed-forward carrier

recovery algorithms [93, 73] have been investigated in relation to important system parameters such as noise performance, optimal phase estimation filter length, laser linewidth, external quantization limitation by ADC resolution and the effect of test phase angle resolution. Moreover, the influence of different four-level driving voltage ranges to the IQ modulators has been tested.

5.2.1 Nonlinear effect of IQ modulator experiment

In this experment, the influence of linear and nonlinear effects related to the IQ-modulator of a 16-QAM coherent transmission system has been investigated in a real-time transmission [49].

To evaluate the effects of the MZMs to a 16-QAM signal, two nonideal DPMZMs with different extinction ratio have been tested. Each modulator design is based on dual parallel structure of two MZMs embedded in a Mach Zehnder super-structure, implemented on a proven and high stability x-cut substrate. Both MZMs within the same IQ-modulator are identical and they have the same values of input amplitudes of the electrical signals. The two parallel MZMs are integrated on a $LiNbO_3$ substrate. The first DPMZM was from Photline (QPSK_LN_40) with maximum $40\ \mathrm{Gbit/s}$ maximum optical transmission, while the second one was from Avanex (SD50-DP) with $50\ \mathrm{Gbit/s}$ maximum optical transmission. Both modulators are based on dual high bandwidth; supported with low MZM power transfer function ($V_\pi = 7.5\mathrm{V}$ and $V_\pi = 3.5\mathrm{V}$) and an extinction ratio ($ER = 50\ \mathrm{dB}$ and $ER = 25\ \mathrm{dB}$), respectvely.

From the optical transmission system shown in Figure 3.10, the bit error ratio (BER) versus received power is measured for $2^7 - 1$ PRBS data and over a distance of 1.6 km of SMF. All amplitudes of the MZMs need to be carefully adjusted to obtain a good pattern and avoid phase error [53, 54]. $-5\ \mathrm{dBm}$ and $-9\ \mathrm{dBm}$ optical launch power was selected where the nonlinear effect becomes clear for comparison. After optical transmission, the received electrical signals are amplified and sampled with 6 bit ADCs, where the outputs are connected to a Xilinx Virtex 4 FPGA that contains the digital carrier and data recovery. Phase estimation was implemented as BPS with $B = 16$ test carrier phase angles and $N = 6$ temporal samples before and after the current sample are processed to recover the carrier. Figure 5.7 shows the BER of all I&Q subchannels versus preamplifier input power for various α and Δ values. From the BER curves, the dependences on α and Δ are deduced. The lowest BER values were measured for $\alpha = 0.5$ and $\Delta = 0.5$. A BER floor

was observed, below the threshold of a state-of-the-art FEC (7% overhead). For a given $\alpha = 0.5$, corresponding Δ was varied with steps of ~0.2. The BER changed as a function of Δ in the given range, especially when Δ is far away from the optimal condition (i.e. $\Delta = 1$). The reason for this is that the nonlinear transmittance of the MZM is affected severely when Δ is increased.

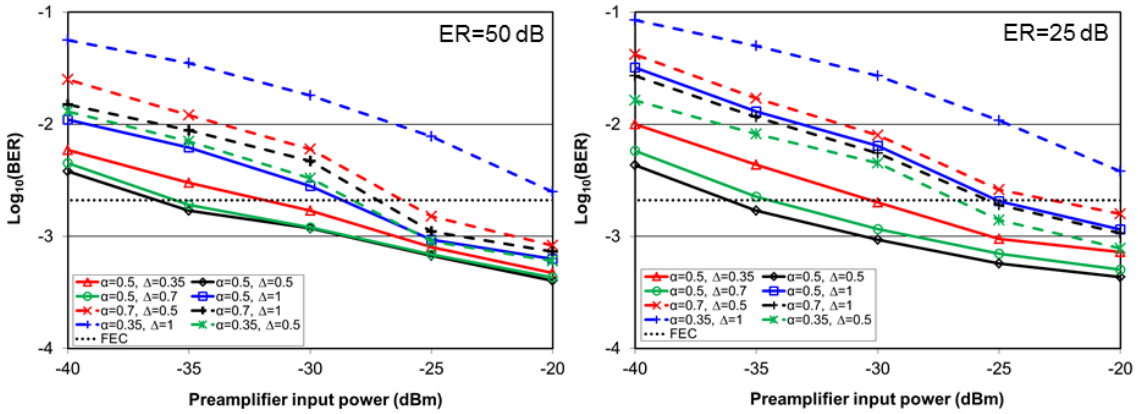

Figure 5.7: 16-QAM BER curves for various α and Δ values for $ER = 50$ dB (left), and for $ER = 25$ dB (right); averaged over all 4 subchannels (I1, Q1, I2 and Q2). Fiber length was 1.6 km and -5 dBm fiber launch power.

Figure 5.7 shows that the case of optimum parameters $\alpha = 0.5$ and $\Delta = 0.5$ are almost independent from the ER. The necessary preamplifier input power for reaching the threshold ($2 \cdot 10^{-3}$) of state-of-the-art FEC (7% overhead) is shown in Table 5.1 for both modulators.

Table 5.1: Fiber input power at FEC threshold ($2 \cdot 10^{-3}$) for $ER = 50$ dB and $ER = 25$ dB.

	$ER = 50\,dB$	$ER = 25\,dB$
$\alpha = 0.5, \Delta = 0.5$	– 36.5 dBm	– 36.2 dBm
$\alpha = 0.5, \Delta = 0.35$	– 32 dBm	– 30.5 dBm
$\alpha = 0.5, \Delta = 0.7$	– 35.5 dBm	– 34.8 dBm
$\alpha = 0.5, \Delta = 1$	– 28.7 dBm	– 25 dBm
$\alpha = 0.35, \Delta = 0.5$	– 28.3 dBm	– 26.8 dBm
$\alpha = 0.35, \Delta = 1$	–	–
$\alpha = 0.7, \Delta = 0.5$	– 26.5 dBm	– 23.5 dBm
$\alpha = 0.7, \Delta = 1$	– 27.5 dBm	– 25.3 dBm

From the Q-factor dependence from the parameter α in Figure 3.14, the best received values of Q-factor are measured when the optimal values of the parameters are applied (Figure 5.8). The maximum required Q-factor becomes monotonically decreasing when Δ is far away from optimal value in the given range, especially when (Δ→ 1). This is because of the nonlinear transmittance of MZM is affected severely when Δ is increased. The 16-QAM transmission system with $ER = 50$ dB shows a better performance comparing to $ER = 25$ dB when launch and receive powers are reduced. The overall performance is better with larger ER.

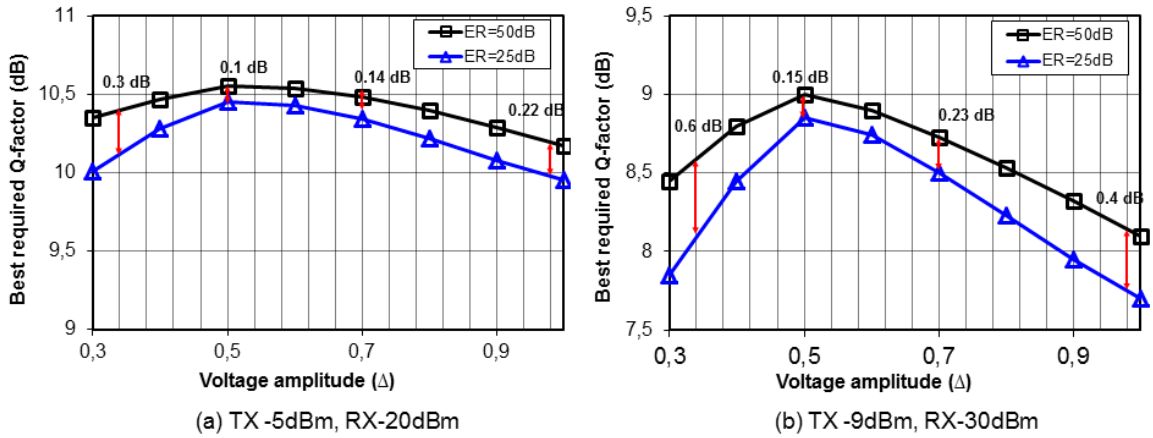

Figure 5.8: Q-factor dependence with the variation of the parameter α for different fiber input power and different received preamplifier input power.

According to the results, the parameter α should be in the range of 5 dB to 6 dB. In this case variations of Δ can be tolerated in the range of 0.4…0.6 for a BER less than the FEC limit (7% overhead) at receiver input power below –30 dBm.

5.2.2 Real-time phase-noise-tolerant experiment

This experiment presents the implementation of a phase-noise-tolerant, hardware-efficient feed-forward carrier recovery [94, 96]. The setup of the 2.5 Gb/s 16-QAM transmission system is shown in Figure 5.9. The drive signals are generated using FPGA. The signals are determined using for copies of a PRBS of length $2^7 - 1$ which mutually have been delayed. Two sequences are considered the most significant bits (MSB_I, MSB_Q). They are differentially encoded and define the quadrant of the square 16-QAM constellation. The other two sequences are considered the least significant bits (LSB_I, LSB_Q) and are used without further encoding to select the in-phase and quadrature amplitude levels within the quadrant. The levels of the most and least significant bits (MSB, LSB) are coarsely set using fixed 6 dB attenuators in one path. The resultant approximately 200mVpp 4-level

signal is applied to the single-drive I and Q arms of an integrated $LiNbO_3$ double-nested MZM with a 3 dB bandwidth of 10 GHz and a V_π of approximately 7.5 V. As light source a tunable ECL with a power of 1.5 dBm and a specified linewidth of 150 kHz is used. The optical intensity eye diagram with its three intensity levels corresponding to the three rings that make up a square 16-QAM constellation, cf. also in Figure 5.9. The fiber launch power at the TX-EDFA output is –2 dBm. After transmission through 100 km of SMF, the signal is fed into a VOA and is amplified by an EDFA, followed by a ~20 GHz wide bandpass filter for noise filtering. A manual polarization controller is used to control the SOP entering the optoelectronic receiver frontend. There the signal and the local oscillator laser are superimposed by a $LiNbO_3$ 90° optical hybrid and detected in two differential photodiode pairs. The outputs of the photodetectors are connected through amplifiers to the ADC.

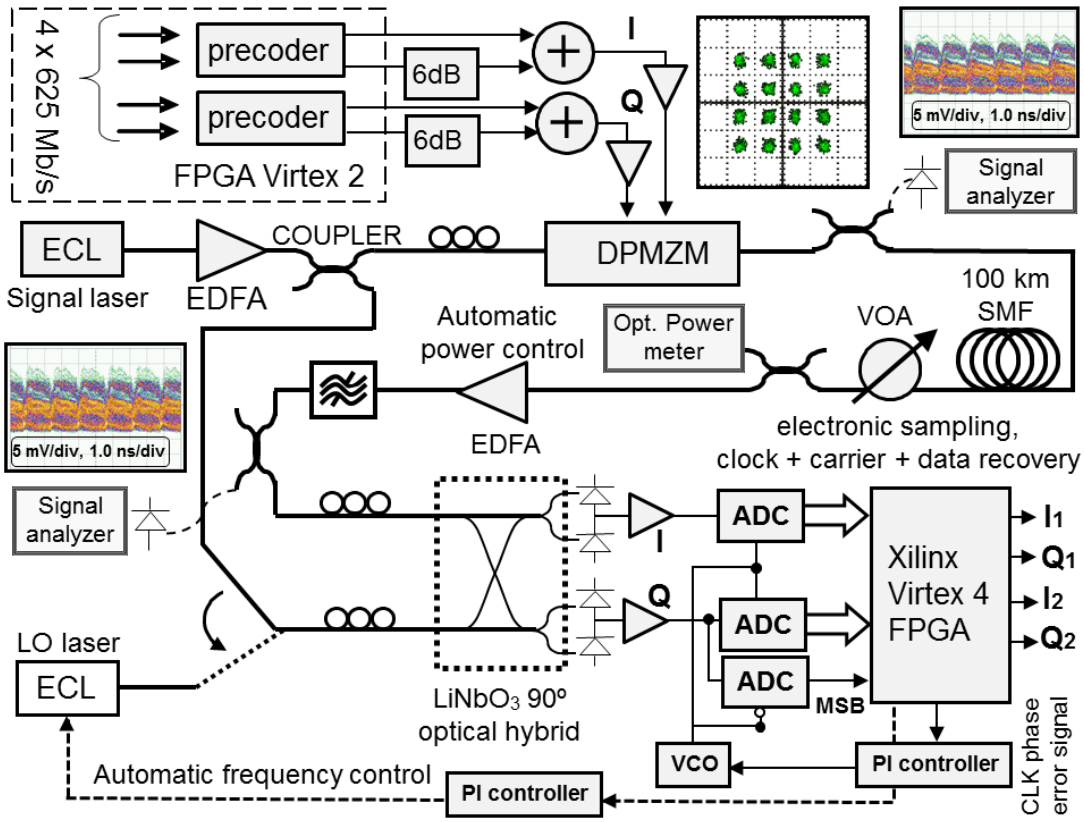

Figure 5.9: 16-QAM transmission setup with real-time synchronous coherent digital I&Q receiver.

The ADCs sample the input signals at the symbol rate of 625 MHz and a nominal resolution of 6 bit. The ADCs interface with a Xilinx Virtex 4 FPGA where carrier and data are recovered electronically. For clock recovery a second time-interleaved ADC pair is used to provide the required oversampling [66]. To obtain a clock phase error signal the

signs of adjacent input samples are correlated [95] and fed out to an external PI controller which controls a voltage-controlled oscillator and closes a phase-locked loop. For BPS carrier recovery the primary received I&Q samples are combined as a symbol pointer in the complex plane and rotated into the first quadrant. Then they are rotated within the quadrant in parallel by $B = 16$ test carrier phase angles [28]. The squared distance between the recovered 16-QAM symbol and the closest constellation point are filtered over $2N + 1$ consecutive symbols. That test phase angle where the filtered squared distance is minimum yields the correct constellation point within a quadrant, i.e. data bits I_2, Q_2. Data bits I_1, Q_1 are obtained by differential modulo 4 decoding of the quadrant number. This prevents occurring quadrant phase jumps of the recovered carrier from falsifying all subsequent data, but results in some deviations from ideal Gray coding (Figure 4.9). For signal processing, the FPGA is configured into $M = 8$ parallel modules. The internal clock frequency is therefore 78.125 MHz. Carrier recovery does not contain any feedback loop, so it can be adapted to any transmission rate by increasing M. The optimum response halfwidth N of the squared-distance filter depends on the laser-sum-linewidth-times-symbol-interval-product ($\Delta f \cdot T$). For this experiment, there has been chosen $N = 6$, which worked best. For BER measurement, appropriate patterns are programmed into the BER tester. While the hardware effort for carrier recovery is on the order of $B = 16$ times larger than for QPSK, capacity is all the same doubled. Also, equalizers typically consume much more silicon floorspace than QPSK carrier recoveries. In the future, a two-stage version [82] of the implemented concept could reduce hardware effort further.

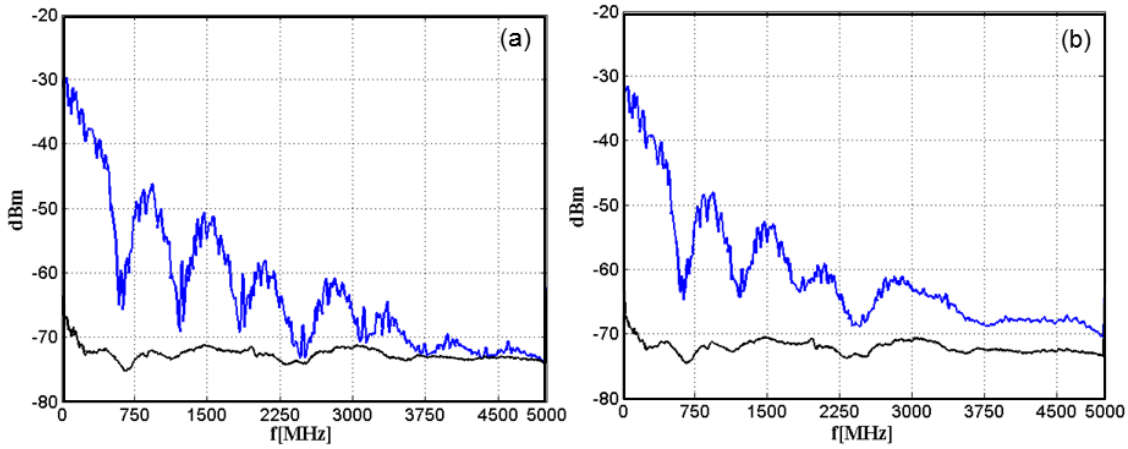

Figure 5.10: Electrical spectra in one quadrature with either aligned (top) or orthogonal (bottom) signal and LO polarizations, showing signal and noise, for -20 dBm (a) and -45 dBm (b) preamplifier input power.

Electrical data transmission was error-free. A SNR of 35 dB was measured at one ADC input, using electrical noise power in a 312.5 MHz band and the total electrical signal power. Corresponding spectra are shown in Figure 5.10.

Figure 5.11 shows BER versus received power for 2.5 Gbit/s with self-homodyne detection and over distances of 20 and 100 km. Clock was either supplied directly from the transmitter or recovered in the receiver. The BER deviations between the receiver setups with and without clock recovery show the influence of timing jitter depending on transmission distance. The best measured BERs were at $1.18 \cdot 10^{-4}$ and $1.0 \cdot 10^{-4}$ for 20 km, and $6.1 \cdot 10^{-4}$ and $2.75 \cdot 10^{-4}$ for 100 km of fiber, for direct clock and clock recovery, respectively. All measurements were repeated several times and turned out to be stable. The total capacity of the conducted 625 Mbaud experiment is 4×625 Mb/s or 2.5 Gb/s.

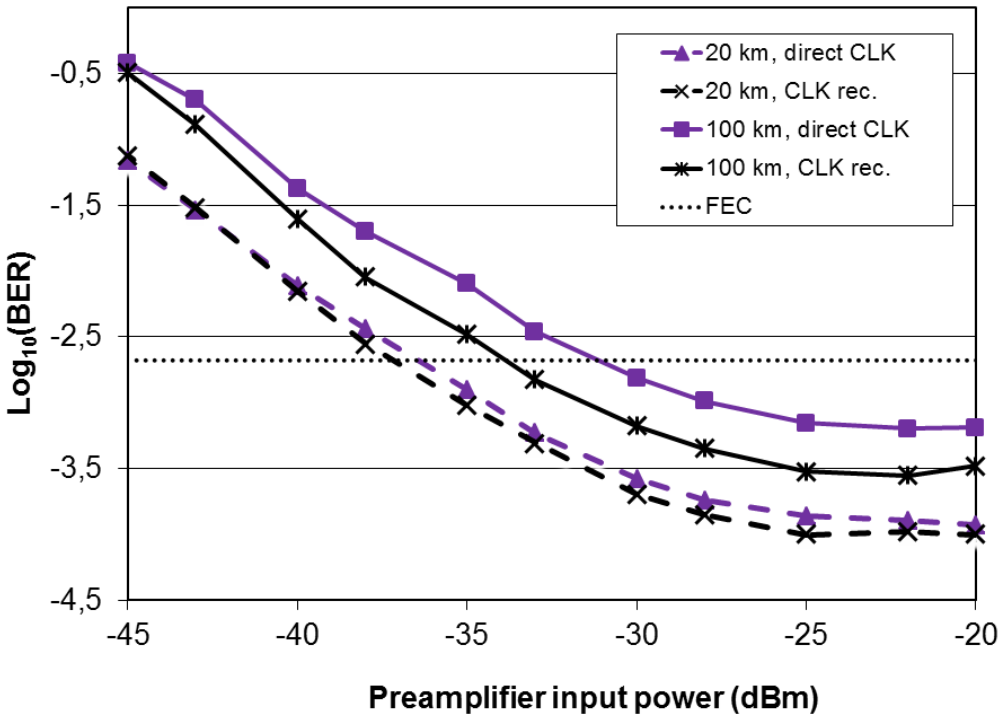

Figure 5.11: Measured BER vs. optical power at the preamplifier input, averaged over all 4 subchannels (I1, Q1, I2 and Q2) at 2.5 Gb/s data rate.

Figure 5.12 shows the measured BERs versus preamplifier input power, averaged over I&Q but separated for inter-quadrant bits (IQ1), Gray-encoded as in [28], and intra-quadrant bits (IQ2). The distance was 100 km. Intra-quadrant decoding is limited more strongly than inter-quadrant decoding, presumably by intersymbol interference (ISI) in the

non-ideal electrical transmitter. This is seen from the fact that the BER of I_2 and Q_2 (inside quadrant) is higher than the BER of the quadrant numbers I_1 and Q_1. Based on simulations without ISI the ideal estimated BER floor is at 10^{-4} for the tested $\Delta f \cdot T = 0.00048$. Averaged over all 4 subchannels (I_1, Q_1, I_2 and Q_2) at received powers larger than -30 dBm, the measured BER was less than the FEC limit ($2 \cdot 10^{-3}$) for all cases. FEC was not applied within this experiment.

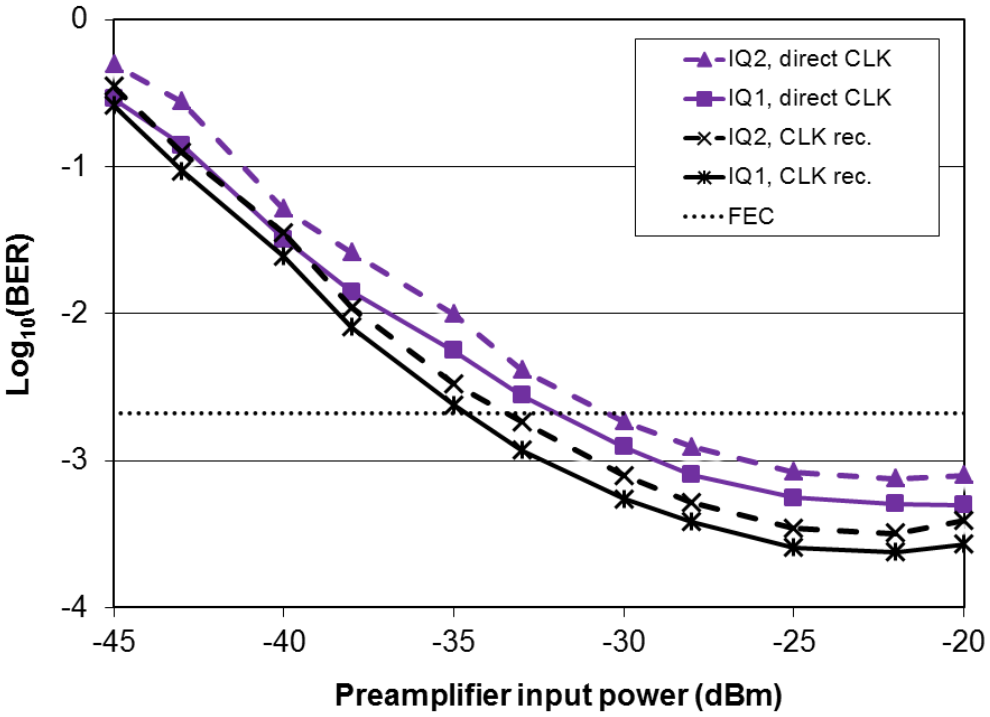

Figure 5.12: Measured BERs of 16-QAM bits 1 and 2, each averaged over I&Q, vs. optical power at preamplifier input. Fiber length was 100 km.

For heterodyne experiment a second ECL was added and used as LO source. Laser linewidths were specified as < 150 kHz. The field information of the optical signal will transferred to electrical carrier at an intermediate frequency (IF) which is corresponds to the frequency difference between signal and LO. The IF should be less than 1% of the symbol rate. R. Noé employed in [97] a delay line frequency discriminator to detect the frequency offset. Therefore an automatic frequency control for the LO laser is implemented inside the FPGA [66]. The observed carrier phase jumps between subsequent symbols are output from the FPGA and fed into a PI controller. The resulting signal controls a portion of the LO bias current [66]. Two techniques of feed-forward carrier phase recovery BPS with $N = 6$ and QPSKP with $N = 9$ and 6 were implemented.

Figure 5.13 shows the BER characteristics for heterodyne setup with clock recovery. After transmission over distance of 20 km the best measured BER result is $2.25 \cdot 10^{-4}$ for BPS while $2.6 \cdot 10^{-4}$ and $4.5 \cdot 10^{-4}$ for QPSKP with $N = 9$ and 6, respectively. For 100 km the measured BER floors were $4.3 \cdot 10^{-4}$ for BPS while for QPSKP the BER floors were $4.8 \cdot 10^{-4}$ and $1.1 \cdot 10^{-3}$ for $N = 9$ and 6, respectively. A similar performance for BPS and QPSKP with a filter-half width of $N = 9$ can be observed for all experiments. The power penalty was approximately 4 dB between BPS and QPSKP for the same filter half-width N.

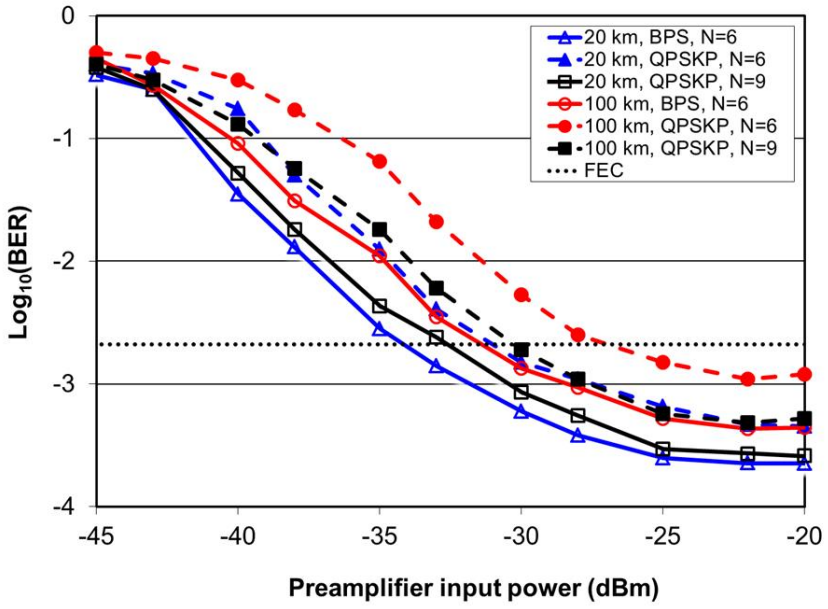

Figure 5.13: Measured BER vs. optical power at the preamplifier input, for heterodyne detection and with clock recovery.

According to simulation [28], the experimental response half-width $N = 6$ of BPS carrier recovery is optimum for a single-polarization 16-QAM system with good receiver sensitivity and phase noise tolerance. This is important because a high received power would always tolerate much phase noise, simply by lowering N. The implemented carrier recovery algorithm is compatible with all kinds of equalizers for polarization control, chromatic dispersion and polarization mode dispersion.

5.2.3 Optimal receiver filter length

In order to remove noise distortions, different filter half-width N were tested. The amount of filter half-width value depends on $\Delta f \cdot T$. To reduce the hardware effort inside the FPGA, the amount of filter half-width should be carfully selected. If the value of the filter

half-width is sizeable, then the usable slice inside the FPGA become unfeasible. In these experments [98, 99] different filter lengths (half-width N) were evaluated for both feed-forward carrier recovery techniques. Figure 5.14 shows an optical transmission system where 2.5 Gb/s data are transmitted over 20, 40 and 100 km of SMF and received in a real-time I&Q self-homodyne setup with standard ECL, clock was supplied directly from the transmitter.

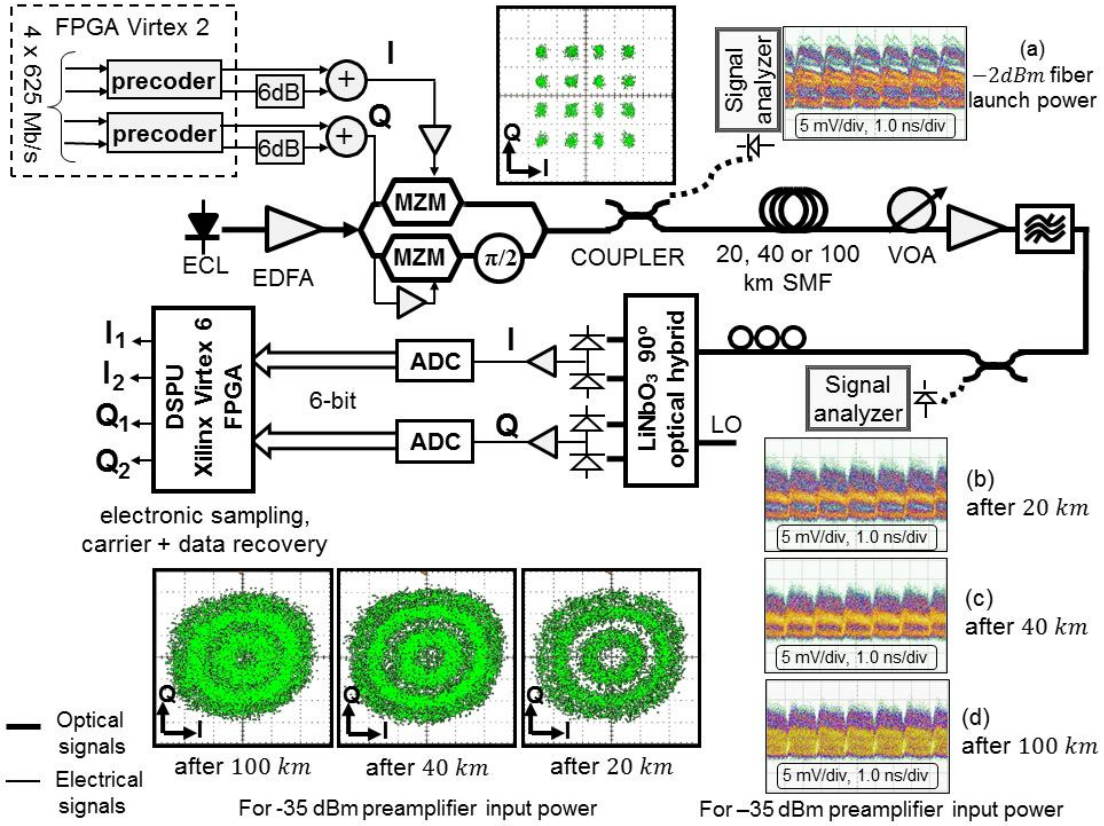

Figure 5.14: 16-QAM transmission setup with constellation and optical intensity eye diagram before and after optical transmission over 20, 40 and 100 km, for −2 dBm TX launch power and −30 dBm RX preamplifier input power.

5.2.3.1 PE filter length tolerance using QPSKP experiment

In this experment QPSKP is implemented with different filter response half-widths which has been selected with $N = 6, 9, 12$ and 15 [99]. These values were selected to meet system performance for laser-linewidth-times-symbol-rate product ($\Delta f \cdot T = 0.00048$). The BER floors versus received power are discussed for the different setups.

Figure 5.15 shows the BER behavior for PRBS data length of $2^7 - 1$. A 1.3 dB penalty can be observed in the BER curve between filter-half width of $N = 15$ and $N = 9$ to the RX input power for 20 km. As phase noise increases, the filter-half width of $N = 9$ shows

better performance to $N = 15$ with 0.5 dB and 2.8 dB penalty in the BER curve to the RX input power for 40 and 100 km of single-mode fiber, respectively. This is due to strong phase noise which needs a smaller filter-half width to achieve a lower mean squared phase estimation error. The filter with $N = 9$ allows reaching a lower BER floor than the filter with $N = 15$. A filter with $N = 6$ is not efficient for ($\Delta f \cdot T = 0.00048$).

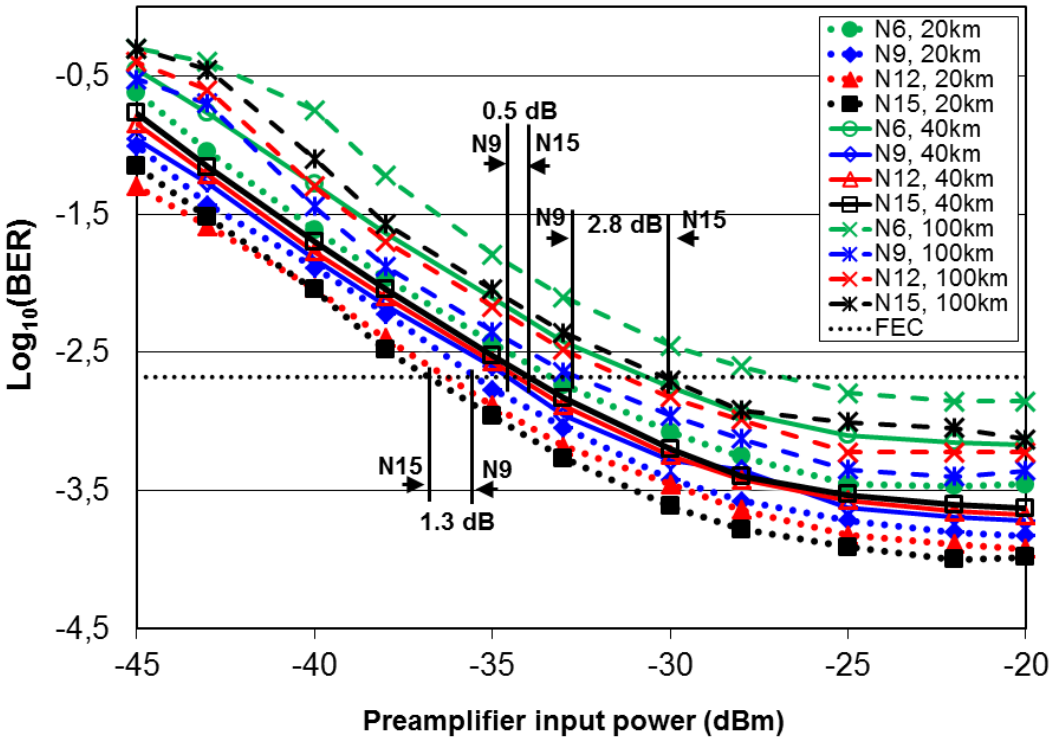

Figure 5.15: Measured BER for the average I&Q subchannels vs. optical power at preamplifier input for PRBS length $2^7 - 1$. Fiber lengths was 20, 40 and 100 km.

The necessary received fiber input power for reaching the threshold ($2 \cdot 10^{-3}$) of state-of-the-art FEC (7% overhead) is shown in Table 5.2 for different filter-half width.

Table 5.2: Fiber input power at FEC threshold ($2 \cdot 10^{-3}$) for different filter-half widths.

	20 km	40 km	100 km
$N = 6$	– 33.2 dBm	– 30.6 dBm	– 27 dBm
$N = 9$	– 35.5 dBm	– 34.5 dBm	– 32.8 dBm
$N = 12$	– 36.3 dBm	– 34.2 dBm	– 31.3 dBm
$N = 15$	– 36.8 dBm	– 34 dBm	– 30 dBm

5.2.3.2 PE filter length tolerance using BPS experiment

In this experment [98], the phase estimator rotates the received symbols into the first quadrant. Then they are rotated within the quadrant in parallel by 16 test carrier phase angles. The squared distance of the recovered 16-QAM symbol and the closest constellation point (in whichever quadrant) is filtered over a number of consecutive symbols. That test phase angle where the filtered squared distance is minimum yields the correct constellation point within a quadrant.

The carrier recovery bandwidth was chosen to be optimum for a single-polarization 16-QAM system with good receiver sensitivity and phase noise tolerance. This is important because a high received power would always allow tolerating much phase noise, simply by increasing the carrier recovery bandwidth. Figure 5.16 shows the measured BER versus optical power at preamplifier input over distances of 20 and 100 km SMF and for different filter half-width N values. In case of 20 km the BER floors were below the FEC limit (7% overhead) until the preamplifier input power was set below -29 dBm for $N \geq 4$. Up to -36.5 dBm received preamplifier input power and $N \geq 6$ yielding BERs below FEC limit. For 100 km the optimal received fiber preamplifier input power was located till -25.5 dBm for $N \geq 5$. Up to -31.8 dBm received preamplifier input power and $N \geq 6$ the BER of 16-QAM signal were below FEC limit(dotted line). The BER for 100 km are higher than for 20 km, this is because of direct clock from the transmitter are used in these experiments.

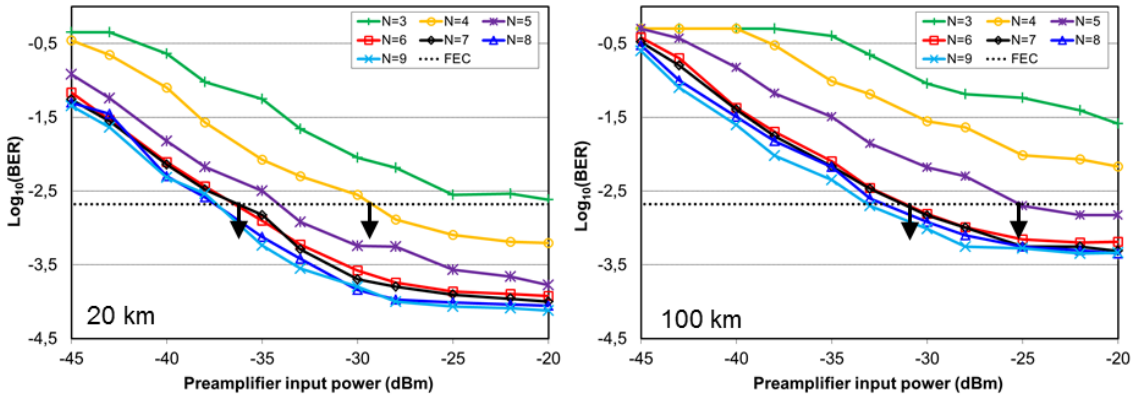

Figure 5.16: Measured BER vs. optical power at preamplifier input for different filter half width N, for 20 km (left) and 100 km (right). Pattern length$2^{7} - 1$.

Finally, $N \geq 6$ will be a fairly good choice for $\Delta f \cdot T = 0.00048$. These experimental results are in accordance to the simulation [28].

5.2.4 Phase noise effects

The phase noise in 16-QAM transmission is mainly contributed from laser sources, optical amplifiers and non linear effects in optical fibers. The amplified spontaneous emission (ASE) noise itself induced phase noise well behaves as AWGN. Therefore, the expermental investgations are separated into two parts including laser phase noise and transmisson phase noise, respectively [100]. The experimental setup is shown in Figure 5.9.

5.2.4.1 Laser phase noise tolerance

The laser phase noise is characterized by its linewidth. The requirement for the laser linewidth in M-QAM systems becomes much more stringent as M increases. Therefore, it is important to take laser linewidth into account. The output of a single-frequency laser is not perfectly monochromatic but rather exhibits some phase noise. This leads to a finite linewidth of the laser output. To investigate laser linewidth effects, two commercial ECLs with 150 and 180 kHz laser linewidth were used. In this work, for experimental convenience, PRBS (7, 15, and 23) were used as modulator driving data. BPS and QPSKP carrier phase estimation methods have been tested and compared by each other to present the performance against phase noise. Data throughputs of 2.5 Gbit/s and 1.25 Gbit/s were achieved in an FPGA-based coherent receiver with self-homodyne detection with direct clock from transmitter. Different laser-sum-linewidth-times-symbol-interval-products ($\Delta f \cdot T = 0.00048$, 0.000576, 0.00096 and 0.001152) have been tested.

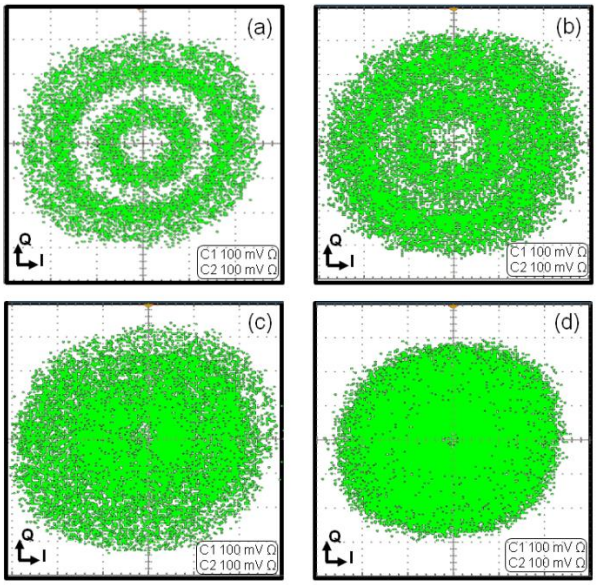

Figure 5.17: Constellation maps of 16-QAM signal affected by phase noise after 20 km of optical transmission at a SNR of 35 dB for $\Delta f \cdot T = 0.00048$ (a), 0.000576 (b), 0.00096 (c) and 0.001152 (d).

Figure 5.17 shows the observed 2.5 Gb/s (625 Msymbol/s) (upper) and 1.25 Gb/s (312.5 Msymbol/s) (lower) constellation diagrams with an ECL of 150 kHz spectral linewidth (left side) and with an ECL of 180 kHz spectral linewidth (right side), respectively. The constellation diagrams showing phase changes for different levels of phase noise (low noise, medium noise, high noise and very high noise) for each $\Delta f \cdot T$, respectively. The results show that the phase noise can be squeezed by reducing the amount of $\Delta f \cdot T$. A back-to-back electrical test, where I&Q electrical data were connected to the I&Q ADCs, turned out to be error-free. Optical receiver sensitivity is limited by thermal and shot noise. The signal power at the photodiodes is therefore chosen so high that imperfect receiver balance can result in significant direct detection of signal and amplified spontaneous emission. To evaluate the BER performance of the self-homodyne phase-diversity receiver for different $\Delta f \cdot T$, the received I&Q samples are recovered by performing the BPS with $B = 16$ test phase angles and $N = 6$ filter half-width.

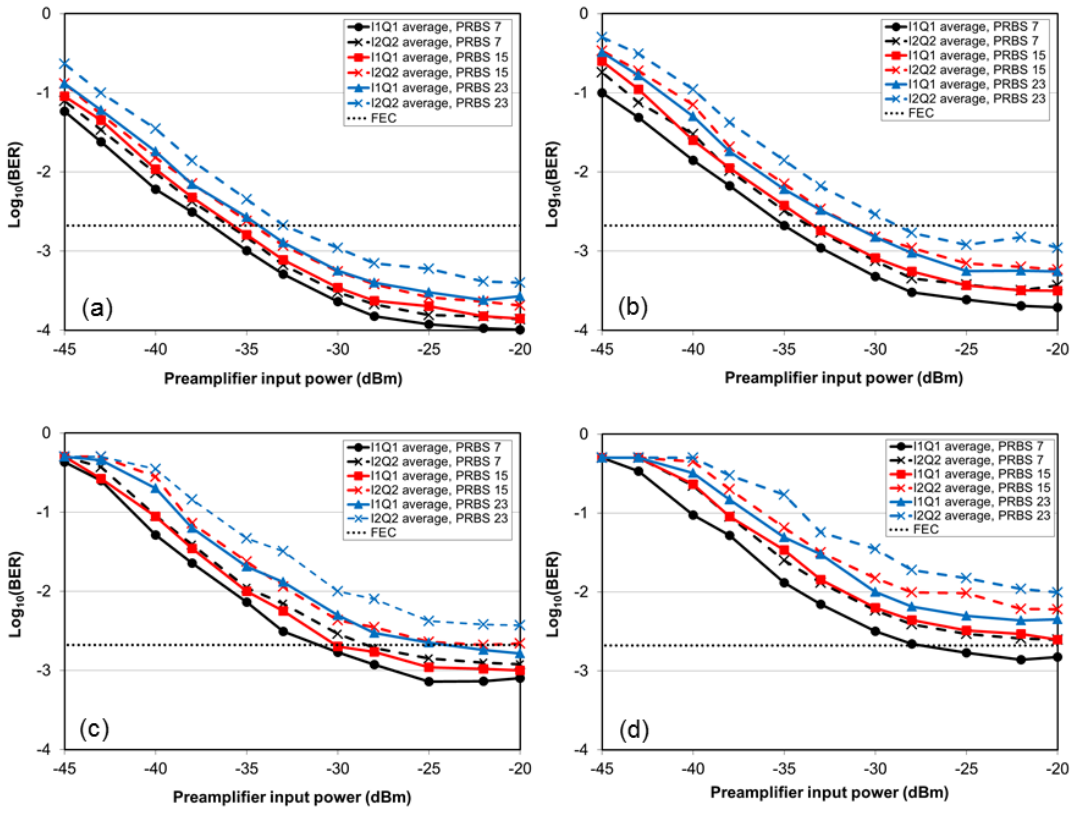

Figure 5.18: BER after 20 km of optical transmission for $\Delta f \cdot T = 0.00048$ (a), 0.000576 (b), 0.00096 (c), and 0.001152 (d); using BPS with $B = 16$, AV IQ1 and IQ2.

Figure 5.18 shows measured BERs versus preamplifier input power, averaged over I&Q but separate for inter-quadrant bits (IQ1) and intra-quadrant bits (IQ2). Intra-quadrant decoding is limited more strongly than inter-quadrant decoding, presumably by

intersymbol interference (ISI) in the non-ideal electrical transmitter. This is seen from the fact that the BER of I_2 and Q_2 (inside quadrant) is higher than the BER of the quadrant numbers I_1 and Q_1.

Figure 5.19 shows the BER versus received power of the averaged over all 4 subchannels (I_1, Q_1, I_2 and Q_2). The best measured BERs were at $1.18 \cdot 10^{-4}$, $2.5 \cdot 10^{-4}$, $9.52 \cdot 10^{-4}$ and $1.9 \cdot 10^{-3}$ for $2^7 - 1$ PRBS data; $1.72 \cdot 10^{-4}$, $4.5 \cdot 10^{-4}$, $1.46 \cdot 10^{-3}$ and $4.03 \cdot 10^{-3}$ for $2^{15} - 1$ PRBS data; and $3.0 \cdot 10^{-4}$, $8.25 \cdot 10^{-4}$, $2.7 \cdot 10^{-3}$ and $6.93 \cdot 10^{-3}$ for $2^{23} - 1$ PRBS data; for $\Delta f \cdot T = 0.00048$, 0.000576, 0.00096 and 0.001152, respectively. The received power is -36.5 dBm at FEC limit (7% overhead) for $\Delta f \cdot T = 0.00048$ and PRBS-7. This result shows an increasing in the FEC BER limit about 2.4 dB, 6.9 dB and 13.6 dB for the same PRBS data length and for $\Delta f \cdot T = 0.000576$, 0.00096 and 0.001152, respectively. FEC was not used in the experment. The 312.5 Mbaud 16-QAM is strongly limited by the laser phase noise and has an apparent BER floor especially when 180 kHz laser linewidth is used.

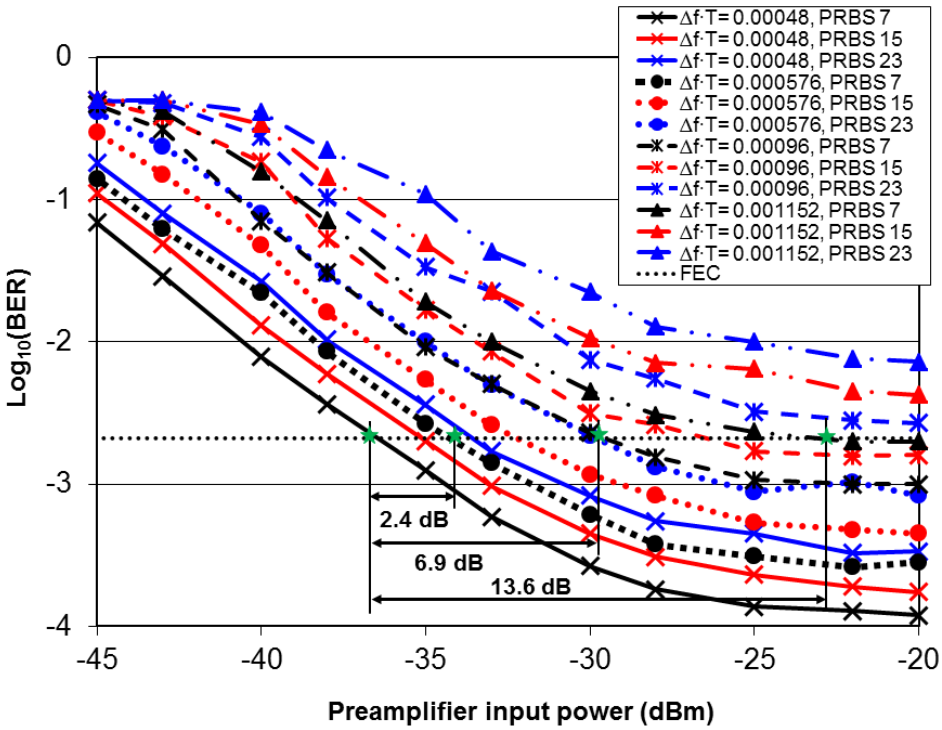

Figure 5.19: Measured BER vs. optical power at the preamplifier input, averaged over all 4 subchannels (I_1, Q_1, I_2 and Q_2) for different $\Delta f \cdot T$. Fiber length was 20 km.

From Figure 5.13, the averaged I&Q channel BERs of BPS with $B = 16$ and filter half-width $N = 6$ shows the same results as for QPSKP with $B = 32$ and $N = 9$. Therefore,

these two techniques are compared with each other and by using the same values of test phase angles $B = 32$. Figure 5.20 shows the BER floors of various receiver input power levels and laser linewidth after transmission over 20 km of SMF, using $2^7 - 1$ PRBS data.

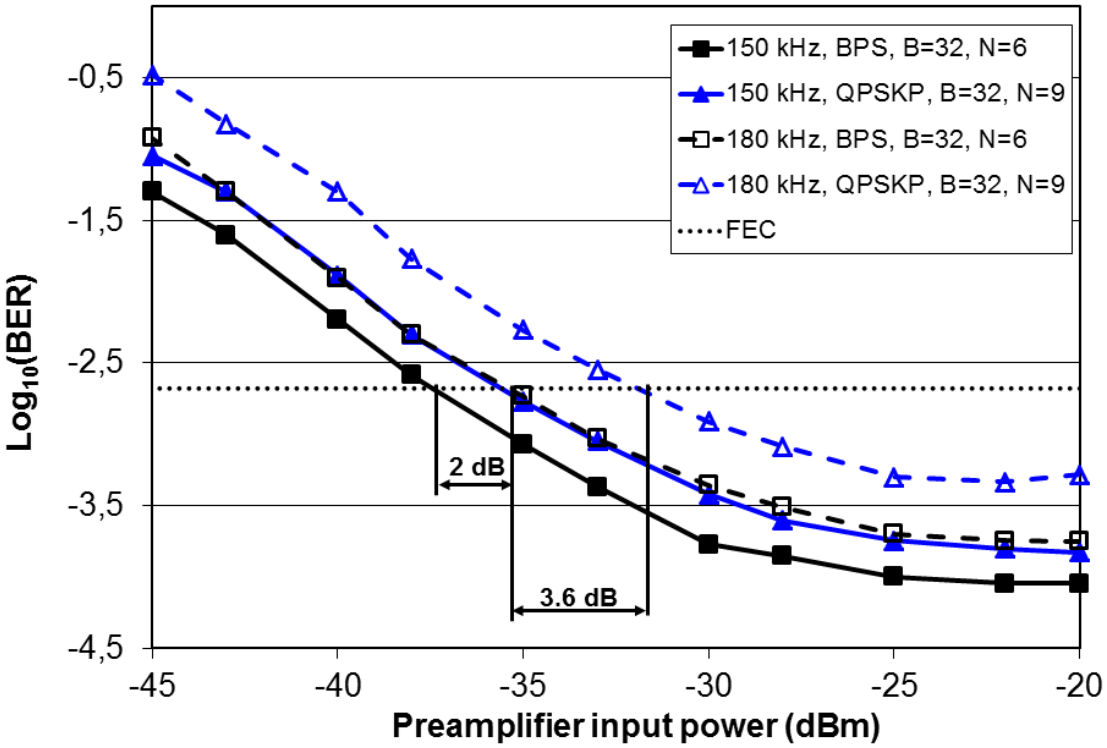

Figure 5.20: BER after 20 km of optical transmission for $\Delta f \cdot T = 0.00048$ vs. $\Delta f \cdot T = 0.000576$ using BPS with ($N = 6, B = 32$) and QPSKP with ($N = 9, B = 32$). Fiber length was 20 km.

The best measured BER for the setup with 150 kHz laser linewidth was $9.0 \cdot 10^{-5}$ and $1.5 \cdot 10^{-4}$ for BPS ($B = 32$ and $N = 6$) and QPSKP ($B = 32$ and $N = 9$), respectively. Both DSP setups could be detected until the preamplifier input power was set below -45 dBm. The BER floors for 180 kHz laser linewidth are slightly higher than for 150 kHz, $1.78 \cdot 10^{-4}$ and $4.65 \cdot 10^{-4}$ for BPS and QPSKP techniques, respectively. Up to -35 dBm received preamplifier input power a 2 dB performance penalty between BPS and QPSKP can be observed for 150 kHz linewidth, while the penalty increases to 3.6 dB for a linewidth of 180 kHz. The tested 150 kHz linewidth BER curves are closer to each other comparing to the 180 kHz ones. The main reason is that the tested 150 kHz linewidth lasers include less frequency jitter, so called $1/f$ frequency noise. This kind of noise leads to overestimation of the laser linewidth but does not degrade BER in high bit rate systems [101]. On the other hand, BPS demonstrates the best phase noise tolerance comparing to the rest of feed-forward carrier recovery algorithms but comes with an expense of high

complexity [28]. This problem can be relieved by reducing the number of test carrier phase angles. The reduction of the symbol rate makes the laser phase noise more critical.

5.2.4.2 Phase noise from optical fiber transmissions

The phase noise from the optical transmission affects the carrier phase estimation and the recoverd signal constellation. In this experiment the phase noise from real-time 2.5 Gb/s 16-QAM system include two scenarios: (i) short transmission 20 km SMF and (ii) long distance transmission with 100 km SMF. High launched optical power is applied in both experiments [100]. The optical transmission system with coherent detection and optical amplification is limited by amplifier noise, where ASE noise is the dominant noise component. The ASE noise is responsible for energy fluctuations which make the decision between zero and one level difficult. Also it reduces the signal to noise ratio at the receiver. Dependencies on fiber launch power were analyzed for two different receiver input power values. The intensity patterns were recorded at the receiver input after 20 and 100 km SMF as shown in Figure 5.21.

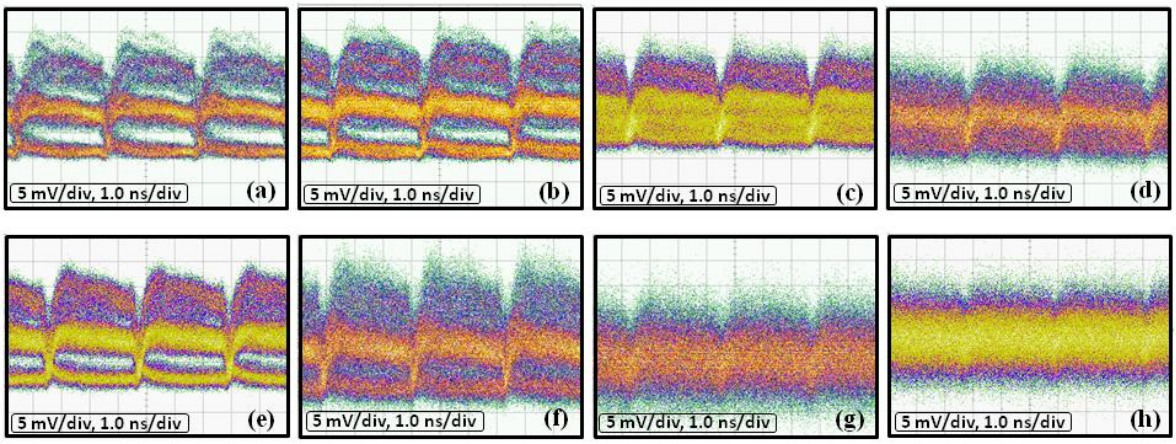

Figure 5.21: 16-QAM intensity eye diagram for $\Delta f \cdot T = 0.00048$ and after 20 km (top) or 100 km (bottom) of SMF for: TX = – 2 dBm, RX = – 20 dBm (a); TX = – 2 dBm, RX = – 30 dBm (b); TX = – 10 dBm, RX = – 20 dBm (c); TX = – 10 dBm, RX = – 30 dBm (d); TX = – 2 dBm, RX = – 20 dBm (e); TX = – 2 dBm, RX = – 30 dBm (f); TX = – 10 dBm, RX = – 20 dBm (g) and TX = – 10 dBm, RX = – 30 dBm (h) input power.

Figure 5.22 shows the received constellation maps of 16-QAM with self-homodyne detection after optical transmission for – 2 dBm and – 10 dBm fiber launch power and – 20 dBm and – 30 dBm received preamplifier input power.

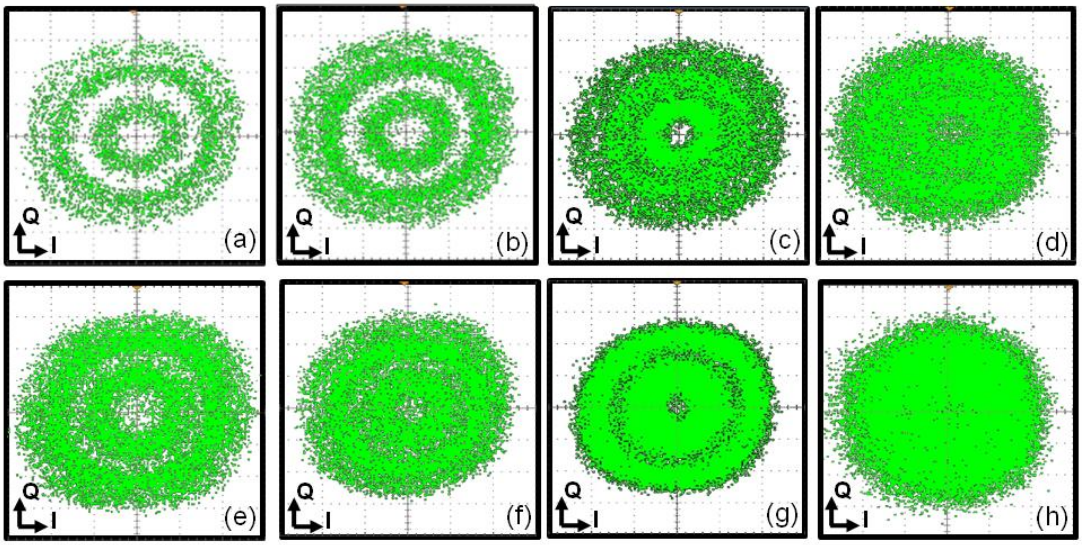

Figure 5.22: 16-QAM constellation maps for $\Delta f \cdot T = 0.00048$ and after 20 km (top) or 100 km (bottom) of SMF for: TX =– 2 dBm, RX = – 20 dBm (a); TX =– 2 dBm, RX =– 30 dBm (b); TX =– 10 dBm, RX =– 20 dBm (c); TX =– 10 dBm, RX =– 30 dBm (d); TX =– 2 dBm, RX =– 20 dBm (e); TX =– 2 dBm, RX =– 30 dBm (f); TX =– 10 dBm, RX =– 20 dBm (g) and TX =– 10 dBm, RX =– 30 dBm (h) input power. Self-homodyne experiment

Figure 5.23 shows the constellation maps of the received 16-QAM signals after optical transmission for heterodyne experiment over 20 and 100 km of SMF at a SNR of 35 dB.

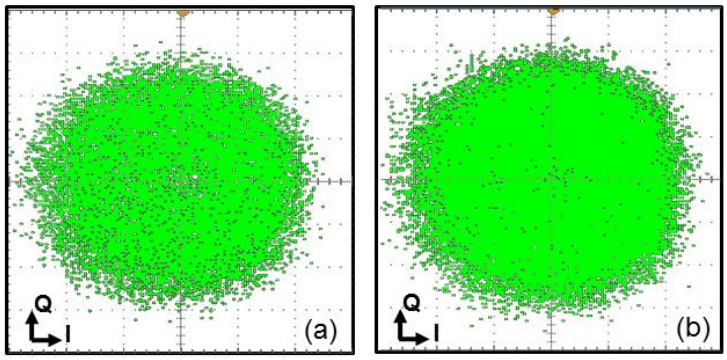

Figure 5.23: 16-QAM constellation for heterodyne experiment after 20 km (a) and 100 km (b).

Figure 5.24 depicts the influence of transmission phase noise for for BPS with ($B = 16$ and $N = 6$) versus QPSKP with ($B = 32$ and $N = 9$) by using a self-homodyne with direct clock and a heterodyne with clock recovery configrations, it shows the Q-factor versus the launched power for various transmission lengths. A similar performance for both CPE algorithms with RX= -20 dBm preamplifier input power can be observed for both transmission distances, while for RX = -30 dBm the QPSKP shows a penalty of about

1 dB comparing to the BPS. Optimal fiber input power was located till − 6 dBm for different fiber lengths.

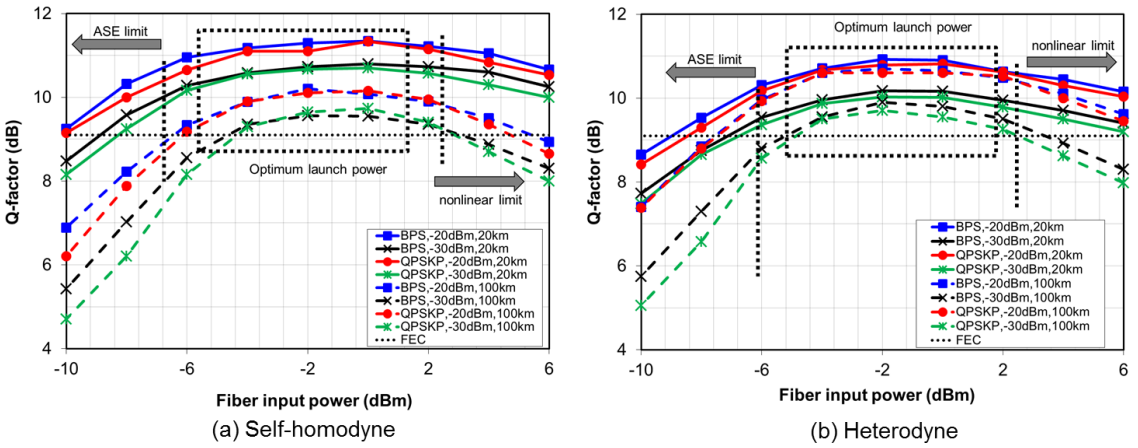

Figure 5.24: Q-factor vs. Fiber input power for different received preamplifier input power and CPE algorithms, using $2^7 - 1$ PRBS data with self-homodyne (a) and heterodyne (b) detections.

The Q-factor has a small change for launched powers from − 6 to 0 dBm despite the variation of the received OSNR. This is because the system performance is limited by imperfection of the electrical components. For launch powers higher than 0 dBm the phase drift increases and the Q-factor decreases. The difference between BPS and QPSKP Q-factors is obvious but both show the same tendency. It is apparent that the transmission system is corrupted by AWGN when the launch power is less than − 8 dBm and − 6 dBm for 20 and 100 km SMF, respectively. During fiber propagation, an optical signal is distorted by an intensity dependent SPM induced nonlinear phase shift. The symbols of 16-QAM have different intensity levels. Therfore, the intensity dependent nonlinear phase shift causes a strong deformation of the received 16-QAM signal constellation. The effect of SPM is not shown so clear for high launch power because it is difficult to obtain a meaningful BER at this transmission distance. In Figure 5.24, the optimum launch power is about 0 dBm for 20 km SMF with negligible fiber nonlinearity. In 100 km long-haul transmission, the launch power into the SMF is − 2 dBm. Even when 10 dB of attenuation is added to the received signal, the optimal launch power is still the same. By comparing BPS with QPSKP carrier phase estimation, the Q-factor of QPSKP is considerably reduced. QPSKP demonstrates worst phase noise tolerance than BPS, this is because QPSKP is more sensitive to ASE-based fluctuation in the amplitude. Although the QPSKP method is slightly simpler, its performance is noticeably worse than BPS

technique. It is observed that QPSKP is strongly affected by SPM induced mean nonlinear phase shifts from Q-factor plot for received data after 100 km, shown on the right side.

5.2.5 BPS angle resolutions effect

As real-time realization of DSP for coherent systems has become an important topic [102], feed-forward carrier recovery algorithm for M-QAM system offered in [28], where authers demonstrate the minimum distance estimator (MDE) which provides sufficient performance for M-QAM with laser linewidths [83]. The proposed scheme which was later named BPS in optical communication literature, achieves the best phase noise tolerance but comes with an expense of hardware effort [28]. This problem had relieved by reducing number of test phase angles to 16. This number is a crucial quantity for BPS algorithm. If the required resolution is too large (i.e. more than 32), the hardware effort will become unfeasible.

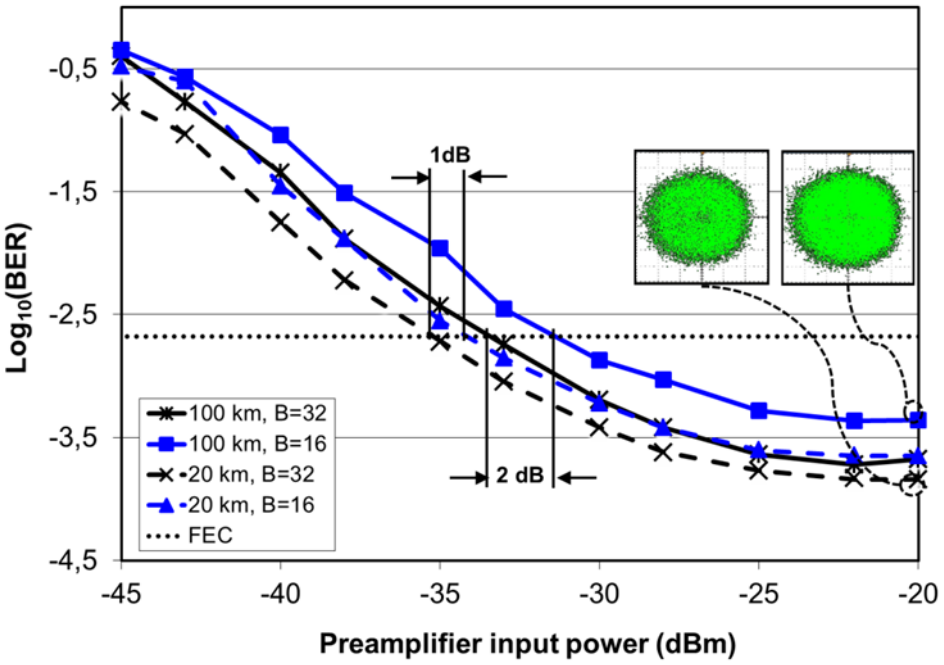

Figure 5.25: Measured BER vs. optical power at the preamplifier input, for different B.

Figure 5.25 shows the influence of 16 and 32 test phase angles on the receiver sensitivity [90]. The test of the system was conducted with $2^7 - 1$ PRBS data as a hetrodyne experiment at data rate of 2.5 Gb/s. The large test phase angle with $B = 32$ yields a better system performance with a BER floor of $1.45 \cdot 10^{-4}$ and a sensitivity of -35.5 dBm for a BER below the threshold of a state-of-the-art FEC (7% overhead) for 20 km SMF. The receiver with $B = 16$ achieves a BER floor $2.25 \cdot 10^{-4}$ and a sensitivity of -34.5 dBm. The BER floors for 100 km distance are $1.9 \cdot 10^{-4}$ and $4.3 \cdot 10^{-4}$ for $B = 32$ and

$B = 16$, respectively. Due to the high laser-sum-linewidth-times-symbol-interval-product $\Delta f \cdot T = 0.00048$, the large test phase angle with $B = 32$ now outperforms the smaller number of test phase angle with $B = 16$ by 1 dB in terms of receiver sensitivity for 20 km and 2 dB for 100 km of fiber length. These results underline the excellent robustness of BPS with 32 test carrier phase angles in the square 16-QAM modulation format. In general, an acceptable BER floor can be seen for $B = 16$ for high laser-sum-linewidth-times-symbol-interval-product and high phase noise. Increasing number of test phase angle causes an improvement but at a price of hardware effort.

5.2.6 External quantization limit by ADC resolution

In these experiments [103] and [90], BPS with ($N = 6$, $B = 16$) versus QPSKP with ($N = 9$ and 6, $B = 32$) have been tested and compared with each other to investigate the influence of ADCs, which is a challenge in real-time coherent transmission systems. The system is tested firstly by using self-homodyne detection with direct clock and later by using heterodyne detection with clock recovery, as shown in Figure 5.9. Transmission distance was over 20 km of SMF. To determine the influence of quantization noise induced by the ADCs all measurements are performed for 4, 5 and 6 bit data converters at the symbol rate of 625 MHz. Figure 5.26 shows the Q-factor dependence on fiber input power for different ADC resolutions.

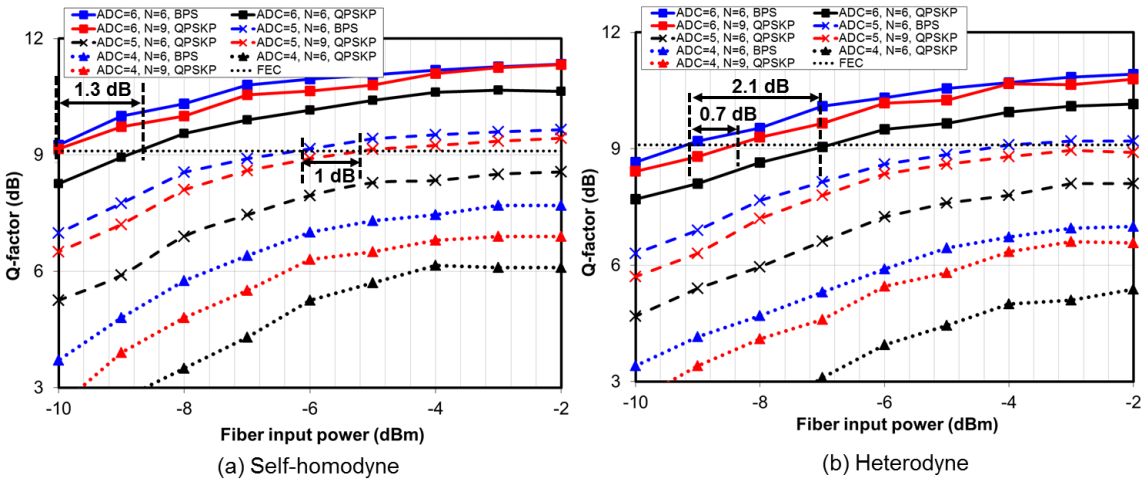

Figure 5.26: Q-factor vs. fiber input power for different ADC resolutions and two carrier-phase-estimation schemes, with self-homodyne (a) and heterodyne (b) detections.

For self-homodyne experiment a similar performance for BPS and QPSKP with a filter half-width of $N = 9$ can be observed for 6 bit ADC resolution, whereas it shows a penalty of 1 dB for 5 bit ADC resolution. For QPSKP with $N = 6$ and 6 bit ADC resolution it

shows a penalty of 1.3 dB and it is lower than the Q-factor limit for 5 bit ADC resolution. An ADC resolution of > 4 bit will be a good choice for $\Delta f \cdot T = 0.00048$. This experiment showed that QPSKP with $N = 9$ and $B = 32$ is comparable to BPS with $N = 6$ and $B = 16$ over 20 km SMF. In heterodyne experiment and 6 bit ADC resolution, the QPSKP technique shows a penalty of 0.7 dB and 2.1 dB for $N = 9$ and 6, respectively. For 5 bit ADC resolution, the Q-factor of BPS at fiber input power of -4 dBm were higher than the Q-limit of 9.1 dB (dotted line) yielding BERs below FEC limit (7% overhead) while QPSKP are below the Q-limit for both $N = 9$ and 6.

Figure 5.27 shows the Q-factor dependence on fiber input power over 100 km of optical transmission for different ADC resolutions, and using BPS with 16 and 32 test carrier phase angles. Up to -20 dBm received preamplifier input power a 0.5 dB performance penalty between $B = 32$ and $B = 16$ can be observed for 6 bit ADC resolutions, while the penalty is increased for decreased ADC resolution.

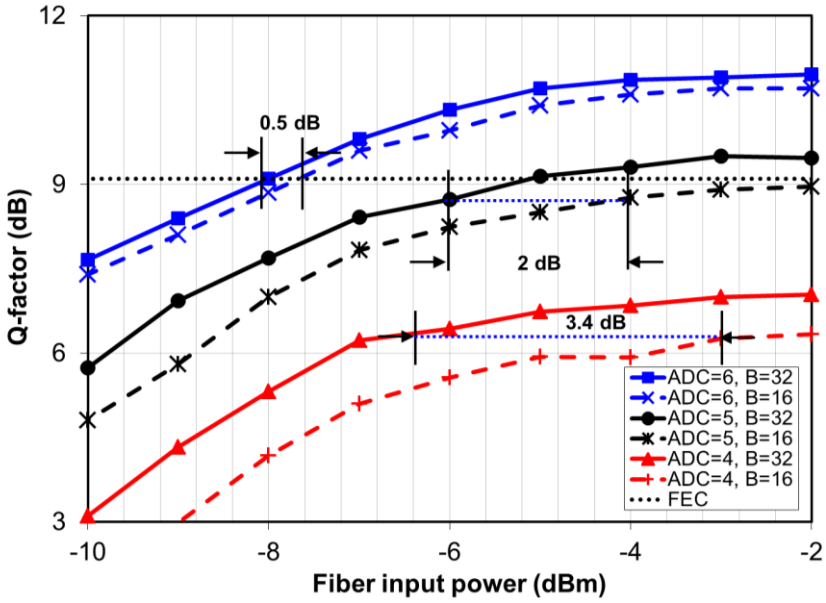

Figure 5.27: Q-factor vs. fiber input power for different ADC resolutions and BPS with different test phase angle numbers and with heterodyne detection.

Chapter 6:

Results discussion and summary

6.1 Discussion

Cost pressure and increasing optical bandwidth usage make it necessary to maximize both the transmitted symbol rate per optical channel and the spectral efficiency, while leaving the deployed fiber infrastructure unchanged. In the recent years QPSK was the preferred modulation format because of its robustness in long-haul links. However, for metropolitan area networks, higher-order quadrature amplitude modulation is permissible namely 16-QAM, which doubles spectral efficiency. Till the beginning of 2012, the experimental results with true real-time measurement setups were still rare to find due to the high complexity in the implementation of real-time coherent receivers, offline DSP was used in many experiments. It is a very useful way to investigate efficient algorithms without the need to do extensive hardware development. FPGAs enable evaluating digital receiver algorithms in real-time experiments before being implemented as CMOS circuits. The flexibility provided by FPGA implementation to develop and test signal processing algorithms in real-time comes at the expense of a reduced bit rate.

The research work described in this thesis investigates phase noise tolerant feed-forward carrier recovery algorithms (BPS and QPSKP) which become most important for the implementation of 16-QAM modulation format. The presented experiments demonstrate for the first time the real-time implementation of a synchronous 16-QAM transmission system with a digital receiver for clock, carrier and data recovery. 2.5 Gb/s (625 Mbaud) 16-QAM data have been transmitted over 20 and 100 km of SMF by a self-homodyne and heterodyne configurations. The influence of ADC, laser linewidth and phase noise which is a challenge in real-time coherent transmission systems was investigated and presented for the two basic recovery techniques. Moreover, different operation points of a 16-QAM modulator have been tested in real-time and an optimal condition is found to minimize the BER. The implemented carrier recovery algorithm is compatible with all kinds of equalizers proposed for polarization control, chromatic dispersion and polarization mode dispersion compensation.

6.2 Summary

16-QAM is the format most likely to complement or replace QPSK as the next step to high-order-formats with increased information content per symbol. For all higher constellations, the phase noise problem becomes sharply increased in comparison to QPSK. Based on this a real-time heterodyne and self-homodyne detections were presented in this research work. To this purpose, a phase-noise-tolerant, hardware-efficient feed-forward carrier recovery was implemented. The influence of linear and nonlinear effects related to the IQ-modulator of a 16-QAM coherent transmission system has been shown. The amplitudes of the MZM in the IQ-modulator need to be carefully adjusted to obtain a good pattern and to avoid phase distortions. The electrical driving voltage of the IQ-modulator were investigated in a real-time transmission and optimized to minimize the required OSNR. Two non-ideal IQ-modulators with different extinction ratio have been tested and found that optimal operating conditions are almost independent of the extinction ratio. 16-QAM signal is prone to the extinction ratio of the modulator especially in the case of low transmitted and received power. Two techniques of carrier phase estimation have been tested and the performances are presented and compared. The QPSKP phase estimator scheme require less computational effort in comparison to BPS, but it is more sensitive against ASE noise effects, especially for higher order QAM constellations. Different filter lengths (half-width N), test carrier phase angles, and ADC resolution have been investigated. For the BPS phase estimator scheme, $N \geq 6$ will be a fairly good choice for $\Delta f \cdot T = 0.00048$, while for the QPSKP scheme filter with $N = 9$ allows to reach a lower BER floor than the filter with $N = 15$ for 100 km of SMF. In addition, implementation of QPSKP with $N = 6$ is not efficient for $\Delta f \cdot T = 0.00048$. Furthermore, an ADC resolution > 4 bit is a good choice for $\Delta f \cdot T = 0.00048$. These results underline the excellent robustness of BPS with 32 test carrier phase angles, and an acceptable BER floor can be seen for 16 for $\Delta f \cdot T = 0.00048$ and for high phase noise. Increasing the number of test phase angles would cause an improvement but at the price of hardware effort. This dissertation has particularly shown that a BER floor was observed below the threshold of a state-of-the-art FEC (7% overhead). Also it showed a successful 16-QAM transmission system in real-time with FPGA-based coherent receiver processing 100% of data.

Appendix : 16-QAM optical transmitter

There are several possible transmitter configurations for square 16-QAM. These methods can be categorized according to electrical driving signals to the optical modulator: i) electrical multilevel drive signals and ii) electrical binary drive signals. The next subsections illustrate different optical square 16-QAM transmitter options.

7.1 Electrical multilevel drive signals

For electrical multilevel drive signals three different transmitter configurations can be used to generate square 16-QAM.

7.1.1 Single dual-drive MZM

One way to generate any arbitrary quadrature signals with multilevel electrical driving signals is to use one dual-drive modulator [104]. This paper proved that that any arbitrary quadrature signals can be generated using one dual-drive modulator. Figure 7.1 shows a basic structure of a dual-drive MZM (DDMZM). The modulator consists of two independent phase modulators. The constellation points of 16-QAM can be generated based on these modulators. These types of linear amplification using nonlinear components (LINC) transmitters are very popular in wireless communications [105].

$$E_{out} = \frac{E_{in}}{2}\left[e^{j\pi\frac{V_1}{V_\pi}} + e^{j\pi\frac{V_2}{V_\pi}}\right] \tag{7.1}$$

V_π is the voltage to provide a π phase shift of each phase modulator. The MZM can operate as a phase modulator for $V_1 = V_2$. So, any quadrature signals can be generated by choosing V_1 and V_2 properly. The normalized form of input and output relationship of (equation 7.1)

$$E_{out} = \frac{r_{max}}{2}\left[e^{j\varphi_1} + e^{j\varphi_2}\right] \tag{7.2}$$

where $\varphi_1 = \pi\frac{V_1}{V_\pi}$ and $\varphi_2 = \pi\frac{V_2}{V_\pi}$. The difference between the two vectors in the circle have a radius of $(1/2)r_{max}$ and the output electric field is E_{out} . The M-ary signal constellation can be represented as complex numbers of

$$s_i = r_i e^{j\theta_i}, \quad r_i > 0, \quad 0 \le \theta_i \le 2\pi, \quad i = 0, \dots, M-1 \tag{7.3}$$

The maximum amplitude is $r_{max} = max\{r_0, r_1, \dots, r_{M-1}\}$ and the two phases of [106] are

$$\varphi_{i1} = \theta_i + \cos^{-1}\left(\frac{r_i}{r_{max}}\right) \tag{7.4}$$

and

$$\varphi_{i2} = \theta_i - \cos^{-1}\left(\frac{r_i}{r_{max}}\right) + \pi. \tag{7.5}$$

Figure 7.1 shows the corresponding phases φ_{i1} and φ_{i2} of all 16 points according to the separation of 16-QAM constellation. Instead of representing all 16 constellation points in the same figure, Figure 7.1 separates the 16-QAM signal into two QPSK and one 8-PSK signals. From Figure 7.1, the generation of a 16-QAM signal using a dual-drive MZM requires a 16-ary driving signals and thus a big electrical effort to enable the simplicity of the optical part.

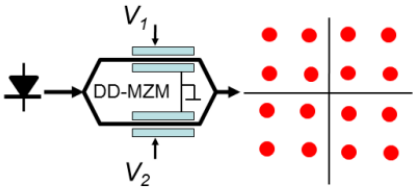

Figure 7.1: Square 16-QAM transmitter using single DDMZM.

7.1.2 Serial configuration

Another transmitter configuration with only two consecutive optical modulators capable to generate any QAM constellation is shown in Figure 7.2. This coherent optical transmitter is called serial configuration [45].

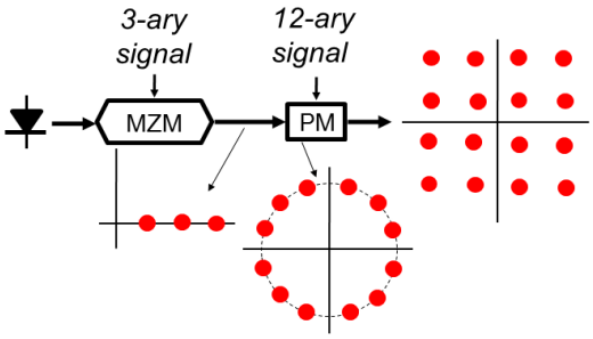

Figure 7.2: Serial square 16-QAM transmitter contains a MZM and a PM in series.

The MZM is used to adjust the amplitude and the PM to set the phase. This modulator has a simple optical part but necessitates very complicated drive circuits for the electrical part, since 3 amplitude levels and 12 electrical driving signals are needed for the phase

modulation for 16-QAM. Again the complexity to generate multilevel driving signals is one of the difficulties for practical implementation especially for high data rates. Therefore, this type of transmitter is not helpful for square 16-QAM.

7.1.3 Pure IQ transmitters

To reduce the complexity of electrical driving circuits a pure IQ transmitter (or conventional IQ setup) can be used, where number of electrical states of the driving signals is much lower as shown in Figure 7.3. In [45], it was shown that in pure IQ transmitters there will be symbol transitions through zero in the constellation diagram. If we consider chirp, the best transmission setup will be a conventional IQ transmitter, where chirp and normalized intensity is comparatively small. The chirp characteristics of the other transmitters are more disadvantageous because chirp appears simultaneously with high power levels. For that reason the common IQ transmitter is used here.

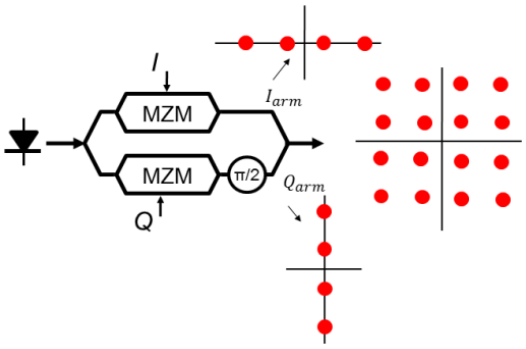

Figure 7.3: Conventional IQ setup.

7.2 Electrical binary drive signals

To generate square 16-QAM with electrical binary drive signals, a combination of multiple optical modulators can be used.

7.2.1 Monolithically integrated IQ-modulator

A 16-QAM transmitter using a monolithically integrated IQ-modulator was tested by [45, 107]. Figure 7.4 shows that the optical 16-QAM signal could be synthesized by addition of two mutually orthogonal and independent signals encoded as four-level amplitude-shift keying (4-ASK). The monolithically integrated IQ-modulator consists of four sub-MZMs arranged within an IQ superstructure [107], where each arm contains two sub-MZMs which are cascaded in series, cf. Figure 7.4 (right). Another option is by replacing one MZM in each arm with a PM [45] cf. Figure 7.4 (left). The two streams will be combined

by quadrature addition of the optical fields to generate a 16-QAM signal. The monolithically integrated IQ-modulator has a simple bias control, stable performance, and is easy to fabricate.

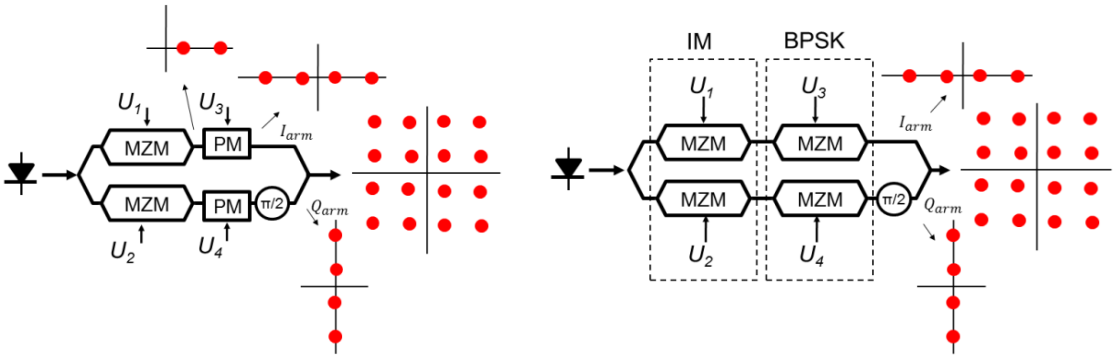

Figure 7.4: IQ-setup with MZM and PM (left), quad mach-zehnder IQ modulator (right).

7.2.2 IQ-modulator with PM in serial setup

The diagram of this scheme is shown in Figure 7.5, which consists of a DPMZM followed by a PM [108]. The structure of the transmitter can be divided into two stages. In the first stage, both sub-MZMs of the DPMZM are biased at a quadrature point and driven by U_1 and U_2 with the same amplitude to generate two 2ASK signals with equal ER. By adjusting the bias of main MZM, the two ASK signals achieve a 90° phase difference and are then combined to obtain an offset QPSK signal with its origin biased in the first quadrant, as shown in Figure 7.5. In the second stage, the generated offset QPSK signal is further QPSK modulated by a PM, which is driven by a 4-level electrical signal to realize square 16-QAM signal.

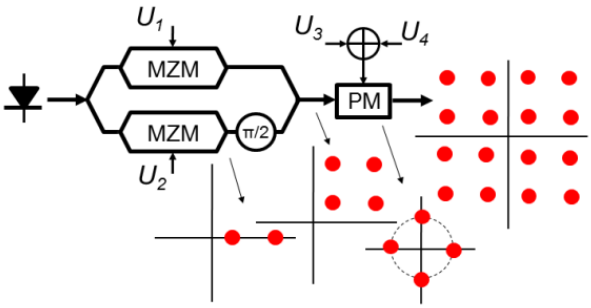

Figure 7.5: Serial square 16-QAM transmitter, DPMZM and PM in series.

7.2.3 Triple cascaded modulators

Another transmitter also requiring electrical binary drive signals to generate square 16-QAM is shown in Figure 7.6. By this scheme, three cascaded modulators are used [109–

111]. The MZMs within the IQ-modulator achieve a modulation within the first quadrant, while the two consecutive PMs apply phase shifts of π and $\pi/2$, respectively. The driving voltages for the three cascaded modulators can be optimized to reduce the influence of the modulation bandwidth limitation. In [109], it was shown that this scheme shows more inter-symbol interference comparing to single-IQ-modulators. It also indicates that the discrete transmitter schemes, especially the triple cascaded transmitter, are more sensitive to bandwidth limitations of the electronics. One benefit of this transmitter is the possibility of inserting an amplifier in-between the stages.

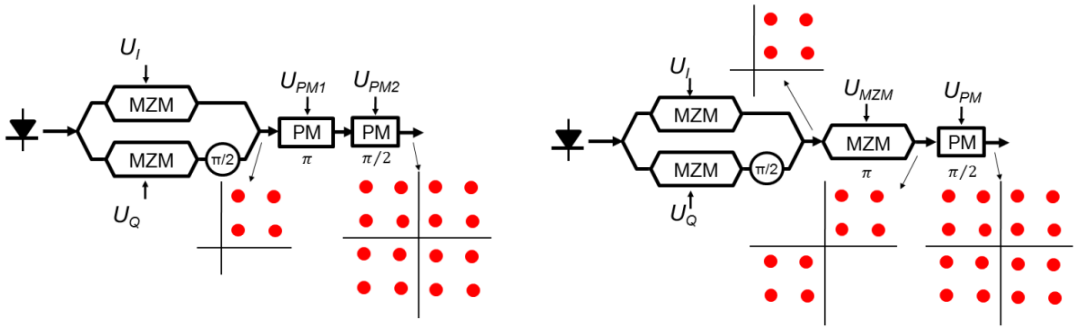

Figure 7.6: IO-modulator followed by: two consecutive PMs (left), MZM and PM(right).

7.2.4 Serial combination of DDMZM and DPMZM

This transmitter scheme is based on a combination of a DDMZM and a DPMZM with electrical binary drive signals, as depicted in Figure 7.7. The two arms of DDMZM are independently driven by two different binary data, and consequently, the DDMZM produces an offset square 4-QAM of the 16-QAM constellation. This 4-QAM signal is then switched over the other quadrants by a typical QPSK modulation scheme using the following DPMZM, resulting in 16-QAM [112]. Each modulator is driven by electrical binary data ($U_1 \sim U_4$) where $v_1(t) \sim v_4(t)$ denote the binary data values between 0.5 and -0.5, and $a_1 \sim a_4$ represent their amplitudes. 4-QAM can be yielded in the first quadrant if the DDMZM driven with $a_1 = a_2 = 0.3V_\pi$, cf. Figure 7.7(bottom). Another solution to drive DDMZM by $a_1 = a_2 = 0.7V_\pi$, cf. Figure 7.7(top). In both cases the bias voltage of DDMZM is equal to $0.5V_\pi$. This technique has a frequency chirp induced by DDMZM, but this impact can be removed if we use RZ pulse carving [112].

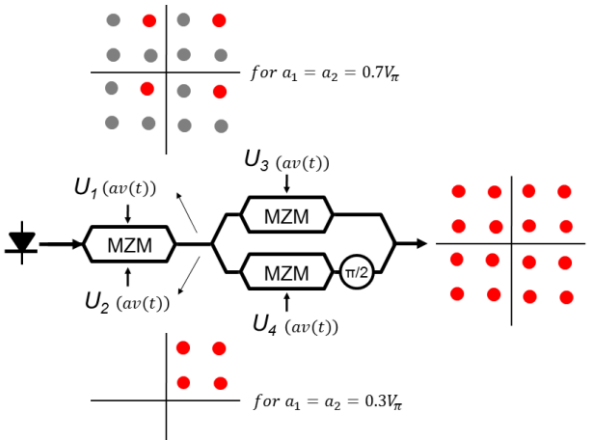

Figure 7.7: Serial combination of DDMZM and DPMZM.

7.2.5 Two cascaded IQ-modulators

A 16-QAM optical signal can be generated by two cascade IQ-modulators, driven by four separate binary electrical signals [109, 113]. A general scheme for the transmitter is shown in Figure 7.8. The two cascaded IQ-modulators are cascaded without any relative phase-stability control. Each IQ-modulator has a nested MZM structure, with an MZM on each arm. Each MZM is operated in push-pull and is designed to have zero chirps.

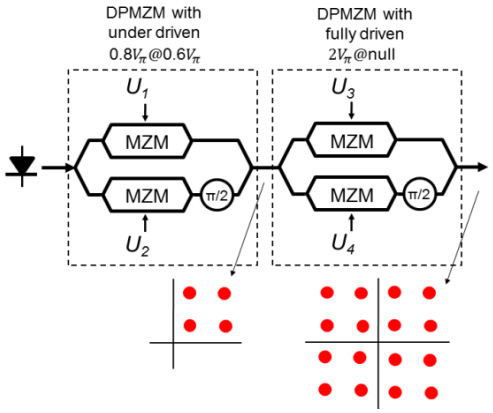

Figure 7.8: Two cascade IQ-modulators.

The transmitter adopts quadrant differential encoding and employs only two-level electrical driving signals. The input sequence of binary data at a bit-rate of Rb is converted to four binary sequences at $Rb/4$, and these are subsequently encoded to obtain the four binary sequences to form the sequence of symbols to be transmitted out of the 16-QAM constellation. This optical modulation scheme is effective for the implementation of quadrant differential encoding; also it has some other interesting characteristics. The two cascaded IQ-modulators are completely independent, meaning that they can be either integrated on a single chip or separated since relative phase stability between them is not

required. This scheme has more inter-symbol interference comparing to single IQ-modulator [109].

7.2.6 Conventional dual-drive IQ-MZM

This 16-QAM optical transmitter can be categorized into two types. In the first type, each DDMZM in the optical modulator is driven by two binary electrical signals with different amplitudes [114] as shown in Figure 7.9(left). To generate square 16-QAM, four equidistant and collinear signal points should be generated in parallel with the axis both in the I and Q arm. The MZM operate in push-pull mode and are biased at the null point. Figure 7.9(right) shows the second type, where an unbalanced power splitting ratio of each input coupler of the two MZMs (one placed on the I arm, the other placed on the Q arm) is optimized to allow for offset-free 16-QAM generation from four equal amplitude binary signals [115]. Four equal amplitude binary signals are applied to generate a square 16-QAM constellation. The structure is similar to the first type, but with a fundamental difference in the design: The splitter of the first and the second DDMZM is designed to be unbalanced, with a power-splitting ratio equal to $80/20$, corresponding to an amplitude ratio of 2. Due to the unbalanced splitter, the optical field propagating in the first arm will be twice in amplitude with respect to the optical field propagating in the second arm. Later, I and Q arms will produce a four-level amplitude and PSK (4-APSK) constellation.

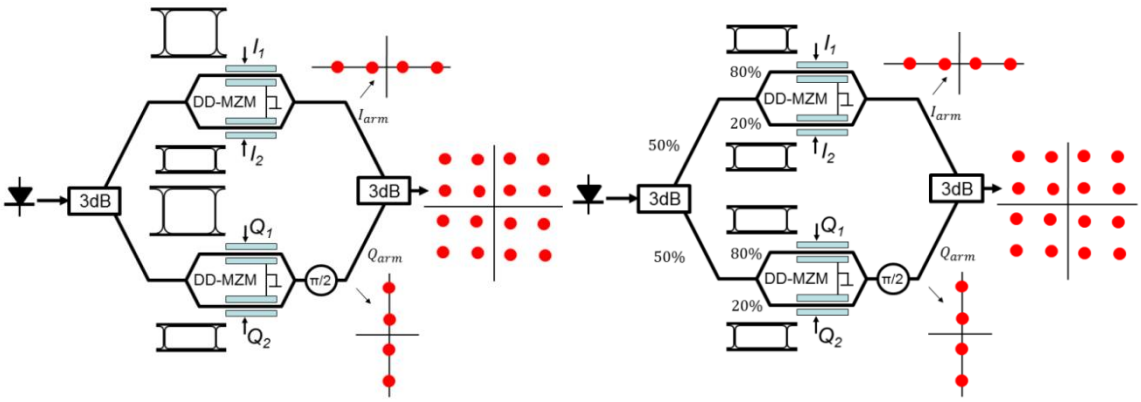

Figure 7.9: Single dual-drive IQ-modulator.

7.2.7 Quad-parallel MZM setup

Another transmitter also requiring electrical binary drive signals for square 16-QAM is denoted as quad-parallel MZM transmitter [116, 46]. Square 16-QAM can be realized from two QPSK signals with different amplitude, as shown in Figure 7.10. The large amplitude QPSK determines the quadrant where the symbol is mapped, while the small-amplitude

QPSK fixes the position of the mapping within the quadrant. After combining the QPSK signals, the output of the 3 dB coupler shows totally 16 symbols which are mapped with equal spacing in a constellation map. The authors in [109] investigate between three types of modulators which use electrical binary drive signals: the quad-parallel MZM, the two cascade IQ-modulators and the three cascade modulators. They compared the constellation diagrams of these schemes and show that the quad-parallel MZM transmitter has the best performance, and the largest penalty was observed for the case of the triple-cascaded modulators scheme. Also they show that the constellation with two cascaded IQ-modulators has worse performance than the quad-parallel MZM setup, but on the other hand, it outperforms the triple-cascaded modulators scheme, regarding tolerance to modulation bandwidth limitations and chromatic dispersion.

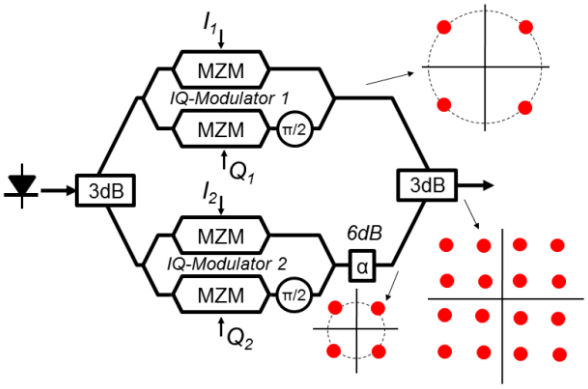

Figure 7.10: Quad-parallel MZM setup.

7.2.8 Simple optical signal generator

In this simple scheme, a delay interferometers (DI) is used to generate square 16-QAM, as shown in Figure 7.11. Firstly, the IQ-modulator is used to generate DQPSK, and then the signal is launched into a 2×2 DI, which consists of two 2×2 couplers, a phase shifter and a delay line [117]. The power splitting ratios of the first and second coupler of 2×2 DI are adjusted to $1:4$ (amplitude ratio of the optical signals in upper and lower arm becoming $1:2$) and $1:1$, respectively. The optical signal in the upper arm is introduced a $\pi/2$ phase shift, while the optical signal in the lower arm is delayed for 5 bits. A 16-QAM signal is yielded after the second coupler.

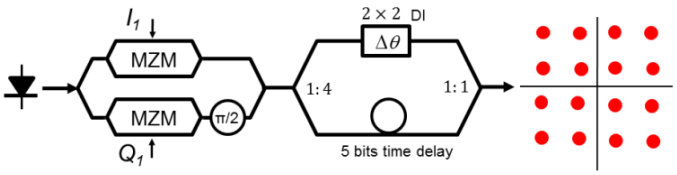

Figure 7.11: Square 16-QAM transmitter.

Bibliography

[1] N. Antoniades, G. Ellinas and L. Roudas, WDM Systems and Networks, Springer, 2012.

[2] J.L. Beylat, "How will optical networks continue to transform the way the world communicates?," in *Asia-Pacific Optical Communication (APOC), Plenary Presentation*, 2007.

[3] M. Nakazawa, K. Kikuchi, T. Miyazaki, High Spectral Density Optical Communication Technologies, Springer, 2010.

[4] P.J. Winzer, "Information Theory and Digital Signal Processing in Optical Communications," in *IEEE CTW*, Barcelona, Spain, 2011.

[5] R.W. Tkach, "Scaling optical communications for the next decade and beyond," *Bell Labs Technical Journal*, vol. 14, no. 4, pp. 3-9, 2010.

[6] "The Digital Universe," EMC-sponsored study by IDC, [Online]. Available: http://www.emc.com/leadership/digital-universe/index.htm.

[7] J. Gray, P. Shenoy, "Rules of Thumb in Data Engineering," in *Proc. 16th International Conference on Data Engineering*, 2000.

[8] R.W. Tkach, "Network Traffic and System Capacity: Scaling for the Future," in *Proc. 36th European Conference and Exhibition on Optical Communication (ECOC)*, 2010.

[9] "Top 500 Supercomputers," [Online]. Available: http://www.top500.org/lists/.

[10] P.J. Winzrer, "OPTICAL NETWORKING BEYOND WDM," *IEEE Photonics Journal*, vol. 4, no. 2, pp. 647-651, 2012.

[11] P.J. Winzer, G. Raybon, M. Duelk, "107-Gb/s optical ETDM transmitter for 100G Ethernet transport," in *Proc. 31st European Conference on Optical Communication (ECOC)*, 2005.

[12] C.R. Doerr, P.J. Winzer, G. Raybon et al., "A single-chip optical equalizer enabling 107-Gb/s optical non-return-to-zero signal generation," in *Proc. 31st European Conference on Optical Communication (ECOC)*, 2005.

[13] R.H. Derksen, G. Lehmann, C.J. Weiske et al., "Integrated 100 Gbit/s ETDM Receiver in a Transmission Experiment over 480 km DMF," in *Proc. Optical Fiber Communication Conference (OFC/NOFC)*, 2006.

[14] T. Pfau, S. Hoffmann, R. Peveling et al., "Real-time Synchronous QPSK Transmission with Standard DFB Lasers and Digital I&Q Receiver," in *Proc. Coherent Optical Technologies and Applications (COTA) Topical Meeting*, 2006.

[15] T. Pfau, R. Peveling, S. Hoffmann et al., "PDL-Tolerant Real-time Polarization-Multiplexed QPSK Transmission with Digital Coherent Polarization Diversity Receiver," in *Proc. IEEE/LEOS Summer Topical Meetings*, 2007.

[16] C.R.S. Fludger, T. Duthel, D. Van den Borne et al., "Coherent Equalization and POLMUX-RZ-DQPSK for Robust 100-GE Transmission," *Journal of Lightwave Technology*, vol. 26, no. 1, pp. 64-72, 2008.

[17] P. J. Winzer, "Information Theory and Digital Signal Processing in Optical Communications," in *IEEE CTW*, Barcelona, Spain, 2011.

[18] B. Koch, R. Noé, D. Sandel et al., "200-Gb/s, 430-km PDM-RZ-DQPSK (4 Bit/Symbol) Transmission with 10 krad/s Endless Polarization Tracking," in *Proc. OFC/NFOEC* , San Diego, CA, Paper OThD4 , Mar. 21-25, 2010, 2010.

[19] A.H. Gnauck, P.J. Winzer, G. Raybon et al., "10 × 224-Gb/s WDM Transmission of 56-Gbaud PDM-QPSK Signals Over 1890 km of Fiber," *IEEE PHOTONICS TECHNOLOGY LETTERS,* vol. 22, no. 13, pp. 954-956, 2010.

[20] G. Raybon, A.L. Adamiecki, S. Randel et al., "All-ETDM 80-Gbaud (640-Gb/s) PDM 16-QAM Generation and Coherent Detection," *IEEE PHOTONICS TECHNOLOGY LETTERS,* vol. 24, no. 15, pp. 1328-1330, 2012.

[21] X. Zhou, L.E. Nelson, P. Magill et al., "PDM-Nyquist-32QAM for 450-Gb/s Per-Channel WDM Transmission on the 50 GHz ITU-T Grid," *JOURNAL OF LIGHTWAVE TECHNOLOGY,* vol. 30, no. 4, pp. 553-559, 2012.

[22] A.H. Gnauck, P.J. Winzer, A. Konczykowska et al., "Generation and transmission of 21.4-Gbaud PDM 64-QAM using a high-power DAC driving a single I/Q modulator," in *Proc. Optical Fiber Communication Conference and Exposition (OFC/NFOEC)*, 2011.

[23] S. Okamoto, T. Omiya, K. Kasai et al., "140 Gbit/s coherent optical transmission over 150 km with a 10 Gsymbol/s polarization-multiplexed 128 QAM signal," in *Proc. Optical Fiber Communication Conference and Exposition (OFC/NFOEC),* 2010.

[24] M. Nakazawa, S. Okamoto, T. Omiya et al., "256-QAM (64 Gb/s) Coherent Optical Transmission Over 160 km With an Optical Bandwidth of 5.4 GHz," *IEEE PHOTONICS TECHNOLOGY LETTERS,* vol. 22, no. 3, pp. 185-187, 2010.

[25] S. Okamoto, K. Toyoda, T. Omiya et al., "512 QAM (54 Gbit/s) coherent optical transmission over 150 km with an optical bandwidth of 4.1 GHz," in *Proc.36th European Conference and Exhibition on Optical Communication (ECOC)*, 2010.

[26] Ciena Corporation, "http://www.ciena.com/connect/blog/?tag=16QAM," WaveLogic 3, March 6, 2012. [Online].

[27] P.J. Winzer , "Beyond 100G ethernet," *IEEE Communications Magazine,* vol. 48, no. 7, pp. 26-30, 2010.

[28] T. Pfau, S. Hoffmann, R. Noe, "Hardware-Efficient Coherent Digital Receiver Concept With Feedforward Carrier Recovery for -QAM Constellations," *Journal of Lightwave Technology,* vol. 27, no. 8, pp. 989-999, 2009.

[29] R.H. Walden, "Analog-to-digital converter survey and analysis," *IEEE Jornal on Selected Areas in Communications,* vol. 17, no. 4, pp. 539-550, 1999.

[30] R.H. Walden, "Analog-to-Digital Converters and Associated IC Technologies," in *Proc. Compound Semiconductor Integrated Circuits Symposium (CSIC)*, 2008.

[31] J.G. Proakis, Digital Communications, 4th edn., New York: McGraw-Hill, 2000.

[32] F. Xiong, Digital Modulation Techniques, Artech House, Inc., 2000.

[33] K.P. Ho, Phase-Modulated Optical Communication Systems, Springer, 2005.

[34] C.E. Shannon, "A mathematical theory of communication," *The Bell System Technical Journal,* vol. 27, p. 379–423 and 623–656, July, October, 1948.

[35] R.-J. Essiambre, G. Kramer, P.J. Winzer et al., "Capacity Limits of Optical Fiber Networks," *JOURNAL OF LIGHTWAVE TECHNOLOGY,* vol. 28, no. 4, pp. 662-

701, 2010.

[36] C. Campopiano, B. Glazer, "A Coherent Digital Amplitude and Phase Modulation Scheme," *IRE Transactions on Communications Systems,* vol. 10, no. 1, pp. 90-95, 1962.

[37] J.-i. Hashimoto, Y. Nakano, K. Tada, "Influence of facet reflection on the performance of a DFB laser integrated with an optical amplifier/modulator," *IEEE Journal of Quantum Electronics,* vol. 28, no. 3, pp. 594- 603, 1992.

[38] F. Koyama, K. Iga, , "Frequency chirping in external modulators," *Journal of Lightwave Technology,* vol. 6, no. 1, pp. 87-93, 1988.

[39] N. Antoniades, G. Ellinas, L. Roudas, WDM Systems and Networks, Springer, 2012.

[40] E. Patzak, R. Lancenhorst , "Sensitivity degradation of conventional and balanced 3 x 3 port phase diversity DPSK receivers due to thermal and local oscillator intensity noise," *Electronics Letters* , vol. 25, no. 8, pp. 545-547, 1989.

[41] M. Seimetz, "Phase diversity receivers for homodyne detection of optical DQPSK signals," *Journal of Lightwave Technology* , vol. 24, no. 9, pp. 3384-3391, 2006.

[42] VPI systems, Photonic Modules Reference Manual, 2005.

[43] M. Seimetz, High-Order Modulation for Optical Fiber Transmission, Springer, 2009.

[44] Govind P. Agrawal, Fiber-Optic Communication Systems, 4th edition, John Wiley & Sons, Inc., 2010.

[45] M. Seimetz, "Multi-format transmitters for coherent optical M-PSK and M-QAM transmission," in *Proc. ICTON, Th.B1.5*, Barcelona, 2005.

[46] T. Sakamoto, A. Chiba, and T. Kawanishi, "50-km SMF transmission of 50-Gb/s 16 QAM generated by quad-parallel MZM," in *Proc. of European Conference on Optical Communication (ECOC), Tu.1.E.3*, 2008.

[47] R.A. Griffin, A.C. Carter, "Optical differential quadrature phase-shift key (oDQPSK) for high capacity optical transmission," in *Proc. Optical Fiber Communication Conference and Exhibit (OFC)* , 2002.

[48] G. Wenke, M. Klimmek, "Considerations on the α-Factor of Nonideal, External Optical Mach- Zehnder Modulators," *Journal of Optical Communications,* vol. 17, no. 2, p. 42–48, 1996.

[49] A. Al-Bermani, C. Wördehoff, S. Hoffmann et al., "Nonlinear Effect of IQ Modulator in a Realtime Synchronous 16-QAM Transmission System," in *Proc. IEEE Photonics Conference (IPC)*, USA, 2011.

[50] E. Säckinger, "Optical Transmitters," in *Broadband Circuitsfor Optical Fiber Communication*, John Wiley & Sons, Inc., 2005, p. 233.

[51] D.A. Fishman, B.S. Jackson, "Transmitter and receiver design for amplified lightwave systems," in *I.P. Kaminow, T.L. Koch, editors, Optical Fiber Telecommunications IIIB*, San Diego, Academic Press, 1997, p. 69–114.

[52] S.H. Chang, H.S. Chung, K. Kim , "Optimization of Operating Conditions for 112-Gb/s Polarization-Multiplexed 16-QAM Optical Modulation," *IEEE Photonics Technology Letters,* vol. 23, no. 11, pp. 724- 726, 2011.

[53] T. Kawanishi, T. Sakamoto, A. Chiba, M. Izutsu, "Study of precise optical modulation using Mach-Zehnder interferometers for advanced modulation formats,"

in *Proc. 33rd European Conference and Ehxibition of Optical Communication (ECOC)*, Germany, 2007.

[54] H.S. Chung, S.H. Chang, K. Kim, "Mitigation of Imperfect Carver-Induced Phase Distortions in a Coherent PM-RZ-QPSK Receiver," *Journal of Lightwave Technology,* vol. 28, no. 24, pp. 3506-3511 , 2010.

[55] T. Okoshi, "Recent advances in coherent optical fiber communication systems," *Journal of Lightwave Technology* , vol. 5, no. 1, pp. 44-52, 1987.

[56] R.A. Linke, A.H. Gnauck, "High-capacity coherent lightwave systems," *Journal of Lightwave Technology,* vol. 6, no. 11, pp. 1750-1769 , 1988.

[57] T. Okoshi, K. Kikuchi, coherent optical fiber communications, Springer, 1988.

[58] M. Seimetz, C.M. Weinert, "Options, Feasibility, and Availability of 2 × 4 90º Hybrids for Coherent Optical Systems," *Journal of Lightwave Technology,* vol. 24, no. 3, pp. 1317-1322, 2006.

[59] D. Hoffman, H. Heidrich, G. Wenke et al. , "Integrated Optics Eight-Port 90º Hybrid on LiNbO3," *Lightwave Technology, Journal of* , vol. 7, no. 5, pp. 794-798 , 1989.

[60] CeLight, "http://www.celight.com," CL-CR-10, January 2007. [Online].

[61] A. Kaplan, K. Achiam, "LiNbO3 integrated optical QPSK modulator and coherent receiver," in *Proc. ECIO*, 2003.

[62] S.J. Savory, G. Gavioli, R.I. Killey, P. Bayvel, "Transmission of 42.8Gbit/s Polarization Multiplexed NRZ-QPSK over 6400km of Standard Fiber with no Optical Dispersion Compensation," in *Proc. Optical Fiber Communication and the National Fiber Optic Engineers Conference (OFC/NFOEC)*, 2007.

[63] T. Pfau, R. Peveling, J. Hauden et al., "Coherent Digital Polarization Diversity Receiver for Real-Time Polarization-Multiplexed QPSK Transmission at 2.8 Gbit/s," *IEEE Photonics Technology Letters,* vol. 19, no. 24, pp. 1988-1990, 2007.

[64] K. Kikuchi, S. Tsukamoto, "Evaluation of Sensitivity of the Digital Coherent Receiver," *Journal of Lightwave Technology,* vol. 26, no. 13, pp. 1817-1822, 2008.

[65] M.G. Taylor, "Phase Estimation Methods for Optical Coherent Detection Using Digital Signal Processing," *Journal of Lightwave Technology,* vol. 27, no. 7, pp. 901-914, 2009.

[66] T. Pfau, S. Hoffmann, R. Peveling et al., " First Real-Time Data Recovery for Synchronous QPSK Transmission with Standard DFB Lasers," *IEEE Photonics Technology Letters,* vol. 18, pp. 1907-1909, 2006.

[67] I. Dedic, "56Gs/s ADC : Enabling 100GbE," in *Proc. Optical Fiber Communication (OFC/NFOEC)*, 2010.

[68] S.J. Savory, "Digital Coherent Optical Receivers: Algorithms and Subsystems," *IEEE Journal of Selected Topics in Quantum Electronics,* vol. 16, no. 5, pp. 1164-1179, 2010.

[69] S.J. Savory, "Digital filters for coherent optical receivers," *Optics Express,* vol. 16, no. 2, pp. 804-817, 2008.

[70] C.R.S. Fludger, J.C. Geyer, T. Duthel et al., "Real-time prototypes for digital coherent receivers," in *Optical Fiber Communication (OFC/NFOEC)*, 2010.

[71] T. Pfau, R. Peveling, V. Herath et al., "Towards Real-Time Implementation of Coherent Optical Communication," in *Proc. Optical Fiber Communication (OFC/*

NOFC), 2009.

[72] S. Zhang, P.Y. Kam, C.Yu, J. Chen, "Laser Linewidth Tolerance of Decision-Aided Maximum Likelihood Phase Estimation in Coherent Optical M-ary PSK and QAM Systems," *IEEE Photonics Technology Letters* , vol. 21, no. 15, pp. 1075-1077 , 2009.

[73] I. Fatadin, D. Ives, S.J. Savory, "Laser Linewidth Tolerance for 16-QAM Coherent Optical Systems using QPSK Partitioning," *IEEE Photonics Technology Letters,* vol. 22, no. 9, pp. 631-633, 2010.

[74] M. Seimetz, "Laser Linewidth Limitations for Optical Systems with High-Order Modulation Employing Feed Forward Digital Carrier Phase Estimation," in *Proc. Optical Fiber communication/National Fiber Optic Engineers Conference (OFC/NFOEC)*, 2008.

[75] E. Ip, J.M. Kahn, "Feedforward Carrier Recovery for Coherent Optical Communications," *Journal of Lightwave Technology,* vol. 25, no. 9, pp. 2675-2692 , 2007.

[76] S. Hoffmann, T. Pfau, O. Adamczyk et al., "Frequency Estimation and Compensation for Coherent QPSK Transmission with DFB Lasers," in *Proc. Coherent Optical Technologies and Applications (COTA), Optical Society of America,* 2008.

[77] S. Hoffmann, T. Pfau, O. Adamczyk et al., "Hardware-Efficient and Phase Noise Tolerant Digital Synchronous QPSK Receiver Concept," in *Proc. Coherent Optical Technologies and Applications (COTA), Optical Society of America*, 2006.

[78] A.J. Viterbi, A.M. Viterbi, "Nonlinear estimation of PSK modulated carrier phase with application to burst digital transmission," *IEEE Transactions on Information Theory,* vol. 29, no. 4, pp. 543-551, 1983.

[79] S. Hoffmann, R. Peveling, T. Pfau et al., "Multiplier-free Realtime Phase Tracking for Coherent QPSK Receivers," *IEEE Photonics Technology Letters,* vol. 21, pp. 137-139, 2009.

[80] N.Wiener, "Extrapolation, Interpolation, and Smoothing of Stationary Time Series.," Cambridge : The MIT Press, 1964.

[81] F. Rice, M. Rice, B. Cowley, "A new algorithm for 16-QAM carrier phase estimation using QPSK partitioning," *Digital Signal Processing*, vol. 12, no. 1, pp. 77-86, 2002.

[82] T. Pfau, R. Noé, "Phase-Noise-Tolerant Two-Stage Carrier Recovery Concept for Higher Order QAM Formats," *IEEE Journal of Selected Topics in Quantum Electronics,* vol. 16, no. 5, pp. 1210-1216, 2010.

[83] X. Zhou, "An Improved Feed-Forward Carrier Recovery Algorithm for Coherent Receivers With M-QAM Modulation Format," *IEEE Photonics Technology Letters,* vol. 22, no. 14, pp. 1051-1053, 2010.

[84] S.K. Oh, S.P. Stapleion, "Blind phase recovery using finite alphabet properties in digital communications," *Electronics Letters,* vol. 33, no. 3, p. 175–176, 1997.

[85] F. Rice, B. Cowley, B. Moran, M. Rice, "Cramér-Rao lower bounds for QAM phase and frequency estimation," *IEEE Transactions on Communications* , vol. 49, no. 9, pp. 1582-1591, 2001.

[86] R. Noé, "PLL-Free Synchronous QPSK Polarization Multiplex/Diversity Receiver Concept with Digital I&Q Baseband Processing," *IEEE Photonics Technology Letters,* vol. 17, no. 4, pp. 887-889, 2005.

[87] W. Weber, "Differential Encoding for Multiple Amplitude and Phase Shift Keying Systems," *IEEE Transactions on Communications* , vol. 26, no. 3, pp. 385-391, 1978.

[88] J. Volder, "The CORDIC Trigonometric Computing Technique," *IRE Transactions on Electronic Computers*, Vols. EC-8, no. 3, pp. 330-334 , 1959.

[89] A. Al-Bermani, C. Wordehoff, S. Hoffmann et al. , "Realtime 16-QAM Transmission with Coherent Digital Receiver," in *Proc. 15th IEEE OptoeElectronics and Communications Conference (OECC)*, 2010.

[90] A. Al-Bermani, C. Wordehoff, O. Jan et al., "Real-time Comparison of Blind Phase Search with Different Angle Resolutions for 16-QAM," in *Proc. IEEE Photonics Conference (IPC)* , 2012.

[91] R. Noé, T. Pfau, M. El-Darawy, "QAM Adaptation of Constant-Modulus Algorithm and Differential Phase Compensation for Polarization Demultiplex in Coherent Receiver," in *Proc. 35th European Conference on Optical Communication (ECOC)*, 2009.

[92] R. Noé, T. Pfau, M. El-Darawy, S. Hoffmann, "Electronic Polarization Control Algorithms for Coherent Optical Transmission," *IEEE Journal of Selected Topics in Quantum Electronics*, vol. 16, no. 5, pp. 1193-1200, 2010.

[93] T. Pfau, R. Peveling, V. Herath et al., " Towards Real-Time Implementation of Coherent Optical Communication," in *Proc. OFC/NFOEC*, invited paper, OThJ4, San Diego, CA, USA, 2009.

[94] A. Al-Bermani, C. Woerdehoff, T. Pfau et al., "First Realtime Synchronous 16-QAM Transmission with Coherent Digital Receiver," in *Proc. ITG Symposium on Photonic Networks* , 2010.

[95] R. Noe, Essentials of Modern Optical Fiber Communication, Springer, 2010.

[96] A. Al-Bermani, C. Wordehoff, S. Hoffmann et al., "Realtime Phase-Noise-Tolerant 2.5 Gbit/s Synchronous 16-QAM Transmission," *IEEE Photonics Technology Letters*, vol. 22, no. 24, pp. 1823-1825, 2010.

[97] R. Noé, W. B. Sessa, R. Welter et al. , " New FSK phase-diversity receiver in a 150 Mbit/s coherent optical transmission system," *Electronics Letters* , vol. 24, no. 9, pp. 567-568, 1988.

[98] A. Al-Bermani, C. Wördehoff, S. Hoffmann et al., "Synchronous 16-QAM Transmission in a FPGA-Based Coherent Receiver with Different Phase Estimation Filter Lengths," in *Proc. 12. ITG-Fachtagung "Photonische Netze"*, 2011.

[99] A. Al-Bermani, C. Wördehoff, K. Puntsri et al., "Phase Estimation Filter Length Tolerance for Real-Time 16-QAM Transmission System Using QPSK Partitioning," in *Proc. Workshop der ITG-Fachgruppe 5.3.1*, 2012.

[100] A. Al-Bermani, C. Wördehoff, O. Jan et al., "The Influence of Laser Phase noise on Carrier Phase Estimation of a Real-Time 16-QAM Transmission with FPGA Based Coherent Receiver," in *Proc. 14. ITG-Fachtagung "Photonische Netze"*, 2013.

[101] K. Kikuchi, "Effect of 1/f-type FM noise on semiconductor-laser linewidth residual in high power limit," *IEEE J. Quantum Electron*, vol. 25, no. 4, pp. 684-688, 1989.

[102] Z. Tao, L. Li, A. Isomura et al., "Multiplier-free Phase Recovery for Optical Coherent Receivers," in *Proc. Optical Fiber communication/National Fiber Optic Engineers Conference (OFC/NFOEC)* , 2008.

[103] A. Al-Bermani, C. Wördehoff, K. Puntsri et al., "Real-time Synchronous 16-QAM Optical Transmission System Using Blind Phase Search and QPSK Partitioning Carrier Recovery Techniques," in *Proc. 13. ITG-Fachtagung "Photonische Netze"*, 2012.

[104] Ho, K.P., Cuei, H.W, "Generation of arbitrary quadrature signals using one dual-drive modulator," *IEEE Journal of Lightwave Technology* , vol. 23, no. 2, p. 764–770, 2005.

[105] F. J. Casadevall and A. Valdovinos, "Performance analysis of QAM modulations applied to the LINC transmitter," *IEEE Trans. Veh. Technol.,* vol. 42, no. 4, p. 399–406, 1993.

[106] D. C. Cox and R. P. Leck, "Component signal separation and recombination for linear amplification with nonlinear components," *IEEE Trans. Commun.,* vol. 23, no. 11, p. 1281–1287, 1975.

[107] G.-W. Lu, T. Sakamoto, A. Chiba, T. Kawanishi, T. Miyazaki, K. Higuma, M. Sudo, and J. Ichikawa, "Monolithically Integrated Quad Mach-Zehnder IQ Modulator for Optical 16-QAM Generation," in *Conference on Lasers and Electro-Optics, OSA Technical Digest (CD), paper CPDA7*, 2010.

[108] L. Zhang, X. Hu, Y. Wu, Q. Liu, T. Wang, and Y. Su, "Multiple 16QAM signals generation at 40Gbit/s using a novel transmitter," in *Proc. 15th Asia-Pacific Conference on Communications (APCC)*, 2009.

[109] G.-W. Lu, M. Sköld, P. Johannisson, J. Zhao, M. Sjödin, H. Sunnerud, M. Westlund, A. Ellis, and P. Andrekson, "40-Gbaud 16-QAM transmitter using tandem IQ modulators with binary driving electronic signals," *Optics Express,* vol. 18, no. 22, pp. 23062-23069, 2010.

[110] M. Seimetz, "Transmitter design," in *High-order modulation for optical fiber transmission*, Springer, 2009, p. 28.

[111] X. Zhou, and J. Yu, "200-Gb/s PDM-16QAM generation using a new synthesizing method," in *Proc. ECOC 2009, paper 10.3.5*, 2009.

[112] H. Y. Choi, T. Tsuritani, and I. Morita, "Optical transmitter for 320-Gb/s PDM-RZ-16QAM generation using electrical binary drive signals," *Optics Express,* vol. 20, no. 27, pp. 28772-28778, 2012.

[113] M. Secondini, E. Forestieri, and F. Cavaliere, "Novel optical modulation scheme for 16-QAM format with quadrant differential encoding," in *Proc. Photonics in Switching*, 2009.

[114] S. Yan, D. Wang, Y. Gao, C. Lu, A. Lau, Y. Ji, L. Liu, and X. Xu , "Generation of square or hexagonal 16-QAM signals using a single dual drive IQ modulator driven by binary signals," in *Proc. OFC/FOEC, paper OW3H.3*, 2012.

[115] A. Malacarne, F. Fresi, J. Klamkin, and L. Poti, "Versatile offset-free 16-QAM single dual-drive IQ modulator driven by binary signals," *Optics Letters,* vol. 37, no. 19, pp. 4149-4151, 2012.

[116] T. Sakamoto, A. Chiba, and T. Kawanishi, "50-Gb/s 16 QAM by a quad-parallel Mach-Zehnder modulator," in *Proc. European Conference on Optical Communication (ECOC), PDP2.8*, 2007.

[117] L. Lei, Y. Yu, F. Lou, Z. Zhang, L. Xiang, and X. Zhang, "A simple experimental scheme for M-QAM optical signals generation," *Frontiers of Optoelectronics,* vol. 5, no. 2, pp. 200-207, 2012.

List of figures and tables